Novel Optoelectronic and Plasmonic Bulk Heterojunction Neurointerfaces for Controlled Capacitive Charge Transfer

by

Rustamzhon Melikov

A Dissertation Submitted to the

Graduate School of Sciences and Engineering

in Partial Fulfillment of the Requirements for

the Degree of

Doctor of Philosophy

in

Electrical and Electronics Engineering

Koc University

January 2021

Novel Optoelectronic and Plasmonic Bulk Heterojunction Neurointerfaces for Controlled Capacitive Charge Transfer

Koc University

Graduate School of Sciences and Engineering

This is to certify that I have examined this copy of a doctoral dissertation by

Rustamzhon Melikov

and have found that it is complete and satisfactory in all respects,
and that any and all revisions required by the final
examining committee have been made.

Committee Members:

_____

Assoc. Prof. Dr. Sedat Nizamoğlu

_____

Assist. Prof. Dr. Aşkın Kocabaş

_____

Prof. Dr. Alper Kiraz

_____

Assist. Prof Burak Ulgut

_____

Prof. Dr. Burcin Unlu

Date: 25 January 2021

To Salim Khafizov …

ABSTRACT

Artificial control of neural activity allows for understanding complex neural networks and improving therapy of neurological disorders. Light is a non-invasive communication trigger with biological systems. Proper transduction of light to bioelectrical stimuli via artificial photoactive devices requires simultaneous satisfaction of safety, efficiency, and current direction control. For safety, we demonstrated novel photovoltaic neurointerfaces that incorporate biocompatible materials and induce capacitive charge-transfer based on charging and discharging of double layer at the electrode-electrolyte interface without irreversible Faradaic reactions. For that, we developed a single-junction, wireless and capacitive-charge-injecting biointerface by using a high open-circuit voltage (0.75 V) bulk heterojunction of PTB7-Th:PC71BM. For efficiency, we integrated plasmonic interactions to optoelectronic biointerfaces. So far, plasmonics has been primarily used for heat-induced cell stimulation due to membrane capacitance change (i.e., optocapacitance). For the first time, we demonstrated that plasmonic coupling to photocapacitor biointerfaces improves safe and efficacious neuromodulating displacement charges for an average of 185% in the entire visible spectrum while maintaining the Faradaic currents below 1%. For current direction control, we show that utilization of photovoltaic biointerfaces combined with light waveform shaping can generate safe capacitive currents for bidirectional modulation of neurons. The differential photovoltage response of the double-layer capacitor facilitates the direction control of capacitive currents depending on the slope of light intensity. Hence, the findings of this thesis show the great promise of optoelectronic neurointerfaces for non-genetic, all-optical and safe modulation of neurons.

ÖZET

Yapay sinir aktivitesi kontrolü, karmaşık sinir ağlarını anlamaya ve nörolojik bozuklukların tedavisini iyileştirmeye izin verir. Işık, biyolojik sistemlerle invazif olmayan bir iletişim tetikleyicisidir. Yapay fotoaktif cihazlar aracılığıyla ışığın biyoelektrik uyaranlara doğru şekilde iletilmesi, aynı anda güvenlik, verimlilik ve mevcut yön kontrolü tatminini gerektirir. Güvenlik için, biyouyumlu malzemeleri içeren ve elektrot-elektrolit arayüzünde çift katmanın geri dönüşü olmayan Faradaik reaksiyonlar olmadan şarj edilmesi ve boşaltılmasına dayanan kapasitif yük aktarımını indükleyen yeni fotovoltaik nöro arayüzleri gösterdik. Bunun için, PTB7-Th: PC71BM'nin yüksek açık devre voltajlı (0,75 V) toplu heterojonksiyonunu kullanarak tek bağlantılı, kablosuz ve kapasitif şarj enjekte eden bir biyo arayüz geliştirdik. Verimlilik için, plazmonik etkileşimleri optoelektronik biyo arayüzlere entegre ettik. Şimdiye kadar, plazmonikler esas olarak membran kapasitans değişikliği (yani optokapasitans) nedeniyle ısı kaynaklı hücre stimülasyonu için kullanılmıştır. İlk kez, fotokapasitör biyo-arayüzlere plasmonik bağlanmanın, Faradaik akımları % 1'in altında tutarken tamamen görünür spektrumda ortalama % 185 güvenli ve etkili nöromodülasyon yer değiştirme yüklerini iyileştirdiğini gösterdik. Akım yönü kontrolü için, ışık dalga formu şekillendirme ile birlikte fotovoltaik biyo arayüzlerin kullanımının nöronların çift yönlü modülasyonu için güvenli kapasitif akımlar oluşturabileceğini gösteriyoruz. Çift katmanlı kapasitörün diferansiyel foto gerilim yanıtı, ışık yoğunluğunun eğimine bağlı olarak kapasitif akımların yön kontrolünü kolaylaştırır. Bu nedenle, bu tezin bulguları, nöronların genetik olmayan, tamamen optik ve güvenli modülasyonu için optoelektronik nöro-arayüzlerin büyük umut vaadini göstermektedir.

ACKNOWLEDGEMENTS

First of all, I am grateful to my supervisor Prof. Dr. Sedat Nizamoglu during my Masters and PhD for his guidance and contribution to the development of myself. It was great experience. In the first 2 years of total 6 years of graduate life, it was amazing experience observing the development of lab and seeing admission of new lab members to IDEALAB. I greatly owe this valuable experience to my supervisor.

My PhD life was precious experience for me, during my emotional ups and downs I received great support from my supervisor, professors, lab mates and friends, as most PhDs students go through. I had opportunity to meet new scientists around the world.

I owe special thanks to Dr. Daniel Aaron Press, Dr. Ganesh Kumar Baskaran, Dr. Shashi Bhushan Srivastava and Dr. Sadra Sadeghi for their contribution and collaboration in my studies. I enjoyed working with you a lot. Again, I want to thank you.

I want to thank my family and relatives for their support. As coming from a culture where doing PhD is rare, they supported me fully with understanding. In Tajikistan (some, not all, post-soviet countries) the way of doing PhD is different. I remember dozens of time explaining them how it is conducted here. It was fun and hope more students pursue career of Research and Development. I want to thank again my father Abduhakim Melikov, my uncle Abdurahmon Melikov and my grandfather Salim Khafizov for encouraging me to pursue in science by engaging with me, with riddles and discussions on physics and engineering. I want to thank my mentor in high school in physics Olympiad group Prof. Normurodov for his effort to teaching me the problem-solving skills in physics.

I want to thank specially my internal jury members Assoc. Prof. Dr. Aşkın Kocabaş and Prof. Dr. Alper Kiraz for their valuable insights and their time. I want to thank external jury members Assist. Prof. Dr. Burak Ulgut and Prof. Dr. Burcin Unlu for agreeing to be jury members in this unrest times. I am very thankful. Thank you very much.

I want to thank my lab mates former, current, and future, Ersan Ozelci, Houman Bahmani Jalali, Sadra Sadeghi, Itir Bakis Dogru Yuksel, Mohammad Mohamadi Aria, Anil Fettahoglu, Reza Rahighi, Onuralp Karatum, Guncem Ozgun Eren, Mertcan Han, Asim Onal, Fatma Oz, Mehwish Shabbir for their great support. It was fun hanging out with you.

I want to thank TUBITAK and this project has received funding from the European Research Council (ERC) under the European Union Horizon 2020 Research and Innovation Programme (Grant agreement no. 639846). I want to thank ERC.

I want to thank my friends in and out of Turkey.

CONTENTS

LIST OF FIGURES

LIST OF TABLES

ABBREVIATIONS

AC	Alternating current
aCSF	Artificial cerebrospinal fluid
AFM	Atomic force microscopy
AuNI	Gold nanoislands
CV	Cyclic voltametry
DAPI	4′,6-diamidino-2-phenylindole
DMEM	Dulbecco's Modified Eagle's Medium
DMSO	Dimethyl sulfoxide
EIS	Electrochemical impedance spectroscopy
EPC	Electrophysiology patch clamp
F8BT	Poly(9,9-dioctylfluorene-alt-benzothiadiazole)
FRA	Frequency response analysis
GNR	Gold nanorods
H2Pc	Phthalocyanine
HH	Hodgkin-Huxley
HOMO	Highest Occupied Molecular Orbital
IR	Infrared
IS	Inpedance spectroscopy
ITO	Indium Tin Oxide

IV	Current-Voltage
LED	Light emitting diode
LSPR	Localized surface plasmon resonance
LUMO	Lowest Occupied Molecular Orbital
MDMO-PPV	Poly(2-methoxy-5-(3′,7′-dimethyloctyloxy)-1,4-phenylenevinylene)
MEA	Micro electrode arrays
MEH-PPV	Poly[2-methoxy-5-(2'-ethylhexyloxy)-1,4-phenylene vinylene]
MPF	maximum permissible radiant power
MTT	(3-(4,5-Dimethylthiazol-2-yl)-2,5-Diphenyltetrazolium Bromide)
N2200	Poly{[N,N′-bis(2-octyldodecyl)-naphthalene-1,4,5,8-bis(dicarboximide)-2,6-diyl]-alt-5,5′-(2,2′-bithiophene)}
N2A	Neuro-2a
NIR	Near infrared
NP	Nanoparticle
P3HT	Poly(3-hexylthiophene-2,5-diyl)
P3OT	Poly(3-octylthiophene-2,5-diyl)
PbS	Lead Sulfide
PC61BM	Phenyl-C61-butyric acid methyl ester
PC71BM	Phenyl-C71-butyric acid methyl ester
PCBM	Phenyl-C61-butyric acid methyl ester
PCPDTBT	Poly[2,6-(4,4-bis-(2-ethylhexyl)-4H-cyclopenta [2,1-b;3,4-b′]dithiophene)-alt-4,7(2,1,3-benzothiadiazole)]

PDPP3T	Poly{2,2′-[(2,5-bis(2-hexyldecyl)-3,6-dioxo-2,3,5,6-tetrahydropyrrolo[3,4-c]pyrrole-1,4-diyl)dithiophene]- 5,5′-diyl-alt-thiophen-2,5-diyl}
PEDOT:PSS	poly(3,4-ethylenedioxythiophene) polystyrene sulfonate
PFA	Paraformaldehyde
PLL	Poly-l-lysine
PTB7-Th	Poly[4,8-bis(5-(2-ethylhexyl)thiophen-2-yl)benzo[1,2-b;4,5-b']dithiophene-2,6-diyl-alt-(4-(2-ethylhexyl)-3-fluorothieno[3,4-b]thiophene-)-2-carboxylate-2-6-diyl)]
PTCDI	N,N′-Dioctyl-3,4,9,10-perylenedicarboximide
QD	Quantum dot
rpm	revolution per minute
SEM	Scanning electron microscopy
SQIB	Aquarine
TBAPF6	Tetrabutylammonium hexafluorophosphate
UV	Ultraviolet

Chapter 1: Introduction

Light activation of neurons by planar interfaces is a developing field with applications extending from fundamental examination of neuronal systems to the development of advanced implants such as artificial retina [1, 2]. Advantageously, light can be effectively focused to a spot that enables precise and local perturbation of discrete-parts of a single neuron [3, 4]. Moreover, light can be adjusted to remotely control the strength of the transmembrane potential and it also allows for separation of cell stimulation and recording channels [5]. Hence, the light stimulation allows spatially and temporally precise excitation and inhibition of neurons both *in vitro* and *in vivo*, and it can be used for biomedical applications such as drug screening, basic neurological treatments, and light-activated implants [6-8]. Optogenetics, which express light-activated proteins in the ion channels of the membrane by viral mutation, offers a solution for the light-activation of the cells.[9] For example, channelrhodopsin, halorhodopsin, and archaerhodopsin are used for neural activation and archaerhodopsin-3, eNpHR, KR2 are used for suppression of neural activity [8, 10]. However, since these ion channels or pumps are generally introduced via genetic modification by a viral vector delivery [5], such a structural variation is currently one of the main concerns. In addition, determination of the suitable viral vectors, heterogeneity in the expression, and immune reaction due to heterologous protein expression currently limit its use in the clinics.[11]

Extracellular electrical stimulation of nerve cells is a non-genetic and clinically-approved method to control the neural activity [12]. To mitigate the toxicity from electrochemical reactions at metal-tissue interfaces, charge balanced alternating current pulses (AC) were used for implantable neuroprostheses including cochlear implants, deep brain stimulators, spinal cord stimulators, and retinal implants [13-16]. Short-duration pulses are applied to neural tissue in a phase-locked fashion for stimulation [17]. To inhibit the target neurons, implants typically work indirectly by delivering excitation to populations of neurons by

delivering high pulse rates that suffer from some undesirable side effects such as persistent refractory state [18].

Alternatively, for neural photostimulation photovoltaic substrates attracted significant attention and the control of the stimulating charge-transfer mechanisms by these substrates is critical for safe and effective cell stimulation. Advantageously, they convert light to bioelectrical stimuli without any need for external power supply and complicated electronics. The flexibility and mechanical matching of photovoltaic substrates with the biological environment make them as an ideal candidate for implantation.[19].

Today neural implants in the clinics use two major stimulation mechanisms, which are based on Faradaic and capacitive (non-Faradaic) charge-transfer processes [20-26]. In Faradaic process, electrons are transferred between the electrode and electrolyte with oxidation and reduction reactions. In capacitive process charges electrostatically perturbs the ions in the electrode-electrolyte interface and leads stimulating currents [12, 27]. Like in clinical electrodes, it is also desired to control the charge-transfer mechanisms by photovoltaic substrates. So far, optically-active substrates using different conjugated polymer material systems such as P3HT, P3HT:PCBM, P3OT:N2200, PDPP3T:PCBM, and P3HT:N2200 were demonstrated for photostimulation [28-33]. In the previous reports the control on Faradaic vs. capacitive contribution was generally realized by varying the polymeric materials interfacing with cells. Moreover, in some cases the charge density levels are not high enough to resolve the Faradaic and capacitive contribution [34]. To resolve the contribution by each mechanism, light intensity levels can be increased, but this can lead to thermocapacitive effects on the membrane [35, 36], which needs to be minimized to clearly observe the charge-transfer mechanisms.

Another important parameter to be considered as an merits affecting the optoelectronic properties for photovoltaic substrates used for extracellular photostimulation is thier open-circuit voltage. For photostimulation of cells, photodiodes connected in series and tandem architecture were utilized to change the open-circuit voltage.[28, 37] Alternatively, bulk heterojunctions can overcome the limitation of charge carrier

diffusion in organic semiconductors and enables significant enhancement in the generation of photo-induced charges that can be effectively used for stimulation of neurons.[38] Moreover, it can also allow for control of optoelectronic and bioelectronic properties of biointerfaces by varying the photoactive layer. So far, P3HT:PCBM, P3OT:N2200, PDPP3T:PCBM, and P3HT:N2200 bulk heterojunctions were independently examined for photostimulation of cells.[28, 30, 32, 33, 39, 40].

Next, capacitive currents have positive and negative transient peaks hence it has wide variety of applications for modulation. Pulse modulation is a widely used technique in bioelectronics for neuromodulation [21, 41, 42]. In general, electrical power gradients were utilized. Schoen et. al. demonstrated modulation of membrane potential under rising and falling voltage pulse modulations to excite neural cells attached to capacitive substrate [21]. In terms of optical modulation, square-waves have been generally applied for photostimulation [43-46]. However, the effect of variation of light power gradients on photocapacitive substrates were not investigated for photostimulation yet.

Finally, optical devices make use of plasmonics for its superior optical properteis. Plasmonics has high potential to increase the performance of optoelectronic biointerfaces. In principle, plasmonic nanostructures can concentrate the incoming radiation to a subwavelength spatial profile due to localized surface plasmon resonance (LSPR) [47], and may boost the light-matter interactions for sensitive transduction of optical signal to bioelectrical stimuli. In addition, light-induced plasmon energy can be transferred to the conduction band of the nanostructure that can produce energetic electrons, known as hot electrons, and these charges may be controlled for photostimulation of neurons. However, despite its high potential for extracellular stimulation, plasmonics has been mainly used for photothermal transmembrane modulation of neurons [48-52]. Light is converted to heat energy due to decay of plasmon oscillations, and the resultant temperature variation induces a membrane potential change through a transient membrane capacitance shift [48]. Recently, some evidence showing that metal decoration can support increase on capacitive and Faradaic currents were also reported [45].

Chapter 2: Literature review

The study and manipulation of bioelectricity dates to discovery of electricity by human civilization. For example, in ancient Egypt and Greece electrical discharges from catfish and eels were used as a treatment for improvement of blood circulation and for pain relief. Luigi Galvani around 1780 conducted experiments on frog legs for proving that electrical discharges induce muscle contraction, which was collected in assay named 'Commentary on the Effect of Electricity on Muscular Motion'. The phenomena were described by the term 'animal electricity'. Next, German scientists Herman von Holmholtz and Emil Heinrich Du Bois-Raymond recorded action potentials with galvanometer. Du Bois-Reymond's book called 'Research on Animal Electricity' in 1848 is considered as beginning of scientific electrophysiology. Finally, with Alan Hodgkin and Andrew Huxley earliest and most famous models in computational biochemistry were introduced for theory on the propagation of action potentials in 1952.

Next big advancement is the invention of patch-clamp techniques by Erwin Neher and Bert Sakmann in 1970s. This way recording of electrical activity can be measured extracellularly by placing the electrode near the cell or intracellularly by reaching the intracellular medium and record the potential inside the cell. The advantage of intracellular recording is it shows actual potential of the cell, which allows better understanding on electrical parameters of the cell. In patch clamp experiments 1 - 2 µm glass pipettes are used. Since, then patch clamp became a golden standard in electrophysiology allowing better understanding of electrical behavior of the cells. In extracellular recording, single electrode is sufficient. The advantage of extracellular recording is for its spatial resolution which recording many cells. Micro Electrode Arrays (MEA) is great for in vitro experiments more than 10000 electrodes, which polytrodes are used for in vivo experiments. The disadvantage of extracellular electrodes comes from high impedances at small scales, which increases signal to noise ratio. In any case, extracellular recording does not measure actual membrane potential, hence it measures

superimposed spatiotemporal-dependent potential, which makes it difficult for acquiring relevant information from extracellular recoding.

2.1 The Ionic basis of membrane potential

In 1952, Hodgkin and Huxley developed an electrical model for the neural membranes (figure 2.1). The model depicts different part of the membrane as an electrical element. The lipid bilayer of the cell membrane is considered as a capacitor. Voltage gated K^+ and Na^+ channels are considered as nonlinear electrical conductance. Leakage channels are considered as linear electrical conductance. The flow of ions for each channel is assumed to be batteries driven by a potential E.

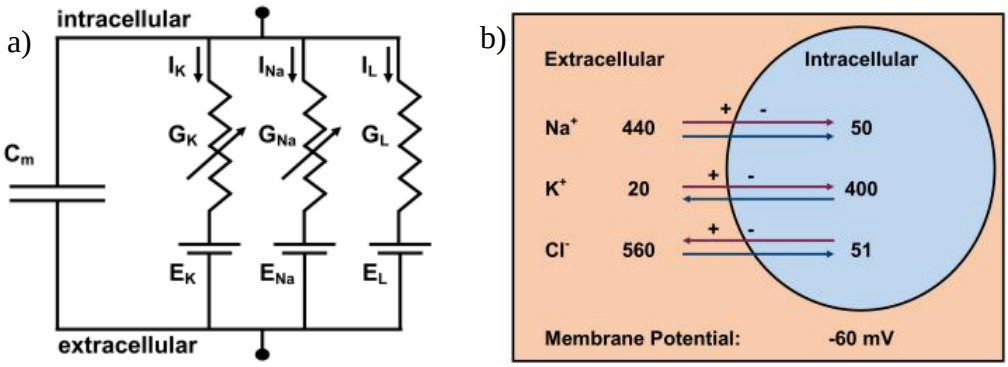

Figure 2.1 (a) Circuit diagram of Hodgkin-Huxley model for the membrane of a giant squid axon. The lipid bilayer is represented as Cm. Voltage-gated ion channels behave as nonlinear conductances (G_K, G_{Na}), leak ion channels is considered as linear (G_L) conductance, respectively.E represents electrochemical gradient. (b) Ion distribution in and out of the cell. The K+, Na+ and Cl− ions are permeable through cell membrane. The blue arrows represent the ion flux, the red arrows represent current along the electrical gradient. When net flux is zero, the cell membrane is at resting potential.

In figure 2.1 b, Cl^- and Na^+ diffusing into the cell membrane, while K^+ diffusing out of the cell membrane. When the net flux across the membrane potential is zero, the cell reaches it resting potential. With the given concentrations in figure 2.1 b, resting potential can be calculated by Goldman-Hodgkin-Katz equation (-60 mV) (equation 2.1). The Na/K ATPase transports K^+ and Na^+ ions in order to maintain balance between intracellular and extracellular medium.

$$V_{rest} = \frac{RT}{F} \ln \left(\frac{E_K[K]_o + E_{Na}[Na]_o + E_{Cl}[Cl]_i}{E_K[K]_i + E_{Na}[Na]_i + E_{Cl}[Cl]_o}\right) \quad (2.1)$$

2.1.1 Action potential

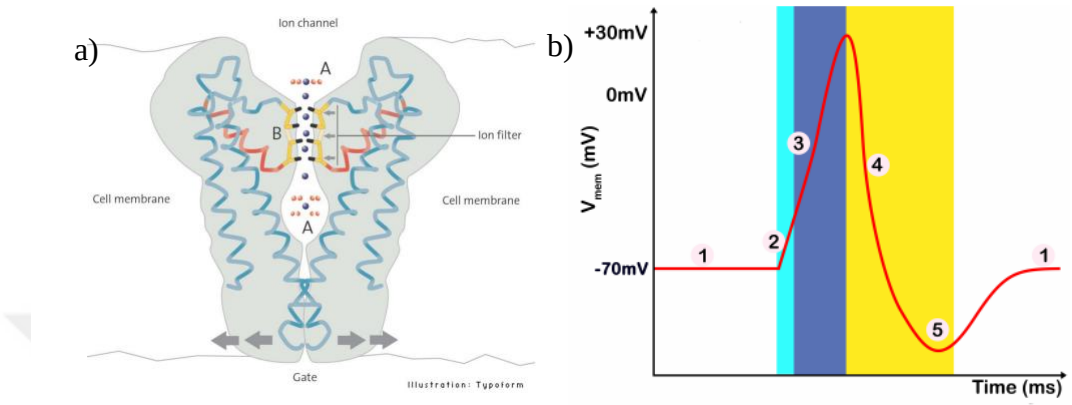

Figure 2.2 (a)Schematic representation of an ion channel in the cell membrane. To pass through the channel, ion (A) needs to lose its water to bind to specific residues of the filter (B). (b) Action potential for squid giant axon. (1) Membrane at resting state, (2) voltage threshold region, (3) depolarization phase, (4), repolarization phase. (5) hyperpolarization phase

Excitable cells communicate between each other by electrical impulses, that are called as action potentials. The shape and size of action potentials vary by the cell types and ion concentration in and outside the cell. In figure 2.2 action potential is depicted for squid giant axon. Initially at phase 1 the cell is at resting state, where there is no efflux or influx of ions. When the trigger is applied, until membrane potential reaches the threshold it stays at phase 2, where influx of Na^+ ions into the cell occurs. In phase 3, the voltage gated Na^+ ions open and more Na^+ ions migrate inside the cell, this increase membrane potential inside the cell with respect to outside of the cell. In phase 4, the voltage gated K^+ ions open while the voltage gated Na^+ ions close, then K^+ ions diffuse outside the cell, this decrease the membrane potential. In phase 5, Na^+ and K^+ ions balance maintained until the cell membrane reaches resting potential.

2.1.2 Patch Clamp technique

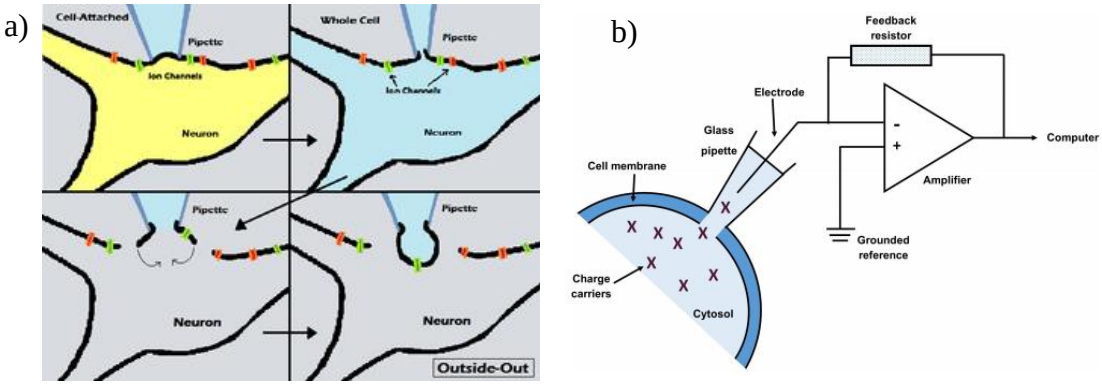

Figure 2.3 (a) Cell attached, whole-cell inside-out and outside-in patch configurations. (b) Electrical schematic of a patch clamp setup.

The patch-clamp recording is a gold standard for investigating ion channel conductance down to single channel recording. Patch clamp can be applied for both cell cultures and sliced tissues. There are four patch clamp configurations such as Cell attached, whole-cell inside-out and outside-in patch configurations (figure 2.3 a). Firstly, the cell attached configuration is obtained to isolate the cell and obtain high resistance seal. The consecutive pulse section breaks the membrane at the tip of the glass pipette thus connecting electrode solution to the intracellular solution. This configuration is called whole-cell patch configuration. Due to direct access to intracellular medium, it is commonly used configuration. For single channel measurements inside-out or outside-in patch clamp configurations can be utilized. In figure 2.3 b, electrical schematic of patch clamp configuration is shown. The signal that is read by electrode is amplified with feedback resistor amplified. The disadvantage of patch clamp technique lies in single cell recording, where it is not suitable for high-throughput screening. However, complex physical properties of ion channels can be studied in detail.

2.2 Optical techniques

The advantages of electrodes for both measuring and exciting the cells is that it both uses electrical currents and potentials. Electrodes need physical contact, and its fixed by

design, hence it has difficulty to adapt actual morphology of the system. Optical techniques have attracted a lot of interest in past decades for investigating biological systems. Light is advantageous in many aspects such as it propagates though various biological tissues, it does not need physical contact hence the risk of mechanical stress and damage is low. Moreover, light can be both spatially and temporally modulated. The main requirement for using light instead of electrical conductors are that light need transduction mechanism to convert into electrical signals. Currently, there is not an optical technique to both stimulate and record simultaneously. For optical stimulation various transducers were used such as intrinsic absorbers, molecular probes, nano/micro particles, and solid-state devices. For the recording fluorescent probes are used widely.

2.2.1 Direct optical stimulation

Apart from light sensitive biological systems (retina), light does not specifically interact with neurons. Generally photosensitive transducers are used in the vicinity of the cell. Many of systems that excite or inhibit optically use photosensitive dyes, in some cases endogenous fluorophores are used. In 1971 blue and green laser light stimulated Aplysia neurons. Heme or carotenoid molecules were intrinsically pigmented.

Another method is to use ultra-short optical laser pulses in nanosecond or femtosecond regime. For low intensities, the transduction of optical pulse happens by two photon absorption by endogenous fluorophores. At higher intensities, transient membrane poration or increase in temperature which results increase in capacitance of the membrane potential results spiking activity.

2.2.2 Molecular based stimulation

In 2005 Boyden et al. expressed channelrhodopsin2 in mammalian neurons, which is a light sensitive ion channel. It controls neural activity in milliseconds precision. This was an optogenetic revolution in neuroscience. The main advantage of optogenetic method is for its high spatiotemporal resolution.

2.2.3 Nano-/micro-particle stimulation

In the few decades, the use of nanoparticles (NP) has been developed intensively. The advantages of nanoparticles are as follows: (1) it can be used as a transport for functional molecules; (2) high surface to volume ratio; (3) tunability in shape and dimension; (4) unique optical properties. The use of NPs as a transducer for direct modulation of cell membrane is new and hot topic. In 2001, Winter et al. proposed attaching semiconductor quantum dots to the plasma membrane and exploit electrical dipole property of NPs for photoactivation. However, there was no reliable photostimulation. The more successful approach was the use of thin film from NPs. Another approach is using Thermal properties of NPs at IR window to successfully modulate neural membrane potential. Infrared thermal stimulation achieved both excitation and inhibition of neural activity based on developed stimulation protocol.

2.2.4 Device based stimulation

Solid-state silicon-based devices are well investigated by Fromherz and coworkers around 1990s. In 2001, Colicos et al proposed coupling of optical excitation and electronic device for better spatial resolution with respect to electrode-based stimulation. They used variation of conductivity of silicon under light illumination. Next, Palankar et al proposed the use of photovoltaic effect of silicon for wireless retinal stimulation. Here is light used to power the device wirelessly.

2.3 Organic semiconductors for neural stimulation

The optical devices for neural stimulation which is described in section 2.2 is based on inorganic semiconductors and metals. Stiffness and electronic conduction properties of inorganic crystalline materials are main disadvantage for interfacing with biological medium. Organic semiconductors have conjugated carbon atoms with sp3 hybridization, which has semiconducting properties due to easily delocalization of pi electrons in this

conjugated system. Recently organic semiconductors is extensively being utilized for its tunability of optoelectronic properties, ease of manufacturing and processing, soft mechanical properties for flexible and conformable devices in research areas such as organic photovoltaic cells (OPVCs), organic light emitting diodes (OLEDs) and organic thin film transistors (OTFTs).

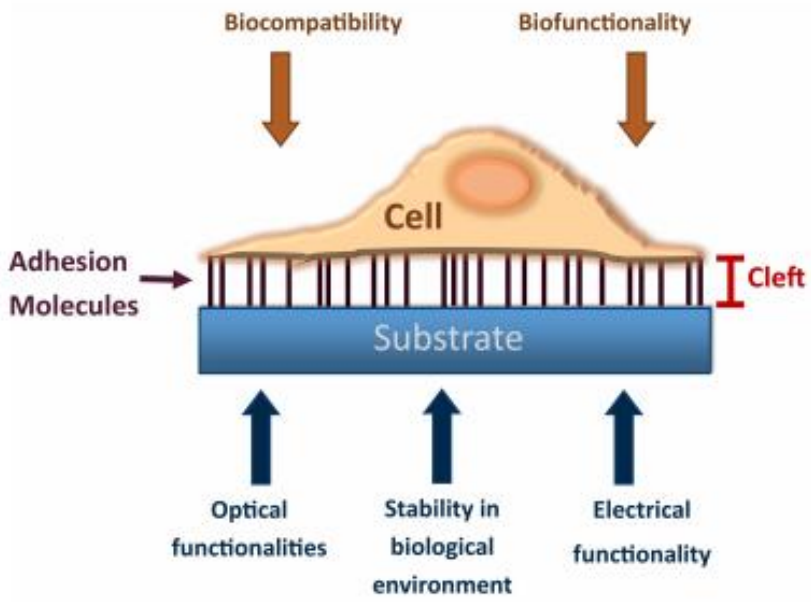

Figure 2.4 Schematic of organic neural interface materials[53]

In bioelectronic applications, organic semiconductors are used as coating material for inorganic electrodes for its better biocompatibility [54]. In last decade, the organic semiconductors are extensively used not only as a passive coating layer but as an active functional material for biological interfaces, such as sensing of biomolecules, functional substrates for cellular growth and activity (figure 2.4).

2.3.1 Photoactive biopolymer interfaces

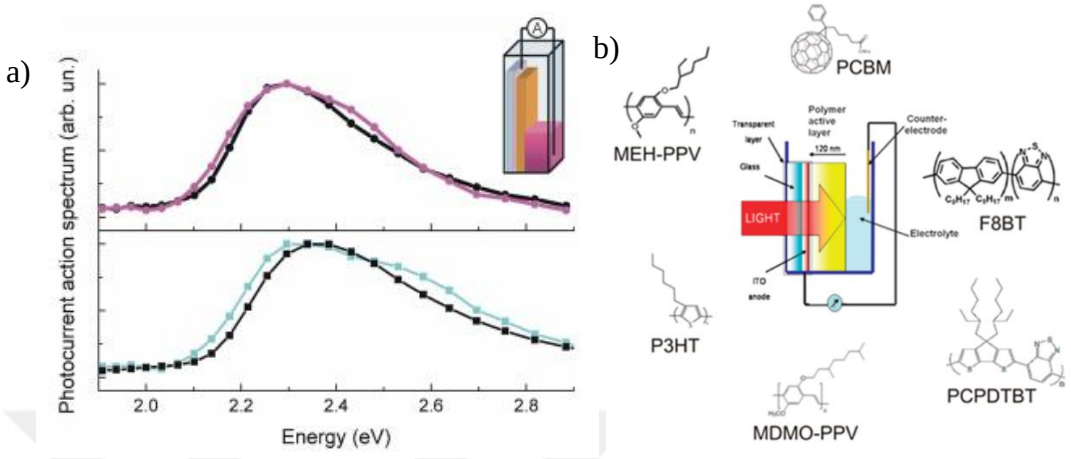

Figure 2.5 (a) Normalized PC(photocurrent) spectra of usual sandwich photodiodes with MEH-PPV, upper panel, circles black line, and MEH-PPV:PCBM, lower panel, squares black line, compared with a liquid cathode, MEM upper, circles magenta line and aCSF lower, squares cyan line. The inset reports a sketch of the hybrid photodiode: [55] (b) Schematic of the photovoltaic/photocatalytic device and chemical structures of the polymers use, as active layers. From top, clockwise: PCBM, F8BT, PCPDTBT, MDMO-PPV, P3HT, MEH-PPV. [56]

For biopolymer interfaces, unique optical properties of organic semiconductors are used as a transducer of light stimuli into bioelectronic signals. Recently, photovoltaic properties of organic materials are well attracted for neural biointerfaces. Due to extracellular medium having high ionic conductivity, the solution can be considered as an electrode, without needing top metal electrode. In 2009 Antognazza et al proposed[55] biointerface comprising of glass substrate, transparent conductive layer of Indium Tin Oxide (ITO) and thin photoactive layer. The photoactive layer consisted of bulk heterojunction of conjugated polymer poly[2-methoxy-5-(2'-ethylhexyloxy)-pphenylene vinylene] (MEH-PPV) as a hole conductor and absorbing material, C61-butyric acid methyl ester (PCBM) as electron acceptor. They demonstrated that the solid/liquid photovoltaic device could generate photocurrent in electrolytic media (figure 2.4). Later Lanzarini et al.[56] used other conjugated polymers such as PCBM, F8BT, PCPDTBT, MDMO-PPV, P3HT, MEH-PPV and showed that under continuous illumination hydrogen is generated in electrolytic media. In this work P3HT was selected as a choice of material for its better photocurrent.

2.3.2 Hybrid biointerfaces for retinal degeneration

In 2011, Ghezzi et al. reported functional organic semiconductor biointerface comprising of ITO/P3HT:PCBM and demonstrated photostimulation on primary cells. It was reported that the biointerface were biocompatible and did not alter physiological properties (figure 2.6). The authors coat thin PLL for biocompatibility and attachment. Action potential from hippocampal cells with a failure rate below 15% was observed, moreover they show that light pulse should be directed to cell body to get reliable action potential spikes.

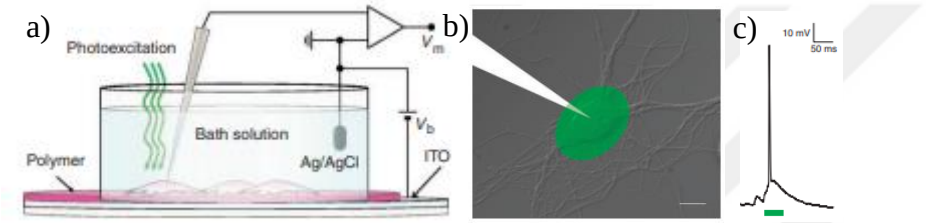

Figure 2.6(a) Schematic representation of biointerface under patch-clamp setup. (b) image of hippocampal cell. (c) Action potential under 50 ms pulsed light [57]

Most of the beforementioned articles use biopolymer interfaces that undergo faradaic reaction to generate photocurrent. In 2019, Glowacki et al. [43] proposed organic electrolytic photocapacitor comprising of thin trilayer of metal and p-n semiconducting organic nanocrystals. The mechanism of charge transfer follows the charging up under light illumination and transducing it into localized displacement current. Free standing, no external bias and stability in physiological conditions are the advantage of electrolytic photocapacitors.

For practical applications, in 2018, Ghezzi et al[19] designed foldable photovoltaic wide field epiretinal prosthesis (POLYRETINA) capable of stimulating retinal ganglion cells under free standing mode. The POLYRETINAwas comprised of PDMS as a substrate, PEDOT:PSS as a transparent conducting layer, P3HT:PCBM as a photoactive layer and

Ti top electrode. It had 46.3 viewing angle, 2215 stimulating pixels and at least 2 years of lifetime.

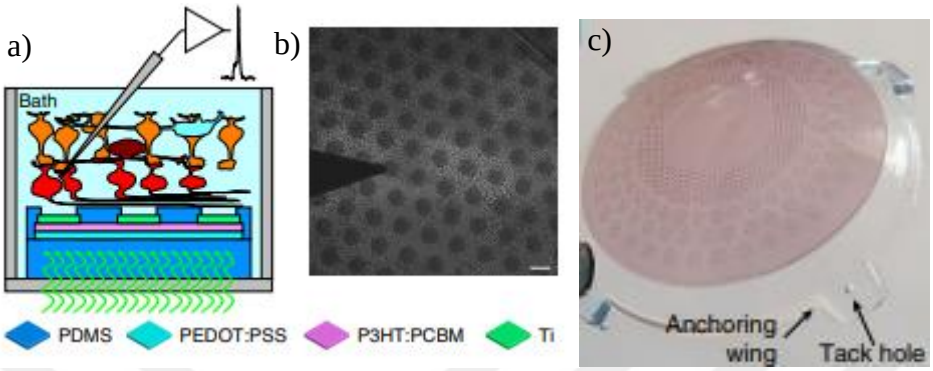

Figure 2.7 (a) Schematic of biointerface and experimental setting. (b) Picture of pixel (c) Image of POLYRETINA [19]

2.4 Charge transfer mechanism in biointerfaces

On Electrode electrolyte interface, two main mechanism of charge transfer happens, faradaic and capacitive charge transfers. With the device architecture and specific band alignment, the amount of current generated from capacitive or faradaic charge transfer can be controlled[43, 45, 55, 58].

In Faradaic charge transfer, surface confined electrochemical reactions occur, such as oxidation and reduction reactions. Since faradaic mechanism inevitably involves direct electron transfer between electrode and electrolyte interface, the ion concentration in electrolyte media changes which may result in harmful side effects in tissues. To solve the issue, capacitive charge transfer mechanism is used. Capacitive charge transfer requires areal capacitance or volumetric capacitance of the electrode. When charge builds up at the surface of the electrode, it attracts opposite charged ions in the electrolyte[59] (figure 2.8).

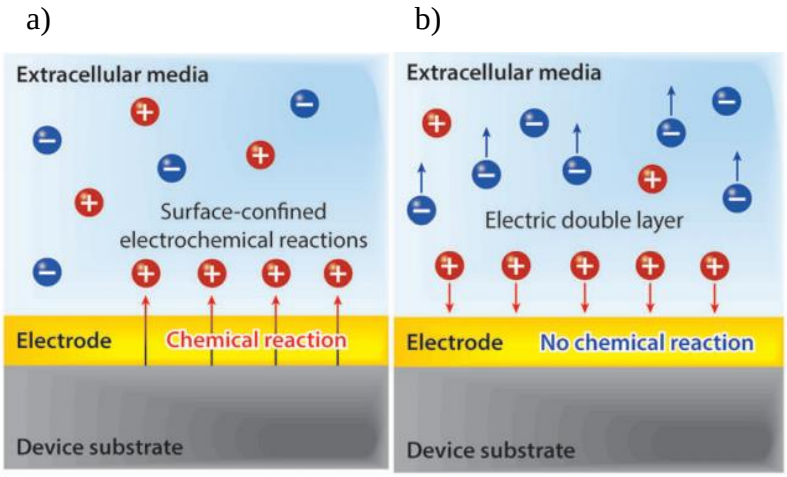

Figure 2.8 (a) Schematic illustration of faradaic charge transfer. (b) Schematic illustration of capacitive charge transfer[59]

2.5 Plasmonic photostimulation of neurons

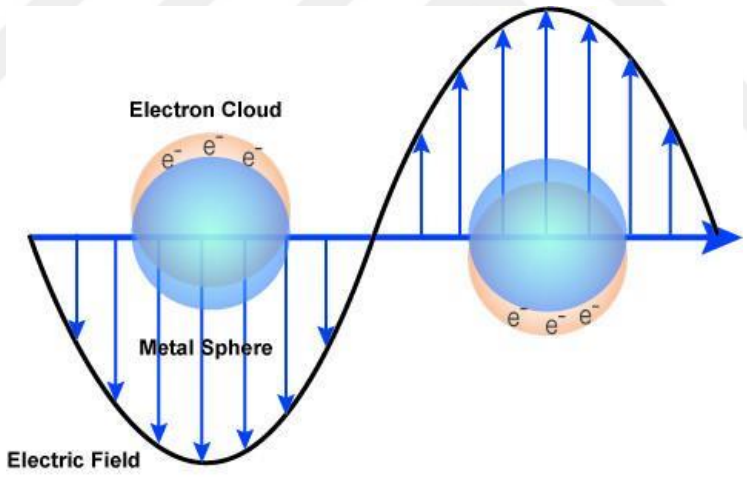

Figure 2.9 Localized surface plasmon resonance

Plasmon is collective oscillation of free electrons with respect to fixed positive ions in the metal. Plasmons have crucial role in the optical properties of metals. Hence, plasmonics hold significant potential due to its strong enhancement capability of light-matter interactions (Figure 2.9). Despite extensive use of metal nanoparticles in nanobiotechnology and biomedicine, its use in extracellular photostimulation has been

mainly focused on photothermal transmembrane modulation of neural cells [49, 51, 52, 60, 61]. Various plasmonic methods have been used for either enhancement of optical properties of the photoactive material or direct perturbation of the neural membrane. One very common method used is heat generation using nano-antenna effect. Photogenerated local heat has been used for directly destroying local tissue [62, 63], to melt membranes for releasing molecules in the local environment, increasing membrane capacitance [60, 64]. However, there is limited research on the enhancement of the optical properties of the photoactive material using plasmonics for the light-based cell stimulation.

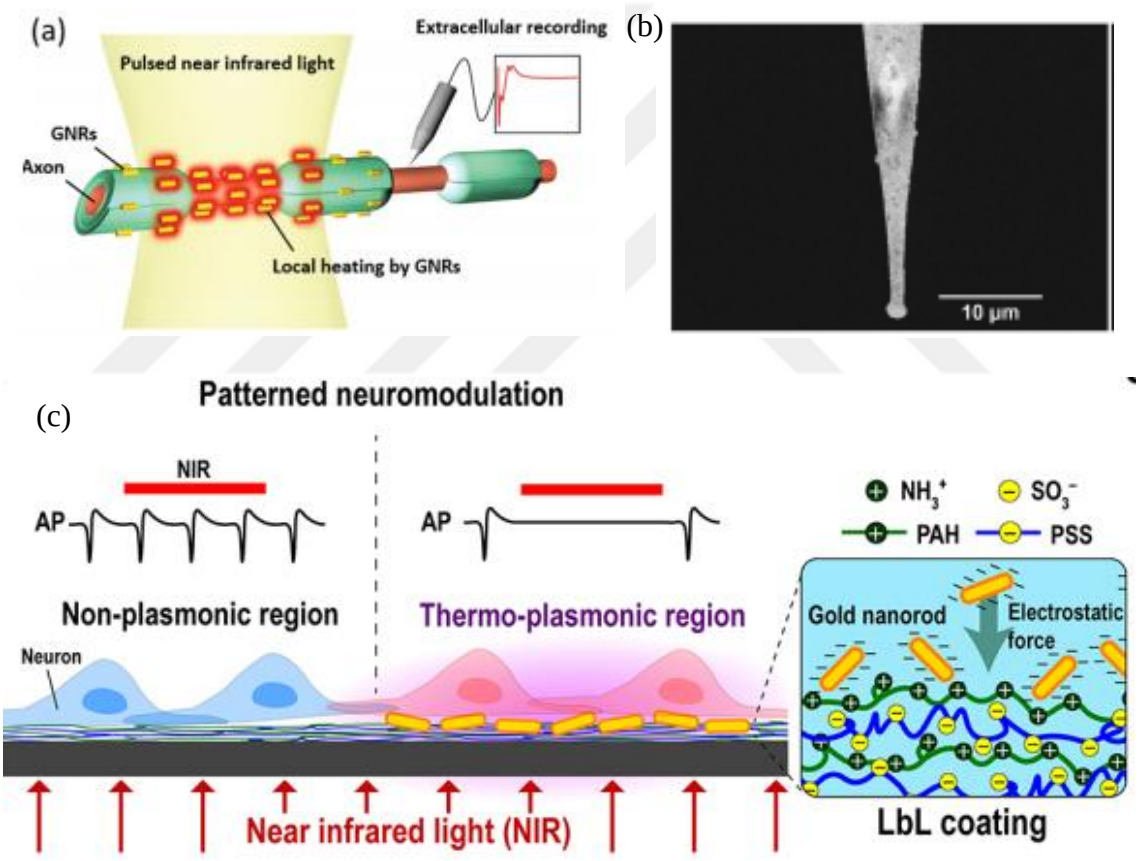

Figure 2.10 (a) Schematic of optical neural stimulation using localized heating of GNRs.[49]. (b) SEM image of micropipette[65] (c) Schematic of inkjet printed thermo plasmonic biointerface[66]

In 2018, Kim et al.[49] demonstrated INS using Gold nanorods (GNR). The results show better neural responsivity, stimulation efficiency and spatial resolution with respect to

conventional INS. They reported more than 6 ^{0}C temperature change within 1 min illumination with energy of 0.0324 J/pulse. Bhethanabotla et al[65], coated gold nanoparticle on nanoelectrodes and show action potential with 120 mW green laser pulse illumination. They show more than 15 ^{0}C temperature increase in the 25 µm proximity from measurement electrode at 100 mW optical power. Similarly, to Kim et al., Nam et. Al inkjet printed GNR and demonstrated growth on hippocampal neurons on the interface. Under NIR illumination they show suppressing of neural activity. Like most plasmonic biointerfaces, they also show temperature increase of up to 9 ^{0}C (Figure 2.10).

Chapter 3: Methods

3.1 Photoelectrode Fabrication

For the fabrication Glovebox, Thermal evaporator, UV-Ozone cleaner, spin coater, weigh, sonicator and heater are used extensively (Figure 3.1).

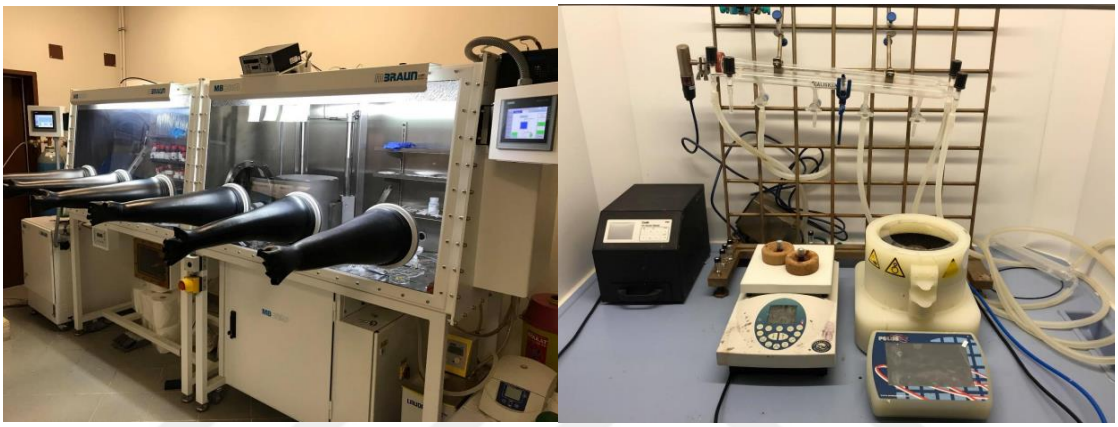

Figure 3.1 Images of equipment used for fabrication of devices. Thermal evaporator, spin coated, heater and UV-Ozone cleaner.

The 95.7 % regioregular P3HT (poly(3-hexylthiophene-2,5-diyl)), >99 % pure PCBM ([6,6]-Phenyl-C61-butyric acid methyl ester), and PbS QDs in toluene photosensitive materials were used as received commercially without any modification. The size of the PbS QDs is 3.7 nm according to the absorbance data (Figure 4.6) [67]. It has oleic acid as a ligand [68, 69]. The photoactive solution was prepared by mixing of two donor (P3HT and PbS QDs) and an acceptor (PCBM) material in o-dichlorobenzene solvent. The blending ratio of the PbS in the P3HT:PbS QDs:PCBM blend is 1:0.17:1. The energy levels of each materials were calculated from cyclic voltammetry measurement discussed in section 4.4 and are close to the literature values [67, 70, 71].

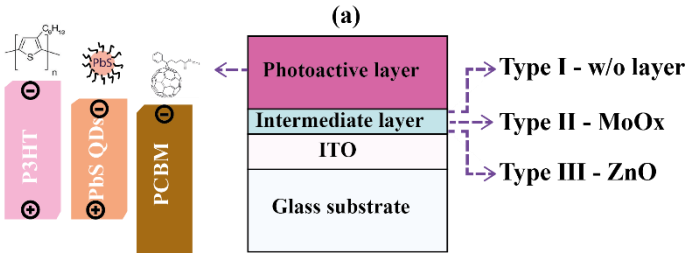

Figure 3.2 Photoelectrode device architectures (Type I, II and III). In all of them P3HT, PbS quantum dots and PCBM blend is used for the photoactive layer.

To study the effect of various functional interfaces, the ITO electrode and photovoltaic layer set aside same for each photoelectrode. We prepared 3-types of photoelectrodes by changing the intermediate layer between ITO and photoactive thin film. The type I (ITO/P3HT:PbS QDs:PCBM) photoelectrode was fabricated by spin coating the photoactive solution on ITO electrode at 2000 rpm and annealing at 155 ^{0}C for 15 minutes. The thickness of the photoactive thin film was found to 83 nm. The type II (ITO/MoOx/P3HT:PbSQDs:PCBM) photoelectrode was fabricated by using 10 nm thick MoOx layer, processed by thermal evaporation at the rate of 0.03 nm/sec under vacuum of 2.0 × 10^{-6} mbar, between ITO and photoactive layer. Similarly, the type III (ITO/ZnO/P3HT:PbSQDs:PCBM) photoelectrode has an additional ZnO layer of 49 nm thickness, processed by sol-gel method, between ITO and photoactive layer.

Figure 3.3 Schematic of the device structures of the biointerface 1 denoted as BI-1 (on the left) and biointerface 2 denoted as BI-2 (on the right).

The two types of biointerfaces were fabricated by changing the photoactive layer with different V_{oc} keeping the ITO/ZnO electrode same. The low-V_{oc} photoactive layer consists the blend of 95.7 % regioregular P3HT (poly(3-hexylthiophene-2,5-diyl)) and > 99 % pure PC61BM ([6,6]-Phenyl-C61-butyric acid methyl ester). The high-V_{oc} photoactive layer was prepared by blending a donor co-polymer poly[4,8-bis(5-(2-

ethylhexyl)thiophen-2-yl)benzo[1,2-b;4,5-b']dithiophene-2,6-diyl-alt-(4-(2-ethylhexyl)-3-fluorothieno[3,4-b]thiophene-)-2-carboxylate-2-6-diyl)] (PTB7-Th) and an acceptor molecule [6,6]-Phenyl-C71-butyric acid methyl ester (PC71BM). The indium tin oxide (ITO) coated glass substrates, P3HT, PTB7-Th, PC61BM, and PC71BM were purchased from Ossila Ltd. The zinc acetate dihydrate, ethanolamine, 2-methxyethanol, chlorobenzene, 1,2-dichlorobenzene, and molybdenum trioxide were purchased from Sigma Aldrich. All the materials and chemicals were used as received.

To fabricate the biointerfaces, the ITO coated glass substrates were sequentially cleaned with 1% by volume Hellmanex soap solution (Ossila Ltd.), de-ionized water, acetone, and isopropanol using ultrasonication. The cleaned substrates were dried in oven at 100 ^{0}C and treated with UV-ozone for 15 min before the coating. The pre-cleaned substrates were spin coated at 2000 rpm for 60 s with ZnO precursor sol-gel solution. The coated substrates were annealed at 250 ^{0}C for 15 min to get the 50 nm of ZnO thin film. The reference photoelectrode (BI-1) was completed by spin coating of P3HT:PC61BM (1:1 weight ratio) solution in o-dichlorobenzene on ITO/ZnO substrate at 1000 rpm for 90 s and annealed at 150 ^{0}C for 15 min. However, the high-V_{oc} photoelectrode (BI-2) was prepared by spin coating of PTB7-Th:PC71BM (1:1.5 weight ratio) solution in chlorobenzene on ITO/ZnO substrate at 600 rpm for 120 s and then dried under nitrogen for 2 h.[72] The thickness of various layers was confirmed by SEM cross-section image (Figure 3.3).

The methods used for fabrication of the device is similar to section 3.1.1 with the following modification. 20 mg ml^{-1} of the donor co-polymer P3HT and 10 mg ml^{-1} of acceptor molecule PC61BM solution was prepared in o-dichlorobenzene and stirred overnight at 70 ^{0}C on a hot plate. Then, 20 mg ml^{-1} P3HT and 10 mg ml^{-1} PC61BM (1:0.5 wt. ratio) was mixed and stirred at 70 ^{0}C for 4 hours. Except the mixing ration of P3HT and PCBM all other methods for fabrication is similar to section 3.1.1.

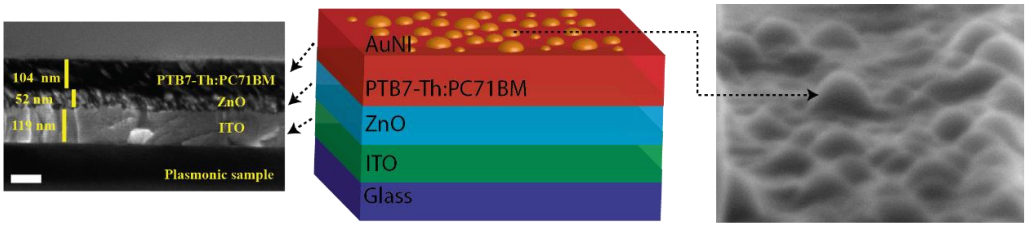

Figure 3.4 (a) (Left) Cross-sectional scanning electron microscopy (SEM) image of the plasmonic biointerface (scale bar, 100 nm). (Middle) Schematic device structure of the plasmonic (ITO/ZnO/PTB7-Th:PC71BM/AuNI) biointerface. (Right) SEM image of nanoislands on the plasmonic biointerface.

Two type of biointerfaces with and without gold nanoislands (AuNI) were fabricated. Indium Tin Oxide (ITO) on glass substrates (side length, 20 mm; side length, 15 mm; thickness 1.1 mm; resistance, 14 - 16 $\Omega.cm^{-2}$; Ossila) was cleaned with 10 wt% Sodium Hydroxide solution for 5 min, 2 % by volume a specific tension-active agent in a water solution (HELLMANEX II, 3 %) for 15 mins at 55 ^{0}C, DI water for 15 min , acetone for 15 mins and isopropyl alcohol for 15 mins using ultrasonic bath. The cleaned ITO on glass coated substrates were dried in oven at 50^{o}C and treated with UV-Ozone for 15 min. ZnO precursor sol-gel solution (0.45 M) was prepared by mixing 219.3 mg zinc acetate dehydrate ($Zn(CH_3CO_2)_2 \cdot 2H_2O$), 2 ml of 2-Methoxyethanol ($C_3H_8O_2$) and 73 mg of Ethanolamine ($HOCH_2CH_2NH_2$) and ultrasonicating at 55^{o}C for 15 min [73]. 14.4 mg ml^{-1} of the donor co-polymer PTB7-Th and 21.6 mg ml^{-1} of acceptor molecule PC71BM solution was prepared in o-dichlorobenzene and stirred overnight at 70^{o}C on a hot plate. Then 14.4 mg ml^{-1} PTB7-Th, 21.6 mg ml^{-1} PC71BM (1:1.5 wt. ratio) in o-dichlorobenzene and 3 % (in volume) 1,8-Diiodooctane (C8H16I2) was added and stirred for 3 h on a hot plate at 70^{o}C. The control biointerface was fabricated by spin coating ZnO precursor sol-gel solution at 2000 rpm for 60 s on a cleaned ITO coated on glass substrate and annealed on a hot plate at 290^{o}C for 15 min [74]. Further on ITO/ZnO substrate photoactive blend of PTB7-Th:PC71BM (1:1.5 wt. ratio) solution in o-dichlorobenzene was spin coated at 600 rpm for 200 s, then dried under nitrogen flow for 15 min and heated at 100 ^{0}C for 5 min. Plasmonic biointerface was fabricated on a control biointerface by coating 5 nm of Au using thermal evaporator (Bruker) at the rate of 0.02-

0.03 nm / s under 6.0 x 10^{-6} mbar vacuum pressure. Due to thin layer of gold forming nanoislands even at room temperature, it is annealed at 100^{o}C, which is maximum temperature that photoactive layer can withstand, before its optical properties deteriorating (Figure 3.4).

3.2 Optical and microscopic characterization

The optical absorbance for biointerfaces was carried out using a UV-Vis spectrophotometer (in our lab). The microscopic images photoelectrode surfaces were investigated using atomic force microscopy (AFM) (KUYTAM). Scanning electron microscopy was used to take cross-sectional images for the optimization of various layer thicknesses (KUYTAM).

3.3 Electrochemical measurement

To study the interfacial charge transfer processes, impedance spectroscopy (IS) measurements are carried on biointerfaces with different photoactive layers interfaced with electrolyte medium under light condition. It involves measuring the electrical impedance and phase angle obtained with sinusoidal voltage excitation of the electrode. The electrochemical impedance spectroscopy (EIS) in frequency response analysis (FRA) potential scan mode were performed on an Autolab Potentiostat Galvanostat PGSTAT (Metrhom, Netherlands). The measurement is made over a broad frequency range, between 1 to 10^5 Hz, and the samples are probed under 10 mV (V_{rms}) AC perturbation at zero dc bias under light conditions (at a wavelength of 470 nm with an intensity level of 10-50 mW cm^{-2}). The magnitude of the AC perturbation is kept sufficiently small so that a linear current-voltage response is obtained at each frequency.[75] Using IS, multiple charge carrier accumulation and charge transport can be distinguished at various interfaces in the device according to their response against an externally applied AC signal. For quantitative analysis, the impedance data are modeled using an equivalent electrical circuit with the circuit elements, which are assigned to

various physical phenomena in the device.[58, 73, 76, 77] The fitted parameters allow us to calculate the capacitance between the photoelectrode/electrolyte (extracellular medium) interface.[43] In order to measure photocurrent and photovoltage, we utilized the 2-probe configuration of electrochemical measurement in short-circuit condition keeping 0 V bias between working and counter electrode. The photoactive area of 1 cm^2 was fixed by using Redoxme Spectro-EFC cell set-up.

Using the macro-electrical parameters obtained by fitting, the driving electrical parameters in the bulk of the biointerface such as effective lifetime (τ_n) and mobility (μ_n) of charge carriers can be estimated using following equations;

$$C_\mu = \frac{(Y_0 R_{rec})^{\frac{1}{n}}}{R_{rec}} \tag{6.1}$$

$$\tau_n = R_{rec} C_\mu \tag{6.2}$$

$$\tau_d = r_t C_\mu \tag{6.3}$$

$$D_n = \frac{L^2}{\tau_d} \tag{6.4}$$

$$\mu_n = eD_n / k_B T \tag{6.5}$$

Where Cμ the chemical capacitance corresponds to carrier accumulation in the bulk, τ_d the electron diffusion time, D_n the diffusion coefficient of electrons, L the photoactive thin film thickness, and k_BT the thermal energy.

3.4 Photocurrent measurement

Further, the photocurrent measurements were performed on a set up including an Olympus T2 upright microscope. An extracellular patch clamp (EPC) 800 patch clamp amplifier (HEKA Elektronik) is used for measuring photocapacitive currents. The

experiment was carried out at room temperature in an extracellular aCSF aqueous medium as supporting electrolyte solution. Extracellular medium (aCSF) was prepared by mixing 10 mM of 4-(2-hydroxyethyl)-1-piperazineethanesulfonic acid (HEPES), 10 mM of glucose, 2 mM CaCl2, 140 mM of NaCl, 1 mM of MgCl2, 3 mM of KCl, into the distilled water and pH was calibrated to 7.4 using 1M NaOH. For the light stimulation, Thorlab's blue LED (M450LP1) with nominal wavelength of 445 nm was varied between 165 µW. cm^{-2} – 169 mW. cm^{-2}, green LED (M530L3) with nominal wavelength of 530 nm was varied between 89 µW. cm^{-2} – 41 mW. cm^{-2} and with nominal wavelength of 630 nm was varied between 64 µW. cm^{-2} – 85 mW. cm^{-2} (Figure A3.2, A3.3). All LEDs were driven by DC2200 - High-Power 1-Channel LED Driver with Pulse Modulation (Thorlab's). A power meter (Newport 843-R) was used to measure the exact power of light reaching the surface of biointerface. The illumination was focused at water immersion objective holder from the photoactive layer side of the biointerface. Illumination area was 1 cm^2. The biointerface corners were cleaned with toluene to stabilize the photocurrent measurements. (Figure 3.5)

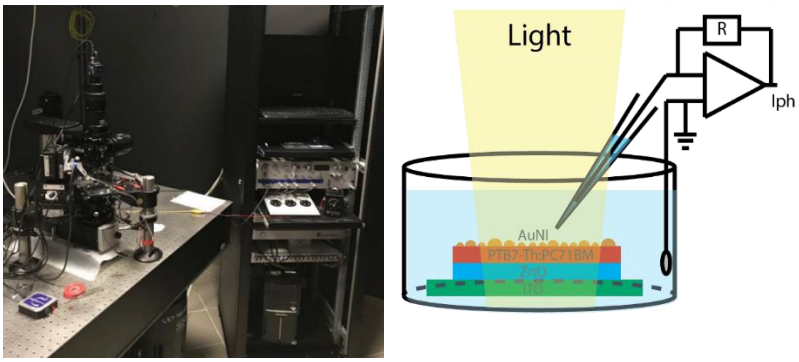

Figure 3.5 Left: Patch clamp system and measurement schematic. Right: Schematic of photocurrent measurement

3.5 Neural compatibility assessments

3.5.1 Cytotoxicity Assessment

Biocompatibility of the photoelectrodes were assessed by measuring the mitochondrial activity of SH-SY5Y cells using MTT assay. The photoelectrodes and ITO control were sterilized by 70% ethanol and 30 min UV exposure. In a 6-well plate, 0.3×10^6 SHSY-5Y cells were seeded onto samples and incubated at 37°C and 5% CO_2. Cytotoxic control samples were prepared with ITO samples that were incubated with growth medium containing 10% dimethyl sulfoxide (DMSO). After 48 hours, growth medium was discarded and 1 mg/ml 3-(4,5-Dimethylthiazol-2-yl)-2,5-diphenyltetrazolium bromide (MTT) was added in serum-free DMEM medium. Samples were incubated with MTT solution for 4 h to allow formazan formation. Finally, MTT solution was removed and formazan salts were dissolved with EtOH/DMSO. The amounts of formazan are measured with a microplate reader (BioTek, Synergy H1) in a 96-well plate. Relative absorbance of photoelectrode samples to ITO control is calculated to determine the relative biocompatibility.

3.5.2 Immunolabeling and Fluorescence Microscopy

SH-SY5Y cells were grown on the pre-sterilized substrates in a 6-well plate as explained under ‘cytotoxicity assessment’ section. After 48 h incubation at 37°C in a 5% CO_2 incubator, growth medium was discarded. For cell fixation, 4% paraformaldehyde was added in phosphate-buffered saline (PBS) solution and samples were incubated at 37°C for 30 min. Fixed cells were rinsed three times with PBSt (PBS containing 0.1% TritonX) and then blocked with PBSt containing 5% bovine serum albumin. Anti-beta III tubulin (ab78078, Abcam) primary antibody was used as neuronal marker labelling the cytoskeleton of SH-SY5Y cells. Samples were incubated with anti-beta III tubulin antibody for 2 h and washed three times with PBSt. Alexa Fluor conjugated goat anti-mouse IgG H&L (ab150113) was used as secondary antibody and DAPI stain was used to detect nuclei. After 1 h incubation with secondary antibody and DAPI, samples were

washed with PBSt and mounted by Mowiol. Imaging was performed with a fluorescence microscope (Zeiss-ObserverZ1).

3.5.3 Cytotoxicity Assessment

Biocompatibility of the photoelectrodes were assessed by measuring the mitochondrial activity of SH-SY5Y cells using MTT assay. The photoelectrodes and ITO control were sterilized by 70% ethanol and 30 min UV exposure. In a 6-well plate, 0.3×10^6 SHSY-5Y cells were seeded onto samples and incubated at 37°C and 5% CO_2. Cytotoxic control samples were prepared with ITO samples that were incubated with growth medium containing 10% dimethyl sulfoxide (DMSO). After 48 hours, growth medium was discarded and 1 mg/ml 3-(4,5-Dimethylthiazol-2-yl)-2,5-diphenyltetrazolium bromide (MTT) was added in serum-free DMEM medium. Samples were incubated with MTT solution for 4 h to allow formazan formation. Finally, MTT solution was removed and formazan salts were dissolved with EtOH/DMSO. The amounts of formazan are measured with a microplate reader (BioTek, Synergy H1) in a 96-well plate. Relative absorbance of photoelectrode samples to ITO control is calculated to determine the relative biocompatibility.

3.6 Cell growth

3.6.1 SHSY-5Y growth

SHSY-5Y cell line was used throughout the experiments. SHSY-5Y cells were cultured in Dulbecco's Modified Eagle's Medium (DMEM, Gibco 21969-035) supplemented with 10% fetal bovine serum (FBS, Gibco 10500), 1% L-glutamine (Gibco, 25030−081), and 1% penicillin−streptomycin (Gibco 15240-062). Cultures were maintained at 37 °C in a 5% CO2, 85% humidified incubator. Cells were passaged and supplied with fresh medium every 2-3 days.

3.6.2 Primary Hippocampal Neuron Isolation and Culture

Hippocampal regions were extracted from decapitated E15-E17 Wistar Albino rats and were placed immediately in ice-cold Hank's Balanced Salt Solution (HBSS, Thermo Fisher Scientific, MA, USA). The hippocampi were incubated in %0.25 Trypsin-EDTA solution (Thermo Fisher Scientific, MA, USA) with %2 DNase-I supplement (NeoFroxx, Einhausen, Germany) for 20 minutes in a 37oC incubator. Then the cells were centrifuged and the supernatant was changed with Dulbecco's Modified Eagle Medium/Nutrient Mixture F-12 (DMEM/F12 Thermo Fisher Scientific, MA, USA) supplemented with %10 fetal bovine serum (FBS, Heat Inactivated, GE Healthcare, IL, USA) and %1 penicillin/streptomycin (Thermo Fisher Scientific, MA, USA). DMEM/F12 was removed and Neurobasal Medium (NBM, Thermo Fisher Scientific, MA, USA) supplemented with B27, L-glutamine, β-mercaptoethanol, glutamate (Thermo Fisher Scientific, MA, USA) was added to the cell pellet. The cells were triturated and were passed through a 70 µm cell strainer. The homogenous cell solution was seeded in poly-D-lysine (PDL, Sigma-Aldrich, MO, USA) coated substrates. After 3-days incubation of cells on substrates in a 37 ^{0}C incubator with %5 carbon dioxide, the media of the cells on substrates were changed with NBM supplemented with cytosine arabinoside (Sigma-Aldrich, MO, USA) to inhibit growth of glial cells. After 24-hour incubation with cytosine arabinoside, the media were changed with NBM and the substrates with the hippocampal neurons used for experiments.

3.7 Electrophysiology measurement

The photostimulation was performed on a set-up comprising of Olympus T2 upright microscope and was placed inside a Faraday cage to prevent electrical noises. EPC 800 patch clamp amplifier (HEKA Elektronik) was used for the photocurrent measurements. For the light stimulation, we used a blue light emitting diode (LED). A power meter (Newport 843-R) was used to measure the exact power of light reaching at the interface. The illumination was focused on water immersion objective (40x/0.8 W, inf/0/FN 26.5)

from the ITO (a transparent electrode) side of the photoelectrode. The pulled patch pipettes of 8-12 MΩ were used to perform the whole-neuron cells under Giga-Ohm seal. Extracellular solution (Artificial Cerebrospinal Fluid, aCSF) is prepared as; 140 mM NaCl, 3 mM KCl, 1 mM $MgCl_2$, 2 mM $CaCl_2$, 10 mM HEPES, 10 mM Glucose. Osmolarity adjusted to 290 mOsm and pH adjusted to 7.4 with NaOH. Internal cellular solution (ICS) is prepared as; 140 mM KCl, 2 mM $MgCl_2$, 10 mM HEPES, 10 mM EGTA, 2 mM Mg-ATP. Osmolarity adjusted to 270 mOsm and pH adjusted to 7.3 with KOH. ICS was used to fill the patch pipettes during the measurement. Olympus T2 upright microscope and a digital camera was used in the electrophysiology set-up to monitor the cells. The stimulations of the primary hippocampal neurons were effective up to 30 minutes and after that they lost their excitability because of the damage by patched microelectrode.

3.8 Optical safety considerations

According to ocular safety standards for ophthalmic applications, the maximum permissible radiant power (MPF) that could enter the pupil chronically or in a single short exposure is calculated. For single-pulse exposures (pulse width of 10ms) at 400 - 700 nm, the peak limit is governed by the equation $MPF = 6.93 \times 10^{-4} C_T C_E t^{-0.25}$, where, t = 10 ms (pulse width), $C_T = 1$ in the range of 400–700 nm and C_E is a function of the visual angle α. For retinal spot sizes greater than 1.7 mm, $\alpha = \alpha_{max} = 100$ mrad and $C_E = 6.67 \times 10^{-3}\ \alpha^2 = 66.7$ W. For 10 ms pulse width MPF = 146.17 mW. For a pupil size with diameter 1.7 mm MPF per unit area is $MPF_{per\ unit\ area} = 6443$ mW. cm^{-2}.

Chapter 4: Band Alignment Engineers Faradaic and Capacitive Photostimulation of Neurons Without Surface Modification

(Reprinted (adapted) with permission from Srivastava, S. B., **Melikov, R.,** Aria, M. M., Dikbas, U. M., Kavakali, I. H., & Nizamoglu, S. (2019). Band Alignment Engineers Faradaic and Capacitive Photostimulation of Neurons Without Surface Modification. *Physical Review Applied*, *11*(4), 044012. Copyright 2019 The American Physical Society (APS).[58])

Here, we demonstrate that the intermediate layer can directly control the strength of the capacitive and Faradaic processes under physiological conditions. To resolve the Faradaic and capacitive stimulation we enhanced photogenerated charge density levels by incorporating PbS quantum dots into P3HT-PCBM blend. This enhancement stemmed from the simultaneous increase of absorption, well matched band alignment of PbS quantum dots with P3HT-PCBM and smaller intermixed phase separated domains with better homogeneity and roughness of the blend. These improvements led to the photostimulation of neurons at low light intensity level of 1 mW cm^{-2} within the retinal irradiance level. These findings open-up a new approach towards superior neural prosthesis.

4.1 Band alignment in bulk heterojunction solar cell and photoelectrode characterization

To fabricate photoelectrode we use an active layer made of P3HT and PCBM as the donor and acceptor molecules because it is one of the most widely studied and successful

photovoltaic blend, which has been proven to stimulate neurons grown on the bio-interface (Section 4.8) [25, 29, 31, 33]. The bulk heterojunction (BHJ) mechanism has an advantage of separating excitons and reduces the recombination process. Into this blend, we add PbS quantum dots that can absorb the entire visible and near IR spectral range (Figure 4.6). The use of PbS QDs in the bulk heterojunction increased the absorbance from 0.15 to 0.17 (Figure 4.1(a)), which corresponds to a net absorption increase of 3% at the wavelength of blue pump source (450 nm). The photocurrent enhancement (Figure 4.1(b)) is 5-fold, significantly above the absorption increase. In order to understand the reason, the surface morphology was measured for P3HT:PCBM and P3HT:PbS QDs:PCBM thin films using atomic force microscopy (shown in Figure 4.1(c) and 4.1(d)). We found out that the surface image of P3HT:PbS QDs:PCBM thin film exhibits smaller intermixed phase separated domains with better homogeneity and roughness, which is crucial for effective charge separation and collection [76]. In addition, the energy levels of the PbS quantum dots match with donor and acceptor molecules for dissociation of the photogenerated excitons (Figure 4.2). The energy levels for each photovoltaic material confirmed by cyclic voltammetry measurements and optical band gap (Figure 4.6). Hence, the synergistic approach of band alignment, absorption, and enhanced morphology improved the amount of charge carriers generated by the photoactive layer to clearly identify the stimulation mechanisms [78, 79].

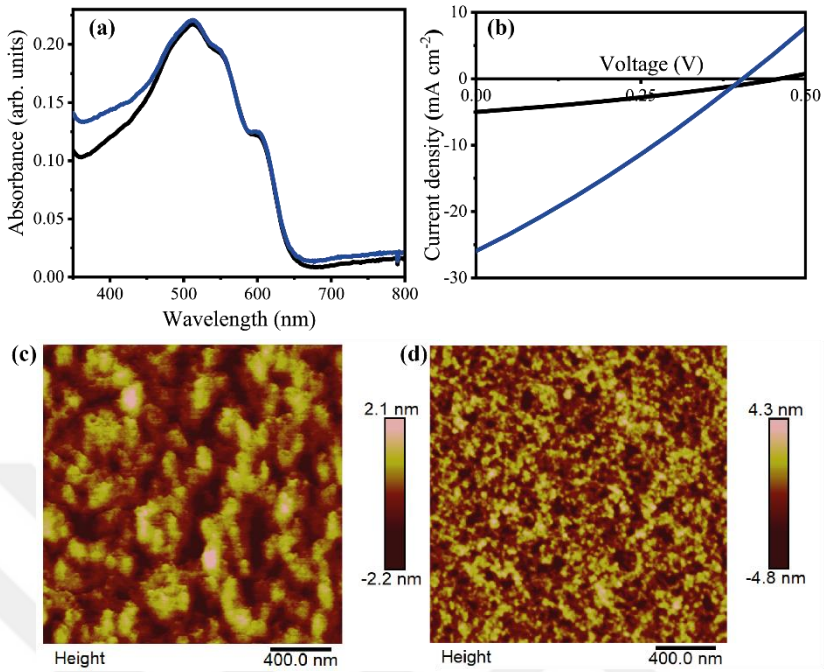

Figure 4.1: (a) UV-Vis spectrum of P3HT:PCBM (black line) and P3HT:PbS-QDs:PCBM thin films (blue line). (b) Current-voltage characteristics of P3HT:PCBM (black line) and P3HT:PbS-QDs:PCBM (blue line) based solar cells under AM1.5G solar illumination of 100 mW cm-2. Solar cell structures are ITO/ZnO/P3HT:PCBM/MoOx/Ag and ITO/ZnO/P3HT:PCBM:PbS-QDs/MoOx/Ag. (c) Surface height profile of P3HT:PCBM thin film and (d) P3HT:PbS-QDs:PCBM thin film for 2 µm × 2 µm scan area.

For photoelectrode characterization in physiological media, we fabricated three different photoelectrode configurations with intermediate layers sandwiched between P3HT:PbS QDs:PCBM bulk heterojunction photoactive layer and bottom electrode (ITO) (Figure 4.2(a)). We control the charge transfer mechanisms from the substrate to the cells by varying the intermediate layer between the photoactive layer and ITO. For the type I structure in Figure 4.2(b) consisting of the photoactive layer on ITO, a dominant Faradaic charge transfer mechanism is expected because the lowest unoccupied molecular orbital (LUMO) energy of the P3HT and PCBM is above the H^+/H_2 potential, and thus the photogenerated electrons can reduce the water molecules without any bias voltage [80]. To explore the possible Faradaic processes, we investigated the impedance spectroscopy (IS) under illumination (Figure 4.12), which can identify electrochemical charge accumulation and transport properties [73, 81, 82]. The impedance response of the

photoactive layer shows an Ohmic behavior between high to mid frequency range (Figure 4.12 inset), and then slowly changes to a depressed semi-circle at low frequencies in the complex plane. In the high frequency region, the bulk characteristic of the device shows Faradic nature. The impedance response was further simulated using an electrical equivalent circuit to get the physical parameters. We found out that while the charge storage at the electrode-electrolyte interface has a capacitance of 3.67 $\mu F.cm^{-2}$ in the equivalent circuit (Figure 4.13), the Faradaic impedance was low (31 kΩ) indicating an effective Faradaic charge-transfer mechanism. As expected, the photoelectrode showed a strong Faradaic photocurrent with a peak current level of 12.67 nA under the intensity of 1 mW cm^{-2} and pulse width of 10 ms (Figure 3.3(b)).

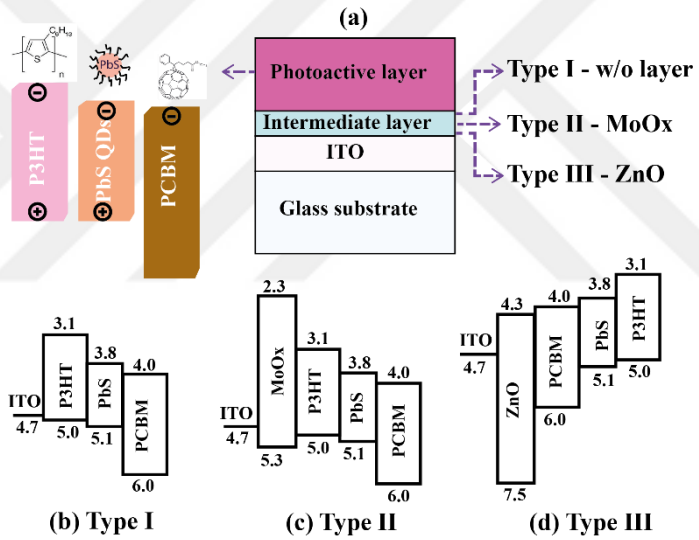

Figure 4.2: (a) Photoelectrode device architectures (Type I, II and III). In all of them P3HT, PbS quantum dots and PCBM blend is used for the photoactive layer. (b) Energy band diagram for ITO/P3HT:PbS QDs:PCBM (Type I), (c) ITO/MoOx/P3HT:PbSQDs:PCBM (Type II), and d) ITO/ZnO/P3HT:PbS QDs:PCBM (Type III).

One possible way to decrease the Faradaic charge transfer mechanism can be partially blocking the electron transport inside the photoelectrode. For that purpose, a MoOx is introduced in between the photoactive layer and ITO (Figure 4.2(c)), which behaves as a potential barrier for electrons. The impedance spectroscopy of the photoactive layer with MoOx also indicates a Faradaic charge-transfer based current injection, but due to the

potential barrier by MoOx layer, the Faradaic current is significantly reduced to 0.95 nA (Figure 4.3(c)). This is also supported by the increase of the Faradaic resistance (82 kΩ) between the electrode and electrolyte under illumination.

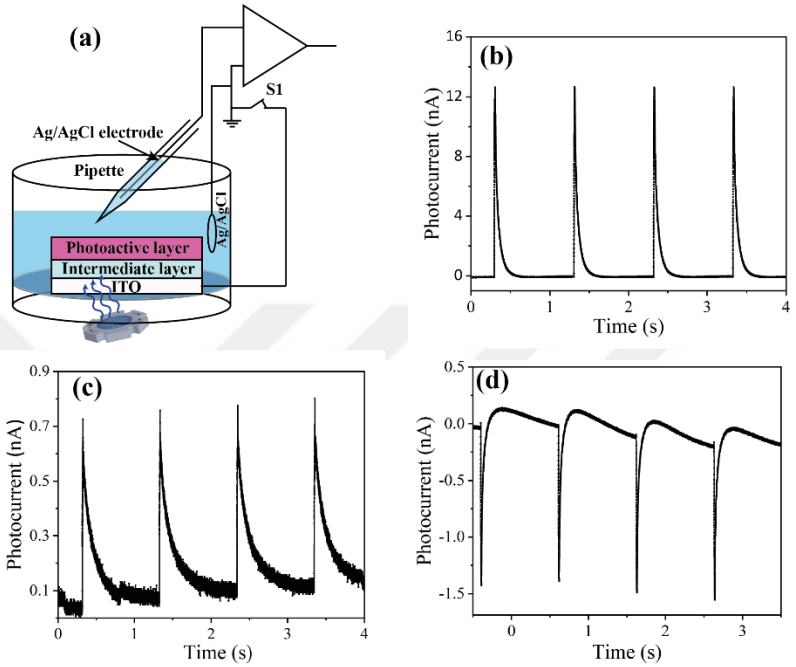

Figure 4.3: Photocurrent generated by the photoelectrodes while ITO is grounded. (a) Schematic of the photocurrent measurement setup. The patch pipette was kept close to the surface and the current was measured with a patch-clamp electrode. (b) Photocurrent vs. time for ITO/P3HT:PbS-QDs:PCBM photoelectrode (Type I), (c) ITO/MoOx/P3HT:PbS-QDs:PCBM photoelectrode (Type II), and (d) ITO/ZnO/ P3HT:PbS-QDs:PCBM photoelectrode (Type III).

To design an electrode with enhanced capacitive charge transfer, the carriers need to be localized close to the interface that can allow strong Coulomb interaction with the ions in the electrolyte. At the same time, these charges need to have an energy level that will not undergo a Faradaic reaction. Since highest occupied molecular orbital (HOMO) energy of the P3HT is above the water oxidation energy, Faradaic process due to hole transfer is limited (Figure 4.13). Therefore, the holes in the photoactive layer need to be positioned close to the electrode-electrolyte interface. Furthermore, from the above-discussed photoelectrodes, we know that the electrons in the photoactive layer can generate

Faradaic reaction. Because of that, the surface electron that can undergo a Faradaic mechanism needs to be moved away from the electrolyte interface and trapped inside the device. For that purpose, we replaced the MoOx layer with a ZnO layer (Figure 4.2(d)), and this type III configuration moved electrons toward the ITO layer and holes toward the electrode-electrolyte interface. Hence, in this structure, holes can effectively attract negative ions in the electrolyte to generate a displacement current.

To analyze the electrochemical behavior of the interface, we performed the impedance spectroscopy (Figure 4.11(a)). The impedance response for the devices under illumination shows a distinctive semi-circle in comparison with the Faradaic interfaces between high to mid frequency range (See Supplemental Material (Figure 4.11(a) inset), and then slowly changes to a depressed semi-circle at low frequencies in the complex plane. In the high frequency region, the bulk characteristic of the photoelectrode shows a capacitive nature. The observed capacitance and Faradaic impedance at the interface were found 5.47 $\mu F.cm^{-2}$ and 0.16 MΩ, respectively, which are higher than the Faradaic devices. These electrochemical properties support the enhanced capacitive nature of the photoelectrode by using ZnO as the intermediate layer. For further clarification, the Bode modulus and Bode phase was plotted against frequency (Figure 4.11(b)). The Bode phase at high frequency is generally interpreted as the electrolyte region, and the region in kHz frequency corresponds to the double layer at the photoelectrode-electrolyte interface. At this frequency, we comparatively observed significantly higher phase angle, which indicates strong capacitive response.

We measured the photocurrent of the electrode inside the aCSF solution under the same light intensity of 1 mW cm^{-2} and 10 ms pulse width. Since holes migrate in the direction of P3HT, the direction of the initial spike is reversed in comparison with the Faradaic electrodes. Hence, the hole cloud in the P3HT attracts the negative ions in the electrolyte. Because of the double layer generation on the electrode-electrolyte interface and the additional serial capacitances of the accumulation at interfacial layer [83], a positive voltage rise between electrolyte and electrode induces a current flow from the electrode

toward electrolyte. After 10 ms pulse, there is a decreasing slope, which now induces a current generation from electrolyte to electrode. The slower kinetics in the displacement current from electrolyte to electrode is possibly due to slower recombination of the carriers in the photoactive layer. Moreover, while we integrate the area under the time-dependent photocurrent, it approximately approaches to zero, which also proves that total number of charges are conserved meaning that the current is generated due to the redistribution of surface charges, not due to either electron or hole tunneling between the electrode and electrolyte. Furthermore, to confirm the key role of bandgap engineering on charge-transfer control, we experimentally tested both adding a thin tunneling layer of 1-nm MoOx between conductive and photoactive layer or tuning the conductivity by adding a 1-nm gold (Au) layer (Figure 4.16(a)). In both cases, Faradaic current was observed (Figure 4.16(b) and (c)), which confirms the importance of band alignment to obtain strong capacitive effects. This approach, which offers an alternative to the variation in physical dimensions, metal doping and surface chemistry [45], advantageously allows for the design flexibility that after the optimization of the photoactive layer for the effective transduction of photons to charge carriers, the inner layers can be engineered for optimized and targeted stimulation mechanisms.

4.2 Charge transfer mechanism in biological media in a wireless, free-standing mode

We next investigated charge transfer mechanisms in biological media in free-standing mode close to the realistic situation of neural stimulation condition. In this case, the photocurrent was measured with a micropipette electrode close to the photoelectrode in aCSF solution. In this set-up configuration, the bath solution was grounded with an Ag/AgCl reference electrode without any wiring to the ITO electrode (Figure 4.4(a)). This setup reflects the working conditions of a standalone implantable device. We

measured the photoresponse of type I, type II and type III photoelectrodes in this mode under blue LED light pulses having the intensity of 1 mW cm^{-2} and the pulse width of 10 ms (Figure 4.4(b)) and quantitatively analysed the contribution by capacitive and Faradaic components by using the approach Jiang *et al.* [45]. Type III photoelectrode was specifically designed for strong capacitive photocurrents and it exhibited capacitive current level of 1.02 nA, which is at least 10-fold higher than the other photoelectrodes. The Faradaic photocurrent is less than 0.5% for type III photoelectrode, almost negligible, showing that major contribution comes from the capacitive photocurrent (Figure 4.4(c) inset). In this mode the Faradaic currents by type I and type II were significantly lowered and a low level of capacitive photocurrents that correspond to 0.10 nA and 0.05 nA were observed, respectively. Due to the effective collection of holes in the photoactive layer in type III photoelectrode, the capacitive current is also controllably reversed in comparison with the other photoelectrodes. Like in the solar cell measurements, the addition of PbS QDs to type III photoelectrodes enhanced the photocurrent approximately for 4 times.

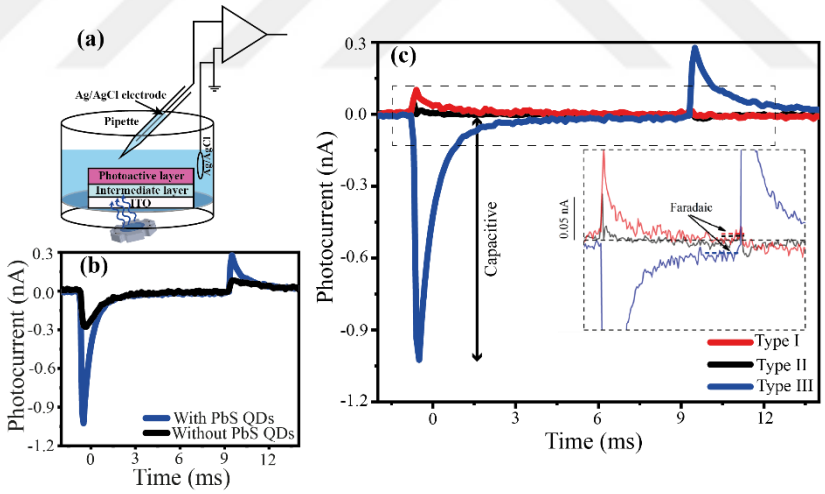

Figure. 4.4: (a) Photocurrent measurement configuration in free standing mode. aCSF solution was grounded with Ag/AgCl reference electrode. (b) Photocapacitive current levels of ITO/ZnO/P3HT:PCBM and ITO/ZnO/P3HT:PbS-QDs:PCBM photoelectrodes. (c) Capacitive and Faradaic components of type I, type II, and type III photoelectrodes under the illumination of 10 ms light pulses with an intensity of 1 mW cm-2.

4.3 Neuronal photostimulation

Initially we checked the biocompatibility of the photoelectrodes, and we observed that they have comparable cell viability with ITO control and the results suggest photoelectrodes didn't exhibit any toxic effect on the cells (Appendix-2). Patch-clamping in whole-cell configuration in current-clamp (I=0) was used to record cellular electrophysiology (Figure 4.5(a)) both for dark and under light conditions. Figure 4.5(b) shows a typical IV characteristic of a SHSY-5Y cell, which was measured with voltage clamp in dark condition. The cell has a quasi-linear response around the resting potential, as assumed in the two-domain-stimulation model (Section 4.6). Like in photocurrent experiments, light pulses with intensity level of 1 mW cm^{-2} and 10 ms pulse width was used for the photostimulation experiments. The electrophysiology experiment was performed in wireless, free standing mode.

Furthermore, organic substrates may also stimulate the neurons via photothermal or thermo-capacitive effects, which induces a depolarization due to phase transition in the phospholipid ordering and afterward it ignites a hyperpolarization due to the variation of the membrane conductance in the channels and rearrangement of the ions [84, 85]. To investigate the contribution of thermal effect, we calculated the temperature produced by light illumination. The maximum heat that can be induced for 1 mW cm^{-2} is less than 0.01^0C (Section 4.7), which is insufficient for photothermal stimulation of the cells. Moreover, the level of intensities that we used in this study is comparatively 2-orders of magnitude lower than the reports studying the thermal activation of neurons [36]. Even though the photoelectrochemical currents may not appropriate for long-term neural stimulation, they can be useful for short-term stimulation [86].

Alternatively, capacitive charge transfer mechanism presents a safe stimulation strategy by redistribution of the ion concentration in the electrolyte, which can be strongly generated by type III photoelectrode. Figure 4.5(c) shows the membrane potential response by type III photoelectrode after the illumination of light pulses showing an

initial depolarization (positive spike) of cell membrane followed by a slower transient repolarization. When the light was switch off after 10 ms, a complementary behavior of negative spike was recorded followed by a transient hyperpolarization before the cell membrane reached to the resting potential. This depolarization and hyperpolarization are an expected behavior due to the bi-directional current generation for each pulse during the rising and falling times of the light intensity. The peak depolarization for different illumination intensities are measured and at 0.2 mW cm^2 intensity levels can still lead to significant peak membrane depolarization (Figure 4.5(d)). It is also evident from the box plot that peak depolarization has variation from cell to cell and can be increased by increasing the light intensity under safe neural stimulation limits.

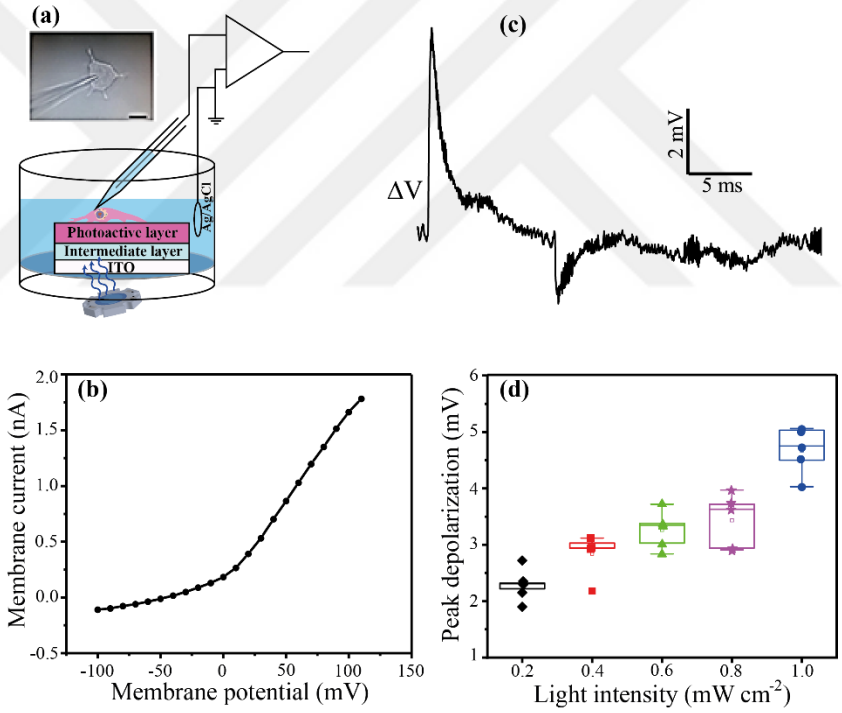

Figure. 4.5: Analysis of SHSY-5Y cell responses to 10-ms light pulses on type-III photoelectrode architecture (ITO/ZnO/P3HT:PbS-QDs:PCBM). (a) Schematic of the whole-cell patch-clamp recoding configuration of the photoelectrode in free-standing mode. The cells were grown on the photoelectrode and adhered on the polymer surface. A LED at far-field is used to illuminate and activate the photoelectrode. (b) Current-voltage characteristics of a typical SHSY-5Y cell under dark. (c) Membrane

potential variation upon light illumination (10 ms, 1 mW cm^{-2}). (d) Peak depolarization recorded for different light intensities (N=5).

4.4 Energy level calculation of photovoltaic materials

The energy levels of the photovoltaic materials (P3HT, PCBM, and PbS QDs) has been determined by cyclic voltammetry (CV) experiments. In this experiment, 0.1 M tetrabutylammonium hexafluorophosphate (TBAPF6) supporting electrolyte was dissolved in anhydrous acetonitrile solvent to make electrolyte solution. Next, we added ferrocene in the electrolyte as an internal reference. For CV measurement, a three-electrode set up consisting of Ag/AgCl as the reference electrode, platinum wire as the counter electrode and thin films of photovoltaic materials as working electrode were used. The highest occupied molecular orbital (HOMO) and lowest unoccupied molecular orbital (LUMO) levels can be estimated by oxidation (E_{ox}^{onset}) and reduction onset (E_{red}^{onset}) potentials of the materials using following equations;

$$E_{HOMO} = -e(4.8 - E_{Fc/Fc^+} + E_{ox}^{onset}) \quad (4.1)$$

$$E_{LUMO} = -e(4.8 - E_{Fc/Fc^+} + E_{red}^{onset}) \quad (4.2)$$

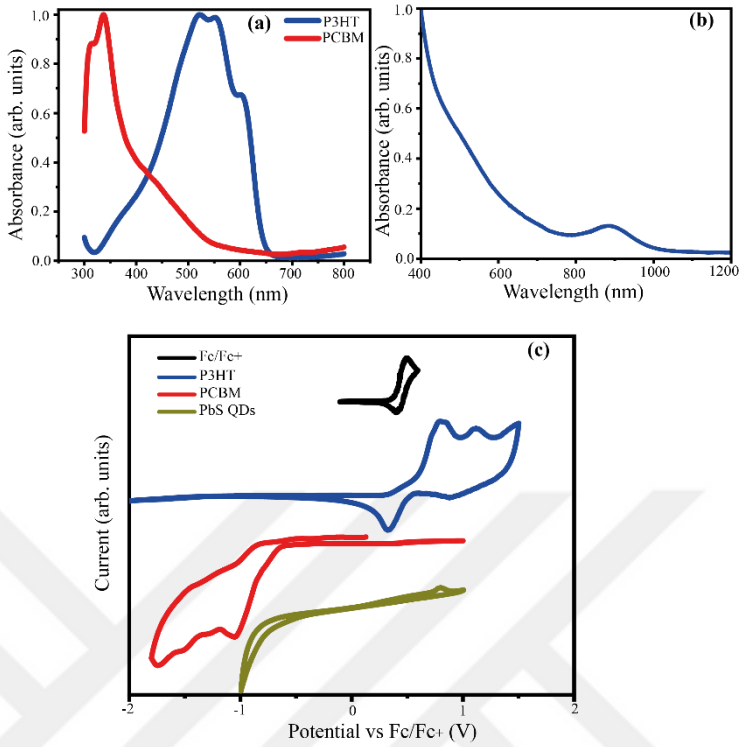

Figure 4.6: (a) Absorbance of photovoltaic materials P3HT and PCBM, (b) Absorption spectra of PbS colloidal quantum dots in toluene solvent, (c), Cyclic Voltammogram of photovoltaic materials (P3HT, PCBM, PbS QDs) with respect to Ferrocene (Fc/Fc+) as internal reference.

Where, E_{Fc/Fc^+} is half wave potential and was calculated to 0.11 V from the redox potential of ferrocene. During CV measurement, the redox reaction may not be observed together for each material. Hence, we have calculated the optical bandgap of 1.92 eV for P3HT, 2.03 eV for PCBM and 1.25 eV for PbS QDs using absorbance plot (Figure 4.6 (a) and (b)). The levels were calculated using equation 4.1, equation 4.2 and optical band gap (E_g) and HOMO/LUMO were determined as -5.01/-3.09 eV for P3HT, -6.04/-4.01 eV for PCBM and -5.11/-3.85 eV for PbS QDs.

4.5 Cell growth and Biocompatibility

SHSY-5Y cell line was used throughout the experiments. SHSY-5Y cells were cultured in Dulbecco's Modified Eagle's Medium (DMEM, Gibco 21969-035) supplemented with 10% fetal bovine serum (FBS, Gibco 10500), 1% L-glutamine (Gibco, 25030−081), and

1% penicillin−streptomycin (Gibco 15240-062). Cultures were maintained at 37 °C in a 5% CO2, 85% humidified incubator. Cells were passaged and supplied with fresh medium every 2-3 days.

Cytotoxicity assay was performed as described by Bahmani et. al. Briefly, photoelectrodes were cut into 0.40 × 0.40 cm square pieces; sterilized by 70% ethanol treatment and 30 minutes UV exposure. Sterilized substrates were placed into sterile 96-well plate and 1×10^4 SHSY-5Y cells were seeded onto substrates in 200 µL growth medium. Plate was incubated for 48 h in incubator under 37 °C in the presences 5% CO_2 incubator. Then, the growth medium was replaced with DMEM containing 1 mg/mL MTT solution (100 µL) and further incubated for 4 h at 37 °C to allow formazan formation. Subsequently, the MTT solution was removed and formazan salt was dissolved in EtOH/DMSO (200 µL). The amounts of formazan were measured with a microplate reader (BioTek, Synergy H1) in a clean 96-well plate. The relative cell viability was calculated as:

$$viability = (OD_{sample} / OD_{control}) \times 100 \quad (4.3)$$

The OD_{sample} was obtained from photoelectrodes and $OD_{control}$ was obtained from ITO control. The experiment was performed at least 3 biological replicates and each biological replicate consists of 9 technical replicates (n=3).

After the synthesis of the photoelectrodes we next investigated its effect on cell viability and cell growth of SHSY-5Y cells using MTT assay and tracking assay. As can be seen in Figure 4.7, cells grown on substrates had comparable viability compared with ITO control rather than 10% DMSO treated cells samples. These results suggested substrate didn’t exhibit any toxic effect on the cells.

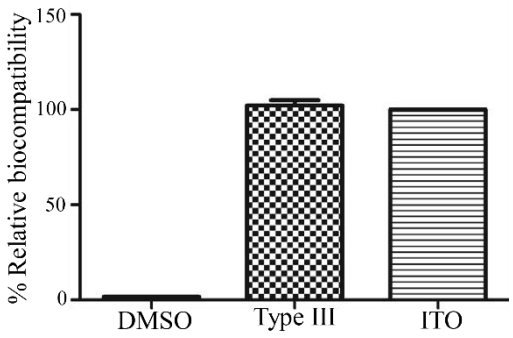

*Figure 4.7: The cell viability assessment of photoelectrodes on SHSY-5Y cell line. The effect of the photoelectrodes on metabolic activity of SHSY-5Y cells assessed by MTT. Data was presented in a column graph plotting the mean with the standard error of the mean (SEM). An unpaired two-tailed t test was performed to determine level of significance. *p < 0.05 was considered as statistically significant, and non-significant differences was presented as 'ns'.*

4.6 Two-domain-stimulation model

Neuron membrane potential is controlled by the inflow and outflow of ions, and to understand the effect of extracellular stimulation by the photoactive substrates on a nerve cell, we use a two-domain-stimulation model [21], which considers the polarization of the attached membrane on the substrate and free-membrane. The circuit diagram of two-domain-stimulation model is shown in Figure 4.8(a). Here we assume the equivalent circuit of the cell membrane as an RC circuit instead of HH model. This is due to the use of undifferentiated SHSY-5Y cells in our electrophysiology experiments, which generally operate under the sub-threshold regime. Moreover, we model the photoactive substrates as current sources that can generate current flow via Faradaic and capacitive mechanisms. Since we measured the current levels of each substrate on its surface with a distance between the patch pipette and the surface, in the equivalent circuit the effect of the leakage current due to cleft between a cell and substrate is assumed to be included in the current source. By writing the circuit via Kirchhoff's current law at intracellular medium node, the equation can be expressed as:

$$A_{fm}C_m\frac{dV_m}{dt}+A_{fm}\frac{V_m}{R_m}+A_{jm}I_{device}=0 \tag{4.4}$$

where V_m is the free membrane potential with respect to ground, $C_m = C_{fm}/A_{fm} = C_{jm}/A_{jm}$ is cell membrane capacitance, $R_m = R_{fm}\times A_{fm} = R_{jm}\times A_{jm}$ is the membrane resistance, A_{jm} is attached membrane area on the electrode, A_{fm} is the free membrane area, and I_{device} is the stimuli current generated by the photoactive surfaces. We also know that while a cell is not stimulated by an extracellular electrode, it will remain at its resting potential (V_{rest}), and thus, the initial and steady-state boundary conditions of membrane potential are V_{rest}.

The general solution of the equation 4.4 is given by:

$$V_m = V_{rest} - \frac{A_{jm}}{A_{fm}}R_m I_{device}(1-e^{(-t/(R_mC_m))}) \tag{4.5}$$

The transmembrane potential with respect to resting potential can be written as:

$$V_{trans} = V_m - V_{rest} = -\frac{A_{jm}}{A_{fm}}R_m I_{device}(1-e^{(-t/(R_mC_m))}) \tag{4.6}$$

We simulated the current-transmembrane potential for a single cell via extracellular excitation. Due to the linearity of an RC circuit we observe a linear response for different current injection levels (Figure 4.8(b)). The physical interpretation of this result is higher current will lead to stronger depolarization and hyperpolarization. Moreover, we also applied Faradaic and capacitive current waveforms into the model. For Faradaic currents we expect a hyperpolarizing behavior and relaxation to the resting state. For the capacitive currents, a depolarization is expected to be followed by a hyperpolarization (Figure 4.8 (c)).

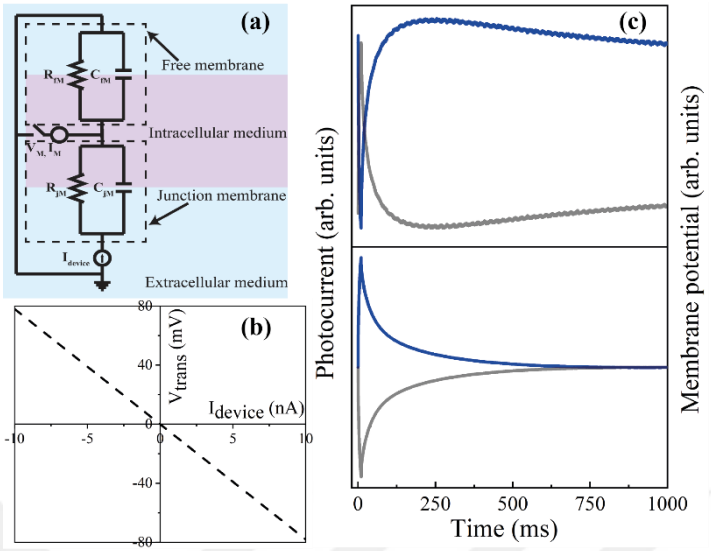

Figure 4.8: (a) Two-domain circuit representation of neuronal cell membrane in subthreshold condition. Blue part shows the extracellular region and the reddish part shows the intracellular region. (b) Simulated transmembrane potential under extracellular input current (I_{device}). The potential shows a linear response as a result of the injected current. (c) The output transmembrane potential waveforms (grey lines) as a response to the capacitive (top) and Faradaic (bottom) current waveforms that are used as the input (blue lines).

4.7 Thermal effect at neuron surface due to light illumination

From the thermodynamic relation,

$$d_q(rev, p) = mC_p dT \tag{4.7}$$

$$\int_0^q dq(rev, p) = mC_p \int_{295K}^{T} dT \tag{4.8}$$

Considering the water heat capacity $C_p = 75.291 JK^{-1}mol^{-1}$, we can calculate specific heat capacity as;

$$q = mC_p \Delta T \tag{4.9}$$

On the other hand, we can find the thermal energy (q) because of light illumination:

$$q = I \times t = 1s \times 1mW = 1 \times 10^{-3} J \quad (4.10)$$

Where I is the light illumination power equal to 1 mW and t is illumination time, 1s.

From equations (4.9) and (4.10);

$$1 \times 10^{-3} J = (0.0332g / 18g / mol) \times 75.291 JK^{-1} mol^{-1} \Delta T$$

$$\Delta T = 0.00728°C$$

4.8 Supporting information

Inverted binary and ternary organic photovoltaic devices were fabricated on patterned indium tin oxide (ITO) substrates with the configurations of ITO/ZnO/P3HT:PCBM/MoO_3/Ag and ITO/ZnO/P3HT:PbSQDs:PCBM/MoO_3/Ag, respectively. ITO coated glass substrates were cleaned using soap solution in de-ionized (DI) water for 15 minutes. The substrates were then rinsed with DI water, and sonicated in acetone and isopropanol, respectively. Next, the substrates were dried with N_2 gun, and treated with UV-ozone for 15 minutes. A sol-gel of ZnO (0.45 M) was prepared using zinc acetate dihydrate in 2-methoxyethanol and ethanolamine. The prepared solution was spin coated at 2000 rpm for 60 seconds to deposit ZnO thin film (~40 nm) on the substrate. A drying process was performed on a hot plate at 250°C for 15 minutes at room temperature. The P3HT and PCBM were used as it was received from Sigma Aldrich. The P3HT:PCBM binary blend was deposited by spin-coating a solution (26 mg/ml) of P3HT:PCBM (1:1) in o-dichlorobenzene at 2000 rpm for 60 seconds on top of ZnO layer. The P3HT:PCBM layer was dried at 150°C at hot plate for 15 minutes to remove the excess solvent. The thickness of the active layer used in these devices is ~100 nm. to complete the device, resulting a device area of approximately 0.04 cm^2.

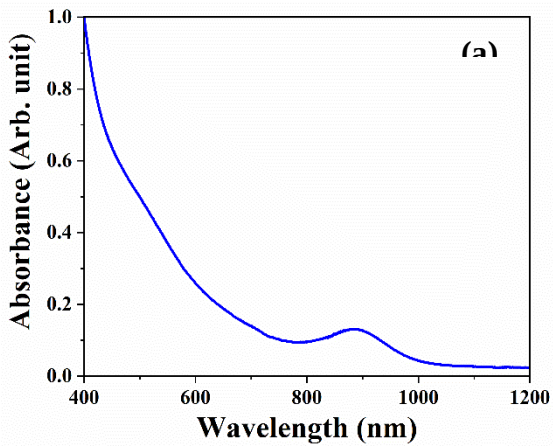

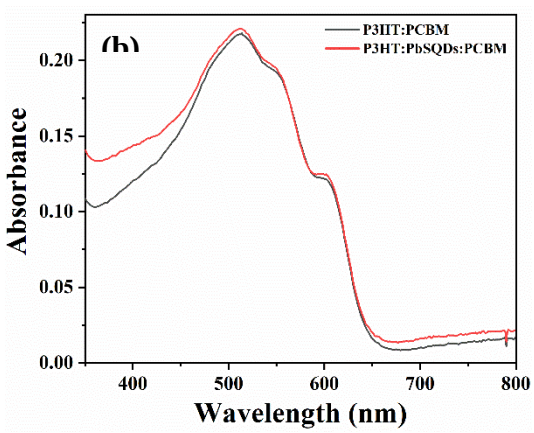

Figure 4.9: (a) Absorption spectra of PbS colloidal quantum dots in toluene solvent, (b) UV-Vis spectrum of PbS QDs, P3HT:PCBM, and P3HT:PbS QDs:PCBM thin films

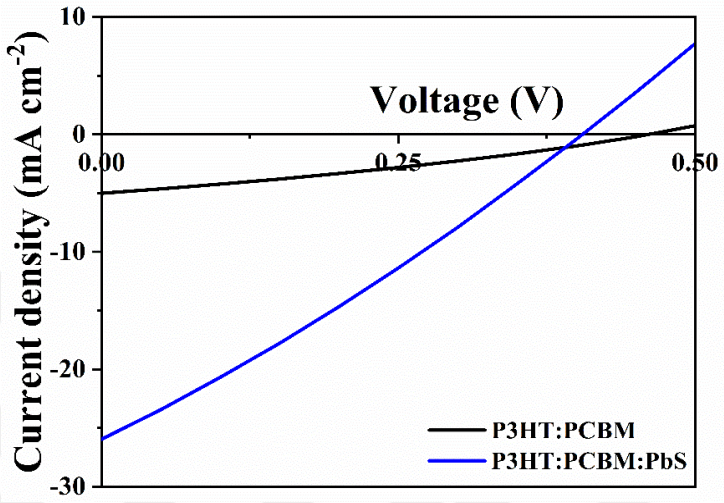

Figure 4.10: Current-voltage characteristics of P3HT:PCBM (black line) and P3HT:PCBM:PbS QDs (blue line) based solar cells under AM1.5G solar illumination of 100 mW cm^{-2}. Solar cell structures are as ITO/ZnO/P3HT:PCBM/MoOx/Ag for basic device, and ITO/ZnO/P3HT:PCBM:PbS QDs/MoOx/Ag after adding PbS QDs in the bulk heterojunction.

Similarly, we have deposited ternary blend (P3HT:PbSQDs:PCBM::1:0.17:1) in o-dichlorobenzene (26 mg/ml) at 2000 rpm for 60 seconds on top of ZnO layer and dried at 150^{o}C at hot plate for 15 minutes. 10 nm of Molybdenum tri-oxide (MoO_3), an electron blocking layer, was deposited on top of the active layer by thermal evaporation. A silver cathode (100 nm) was deposited by thermal evaporation through a shadow mask under a pressure of $\sim 10^{-6}$ mbar

Current density-voltage (J-V) characteristics of binary and ternary solar cells were measured under an AM1.5G illumination source (1000 Wm^{-2}) using a Solar Simulator. The light intensity was adjusted with a NREL calibrated Si solar cell. The Keithley 2400 source meter was used for the measurement of I-V characteristics of binary and ternary solar devices.

Current-voltage (J-V) characteristics were measured in room conditions is shown in Figure 4.10. We observed a significant improvement in the short circuit current density which can be attributed to the high electron mobility of PbS QDs in the active layer and better charge separation due to enhanced nanomorphology.

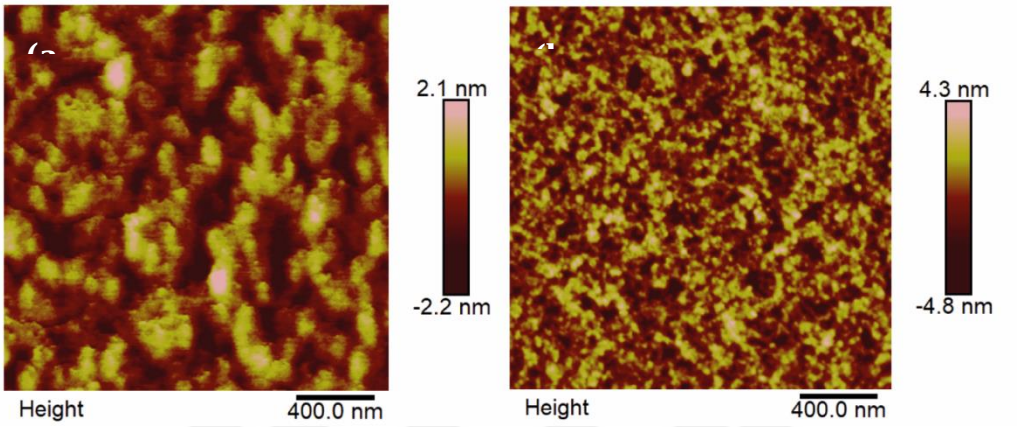

Figure 4.11: (a) Surface height profile of P3HT:PCBM thin film and (b) P3HT:PbS QDs:PCBM thin film for 2 µm × 2 µm scan area.

The photoactive layer thin film morphology is a crucial parameter for organic solar cells. The surface morphology was measured for P3HT:PCBM and P3HT:PbS QDs:PCBM thin films using atomic force microscopy for 2 µm × 2 µm scan size (shown in Figure 4.11 (a) and (b)). The cluster structure with large aggregated domains was observed with average roughness of 0.51 nm for P3HT:PCBM thin film. However, the surface image of P3HT:PbS QDs:PCBM thin film exhibits smaller intermixed phase separated domains with better homogeneity, and average roughness was found 1.03 nm. The surface roughness of the thin film is also a critical parameter while interfacing with another layer (electrode) to get enhanced charge collection, which is better for P3HT:PbS QDs:PCBM thin film [1]. It is crucial to have the interpenetrating nanomorphology of the bulk heterojunction for better charge separation and transport. The homogeneous structure may be evolved because of the differential kinetics of the PbS QDs in the bulk heterojunction.

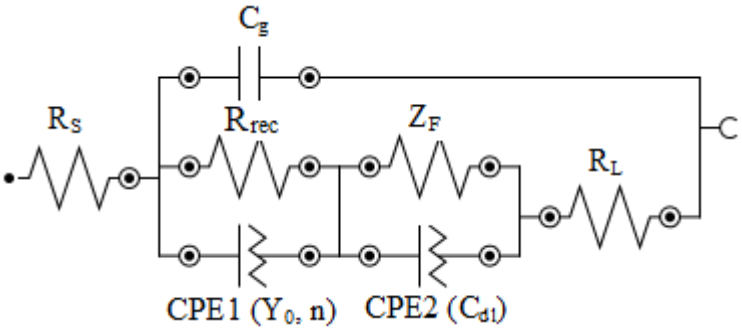

Figure 4.12: The equivalent circuit of the photoelectrode measured by 3-electrode configuration. Each electrical parameter signifies to physical attributes of the photoelectrode. Where, R_s is the series resistance due to probing electrodes, C_g is the characteristic capacitance of the photoelectrode, R_{rec} in parallel to the constant phase element CPE1 signifies the recombination process of charge carriers in the photoactive layer, Z_F represents Faradaic resistance at the electrode-electrolyte interface, CPE2 signifies the capacitive nature of the electrode-electrolyte interface which works parallel to the Z_F, and R_L represents the leakage resistance of electrolyte media.

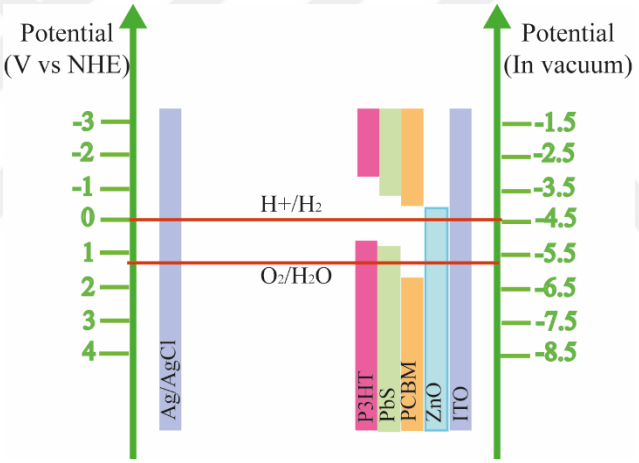

Figure 4.13: Representative diagram of the band edge positions of the photoelectrode and water splitting potential edge (red line)

The LUMO of our photoactive layer is above the H^+/H_2 potential, shown in Figure 4.13 [3]. Hence, the surface electrons of the photoactive layer can move to the aqueous liquid, reduce water and generate Faradaic photocurrent. By properly engineering the intermediate layer between the photoactive and conductive layer, we lead the electron accumulation more toward the inside of the device (ITO side), which decreased the transfer of the surface electrons to the solution. We did the analysis of the Faradaic and capacitive contribution by using the temporal analysis proposed by Jiang *et al* [2] in the

same experimental configuration and because of the optoelectronic of the biointerface, the Faradaic current ratio is decreased to less than 2%.

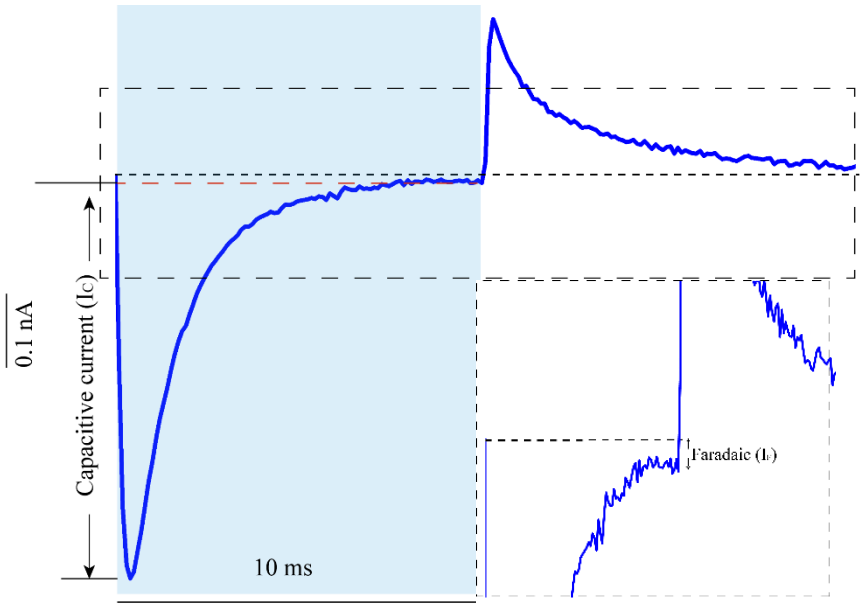

Figure 4.14: Photocurrent of ITO/ZnO/P3HT:PbS QDs:PCBM photoelectrode shows capacitive and Faradaic components under the illumination of 10-ms light pulses (shaded area) with an intensity of 1 mW cm^{-2}. The measurements are done while the switch is open as described by Jiang et al [2].

The quantitative capacitive/Faradaic response was extracted from the temporal response of the photoelectrode at 10 ms light pulse, according to the report by Jiang *et al* [2]. In Figure 4.14, the capacitive and Faradaic part of the photocurrents are shown. Capacitive photocurrent (I_C) of 0.47 nA was observed along with 9 pA of Faradaic current at the time point of 8.5 ms after the light pulse onset, which shows that in our capacitive biointerface the Faradaic contribution to the overall photocurrent is less than 2%. In addition, the thermal response is negligible because of low illumination intensity (1 mW.cm^{-2}).

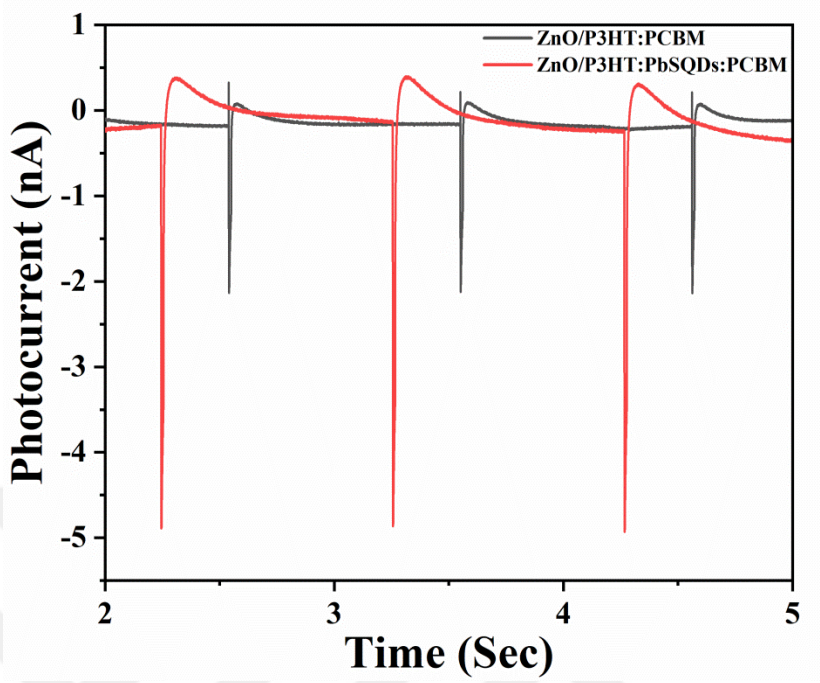

Figure 4.15: Photocurrent comparison of photoelectrodes with and without PbS QDs in the organic active layer. The thin films are illuminated with light pulses having the intensity of 1 mW.cm^{-2} and the pulse width of 10 ms with a repetition rate of 1 second.

We prepared two capacitive substrates having P3HT:PCBM photoactive layer with and without QDs. By incorporating QDs into the P3HT:PCBM the capacitive photocurrent increased from -1.97 nA to -4.70 nA.

The bandgap engineering is critical to control Faradaic and capacitive photocurrent. In order to confirm, we experimentally tested both adding a thin tunneling layer of 1-nm MoO_x between conductive and photoactive layer or tuning the conductivity by adding a 1-nm gold (Au) layer (Figure 4.16(a)). In both cases, Faradaic current was observed (Figure 4.16 (b) and (c)), which confirms the importance of band alignment to obtain capacitive photocurrent.

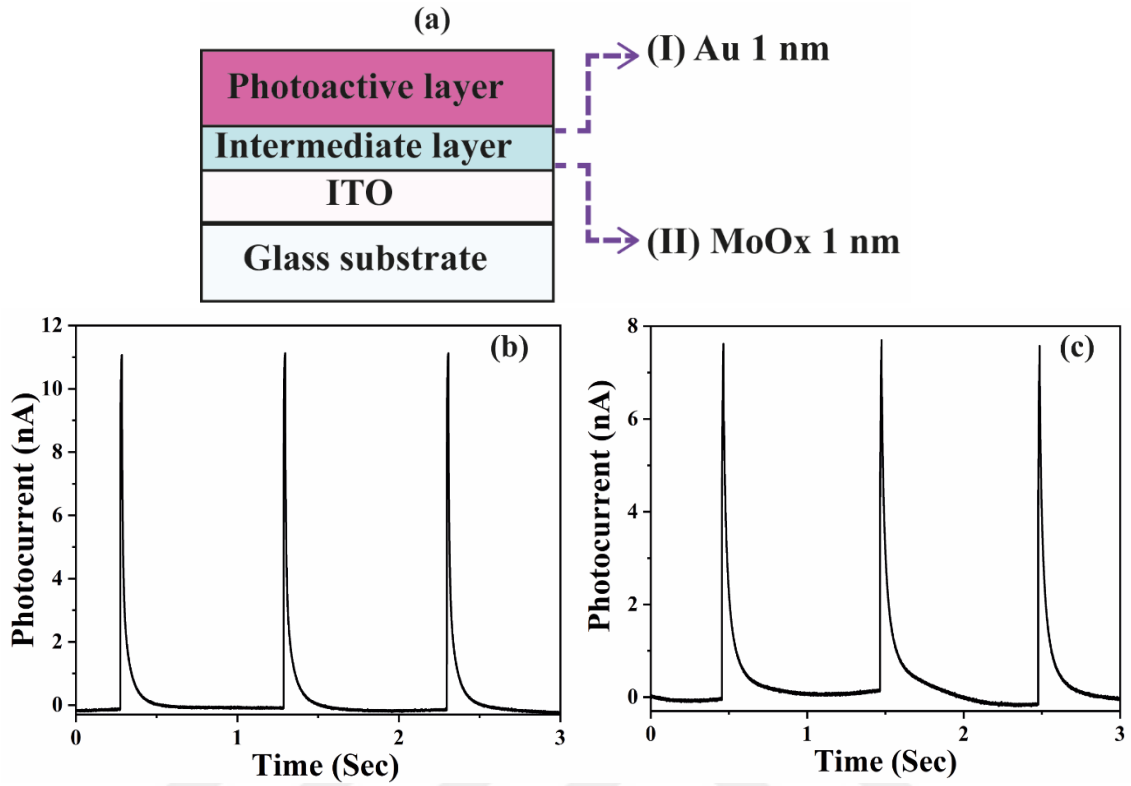

Figure 4.16: (a) The device schematic showing thin tunneling layer between conductive and photoactive layer. (b) Photocurrent vs. time for ITO/Au/P3HT:PbS QDs:PCBM photoelectrode. (c) Photocurrent vs. time for ITO/MoOx/P3HT:PbS QDs:PCBM photoelectrode. The thin films are illuminated with light pulses having the intensity of 1 mW.cm-2 and the pulse width of 10 ms with a repetition rate of 1 second.

Chapter 5: High-V_{oc} Optoelectronic Biointerface for Improved Capacitive Charge Transfer

(Reprinted (adapted) with permission from Srivastava, S. B., **Melikov, R.,** Yildiz, E., Dikbas, U. M., Sadeghi, S., Kavakali, I. H., Sahin, A. & Nizamoglu, S. (2020). Bulk-heterojunction photocapacitors with high open-circuit voltage for low light intensity photostimulation of neurons. *Journal of Materials Chemistry C,*. Copyright 2020 The Royal Society of Chemistry (RSC).)

Dr. Srivastava and Mr. Melikov contributed equally.

Here, we developed a single-junction, wireless and capacitive-charge-injecting optoelectronic biointerface with negligible Faradaic reactions by using a high open-circuit voltage (0.75 V) bulk heterojunction of PTB7-Th:PC71BM are designed and demonstrated. The biointerface generates 2-fold higher photocurrent in comparison with P3HT:PC61BM having an open-circuit voltage of 0.55 V. Further, we observed that light intensity that is logarithmically correlated with open-circuit voltage of solar cells and photovoltage of the biointerfaces varies switching speed of capacitive charge-transfer. Finally, pulse trains of capacitive stimuli at low light intensity of 20 mW cm^{-2} elicit action potential generation in primary hippocampal neurons extracted from E15-E17 Wistar Albino rats. These findings show great promise of high open-circuit voltage bulk heterojunction biointerfaces for non-genetic, all-optical and safe modulation of neurons.

5.1 Photocapacitor Biointerface Structures

Light-induced capacitive charge-transfer is a safe method for neural photostimulation. For capacitive charge-transfer the photogenerated charge carriers need to be dissociated and directed toward the semiconductor-electrolyte interface to induce a displacement

current. For that bulk heterojunction photovoltaics provide an appropriate approach. We selected P3HT:PC61BM and PTB7-Th:PC71BM as the low- and high-V_{oc} bulk heterojunction photovoltaic materials, respectively (Figure 5.1(a)). To generate capacitive stimuli by using the photovoltaic materials, the biointerfaces were prepared in the device forms of ITO/ZnO/P3HT:PC61BM and ITO/ZnO/PTB7-Th:PC71BM denoted as BI-1 and BI-2, respectively (Figure 5.1(a)).

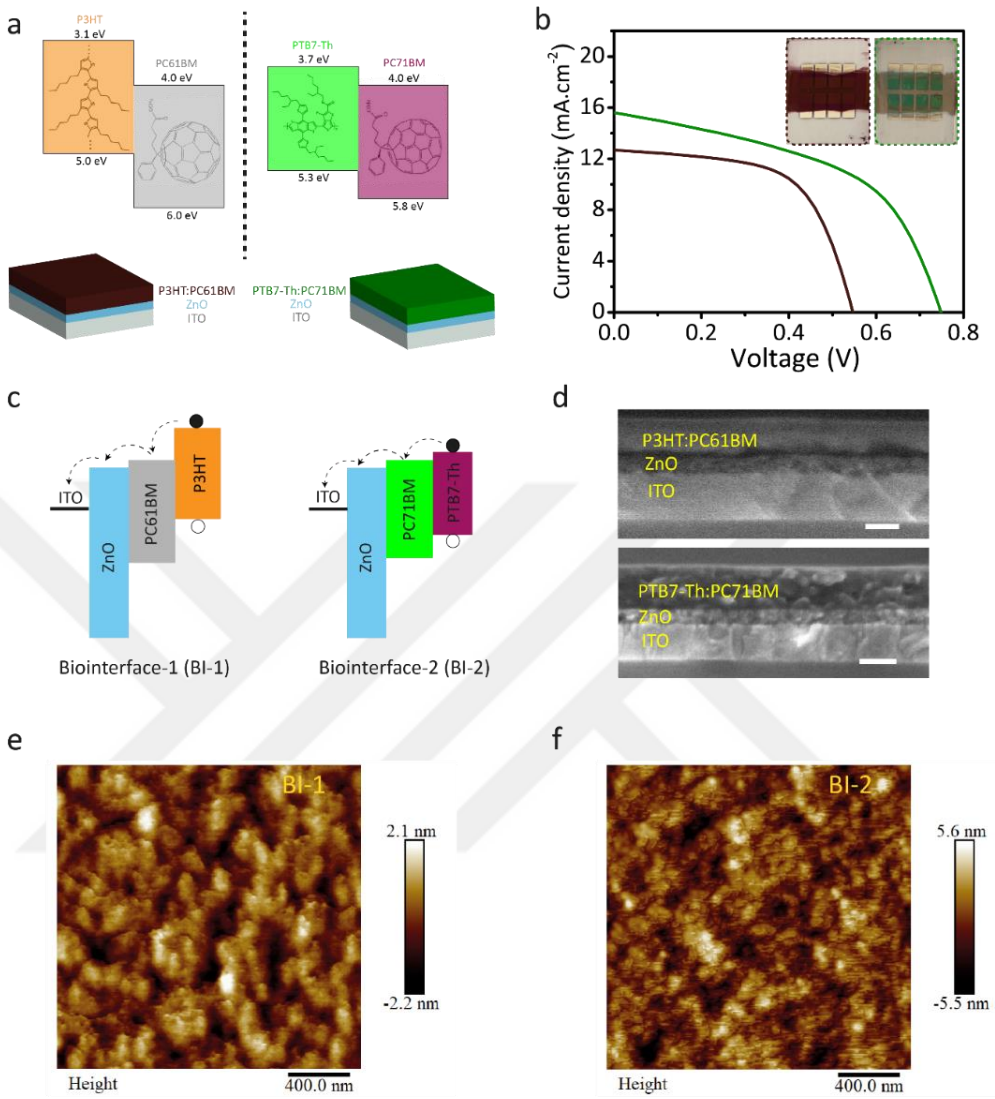

Figure 5.1: (a) Energy levels of the bulk heterojunction photovoltaic materials of P3HT:PC61BM and PTB7-Th:PC71BM. Schematic of the device structures of the biointerface 1 denoted as BI-1 (on the left) and biointerface 2 denoted as BI-2 (on the right). (b) Current and voltage characteristics of the solar cell devices. The solar cell devices have the following architectures: BI-1/MoO_x/Ag (dark red) and BI-2/MoO_x/Ag (dark green). Left and right inset show the photographs of the BI-1 and BI-2 based solar cells, respectively. (c) Energy band diagram of BI-1 and BI-2. (d) Cross-sectional SEM image of BI-1 and BI-2. Scale bar: 100 nm (e) AFM micrograph (surface height profile) of P3HT:PC61BM (BI-1) thin film and (f) PTB7-Th:PC71BM (BI-2) thin film for 2×2 μm^2 scan area.

To measure the open-circuit voltage of the biointerfaces we prepared the photovoltaic devices in the following configuration: BI-1/MoO_x/Ag and BI-2/MoO_x/Ag. We

illuminated them under one-sun AM1.5G solar radiation, and the open-circuit voltages correspond to 0.55 and 0.75 V for BI-1 and BI-2, respectively (Figure 5.1(b)). Ideally, the open-circuit voltage (V_{oc}) for the bulk heterojunction organic solar cells is defined as $V_{oc} = \left(\frac{HOMO_D - LUMO_A}{q} \right) - 0.3$ under one-sun AM1.5G solar radiation, where $HOMO_D$ is defined as the highest occupied molecular orbital (HOMO) of the donor material, $LUMO_A$ is defined as the lowest unoccupied molecular orbital (LUMO) of the acceptor material, q is the electron charge, and 0.3 is the correction factor.[87, 88] Under the ideal case, the open-circuit voltage corresponds to 0.7 V and 1.0 V for BI-1 and BI-2, respectively. Because of the factors such as mobility, lifetime, recombination of charge carriers, etc. they deviate from this ideal value within the range of 0.55-0.60 V and 0.72-0.85 V for P3HT:PC61BM and PTB7-Th:PC71BM devices, matching with BI-1 and BI-2, respectively.[76, 89-94]

After exciton dissociation by the bulk heterojunction, the free electron and hole need to be further separated for displacement current generation. For that, the bulk heterojunction composites were interfaced with ZnO and ITO layers (Figure 5.1(a)). The energy band diagrams of the structures in the Figure 5.1(c) showed that the photogenerated charge carriers can be effectively separated for capacitive charge transfer. For a proper comparison of bulk heterojunction performances, the thickness of the BI-1 and BI-2 was kept at similar levels. According to the cross-sectional scanning electron microscopy (SEM) measurements, the thickness of the BI-1 and BI-2 correspond to ~115 nm and ~119 nm, respectively, and the ZnO layer thickness was ~ 50 nm (Figure 5.1(d)). The surface morphologies of the thin films were characterized by using atomic force microscopy (Figure 5.1(e) and (f)), and we observed that the morphology of the BI-2 thin film exhibits smaller intermixed domains of donor and acceptor molecules with better homogeneity, which is beneficial for effective charge separation.

5.2 Baseline Parameters of Biointerfaces

The baseline parameters of the photocapacitor showing the ability of the effective photostimulation is the quantification of photocurrent and charge per unit area. Hence, we measured the electrochemical photoresponse of the BI-1 and BI-2 biointerfaces under the two-probe configuration that allow understanding the actual potential of the photoelectrode in terms of photocurrent and photovoltage. In this configuration (Figure 5.2 (a)), ITO electrode is used as the working electrode, and the platinum electrode that is shorted with Ag/AgCl is used as the counter electrode (~ 7 mm^2 area). During the measurement, no voltage was applied to the working electrode and current was monitored over time under light-pulse of 10 ms with 50 $mW.cm^{-2}$ intensity illuminated on the photoactive area of 1 cm^2, which is exposed to the artificial cerebrospinal fluid (aCSF) electrolyte. For comparison between the composites it is preferred to have similar photon absorption by the biointerfaces. Figure 5.2(b) indicates the absolute absorption spectra of BI-1 and BI-2, and we selected the wavelength of 470 nm for optical excitation of the biointerfaces, at which both substrates have similar absorbance levels.

Figure 5.2(c) shows the photocurrent per unit area of the biointerfaces (BI-1 and BI-2) measured between working electrode (ITO) and counter electrode (Pt) using pulsed (10 ms) 50 $mW.cm^{-2}$ intensity illumination of blue light. The observable two-spikes in the opposite directions matching with the turn-on and -off times point out a capacitive photocurrent. The peak photocurrent density was observed 168 and 511 $\mu A\ cm^{-2}$ for BI-1 and BI-2 biointerfaces, respectively. The high-Voc biointerface shows almost 3-times increase in the photocurrent density than the low-Voc biointerface. The corresponding charge densities were found 0.32 $\mu C.cm^{-2}$ and 0.46 $\mu C.cm^{-2}$ for BI-1 and BI-2 biointerfaces. The increase in the charge density is about 1.4 times, which is not at the same level with the increase of photocurrent density. It can be attributed to the faster switching speed of the BI-2 than BI-1 biointerface with respect to the pulsed illumination. Besides, a low level of direct electron or hole transfer via Faradaic reactions was observed

for BI-1 and BI-2 (Figure 5.2(c) inset). BI-1 biointerface shows a 24-µA cm^{-2} Faradaic current corresponding almost 14% of the peak photocurrent and BI-2 has negligible Faradaic component less than 3% of its peak photocurrent. Since the hole-capturing P3HT and PTB7-Th molecules had energy levels above the water windows and electrons are mainly accumulated inside the device structure, the Faradaic charge-transfer processes were limited.

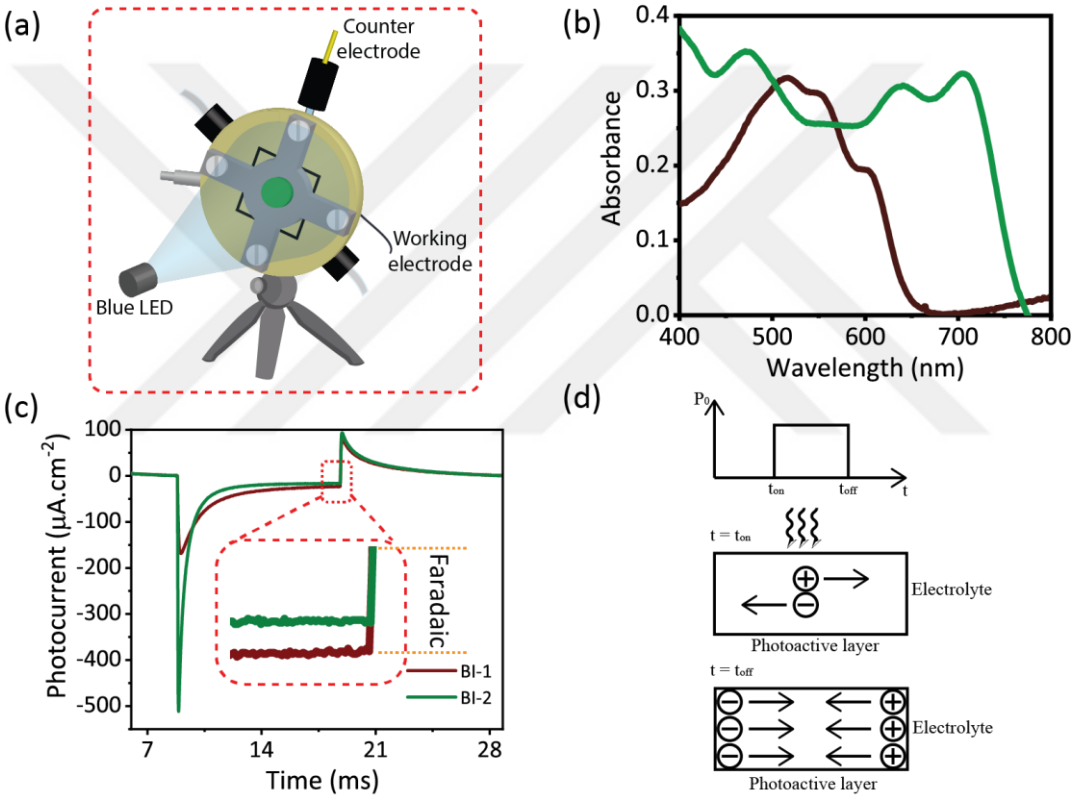

Figure 5.2: (a) Schematic illustrating the electrochemical measurement configuration of the photoelectrode in an aCSF solution. A blue LED (pulsed) is used to illuminate and activate the biointerface. (b) Absorbance spectra of BI-1 and BI-2. (c) Photocurrent density comparison of BI-1 and BI-2 biointerfaces under blue light (10 ms pulse, 470 nm, 50 mW.cm^{-2} light intensity). The inset shows the Faradaic current components of biointerfaces. The dark red color represents BI-1 and the dark green color represents BI-2 biointerface. (d) Schematic shows the movement of the photogenerated charge carriers in the biointerfaces.

The dissociation of the photogenerated excitons leads to both open-circuit voltage inside the photovoltaic device and interfacial photovoltage between the biointerface and aCSF.

To quantitatively analyze the switching properties of the biointerface we defined the rise and fall times as the time of electrode/electrolyte photovoltage (V_{ph}) reaching from 10% to 90% of its peak value and the decrease time of it from 90% to 10%, respectively. The rise time of V_{ph} for BI-2 biointerface at 50 mW.cm^{-2} is 58 µs, which is significantly faster than the 105 µs rise time of BI-1 biointerface. Since the photogenerated charges are accumulated at the respective layers via drift during the increase of V_{oc} and the internal electric field of BI-2 is higher than the BI-1 (Figure 5.2(d)), the rise time of the negative spike of photocurrent was faster.

When the light is turned off after 10 ms, a complementary behavior of photocurrent is observed. The fall time of BI-2 biointerface is recorded as 2.1 ms, which is approximately 3.5-fold faster than the BI-1 biointerface fall time of 7.3 ms. Furthermore, the fall time of BI-2 is ca. 36-fold slower than the rise time because holes and electrons are delocalized in different materials of photoactive layer and ITO/ZnO layers (like in a Type-II heterojunction), which require longer time for recombination in comparison with the rise time of interfacial voltage. The decrease in free charge carrier concentration (n_c) during recombination implies to the increase in effective lifetime (τ_n) of the remaining charge carriers recombination ($\tau_n = (\beta.n_c)^{-1}$ where β, recombination pre-factor), which further slows down the fall time of photovoltage voltage.[95] Hence, in addition to the stimuli strength, the biointerface energy levels also influence the switching properties of capacitive charge-transfer mechanism.

We performed electrochemical impedance spectroscopy (EIS) measurement under light (470 nm, 10 mW.cm^{-2}) to investigate the charge transfer processes in the biointerface-electrolyte interfaces (Figure 5.3(a) and (b)). In comparison with the BI-1, a lower impedance for BI-2 was observed (Figure 5.3(a)) between high to mid frequency region, confirming more charge accumulation for high-V_{oc} biointerface. The impedance data (Figure 5.6), extracted by fitting the experimental data with an equivalent electrical circuit, shows that the electrode-electrolyte capacitance of BI-2 (C_{dl} = 2.9 µF.cm^{-2}) is higher than BI-1 (C_{dl} = 2.6 µF.cm^{-2}), which is another factor leading higher

photocapacitive currents for BI-2. At the same time, the faster response of BI-2 is confirmed by the Bode phase peak frequency at 5.96 kHz, which is higher than the peak frequency of BI-1 at 3.72 kHz (Figure 5.3(b)). Hence, BI-2 is a better candidate for neural interface application because of high current injection levels with fast kinetics.

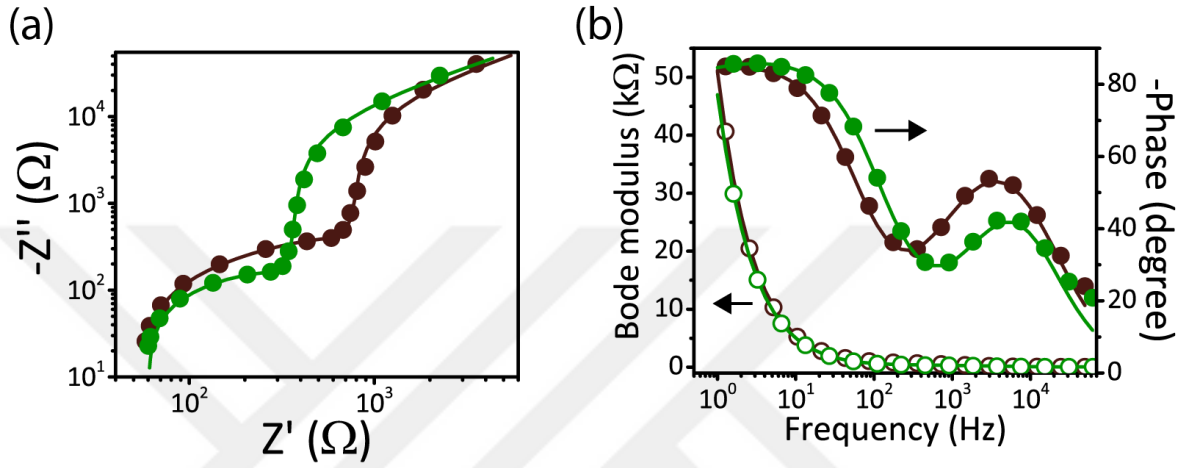

Figure 5.3: Electrochemical impedance spectroscopy of biointerfaces at zero dc bias under the illumination of 10 mW cm^{-2} at the wavelength of 470 nm: (a) Nyquist plot and (b) Bode modulus and Bode phase of the biointerfaces with fitted solid lines. Experimental data is shown by dots and the fitted data is indicated by solid lines. The dark red color represents BI-1 and the dark green color represents BI-2 biointerface.

5.3 Light intensity dependent study of high V_{oc} biointerface

We initially investigate the light intensity dependent photoresponse of the high-V_{oc} biointerface (BI-2). In the case of a wired photovoltaic device, the current density can be determined by the Equation 5.1, where R_{sh} is the shunt resistance, R_s is the series resistance, J_0 is the reverse saturation current density, q is the electronic charge, k_B is the Boltzmann constant, V is the output voltage, T is the temperature and J_{ph} is the photo-current density.[95] In these photovoltaic devices, direct electron transfer from the device

to the external circuitry is responsible for the current. However, in the capacitive photovoltaic biointerfaces since the direct electron transfer is limited due to low-level Faradaic contribution, the biointerfaces operate more closely under the open-circuit condition.

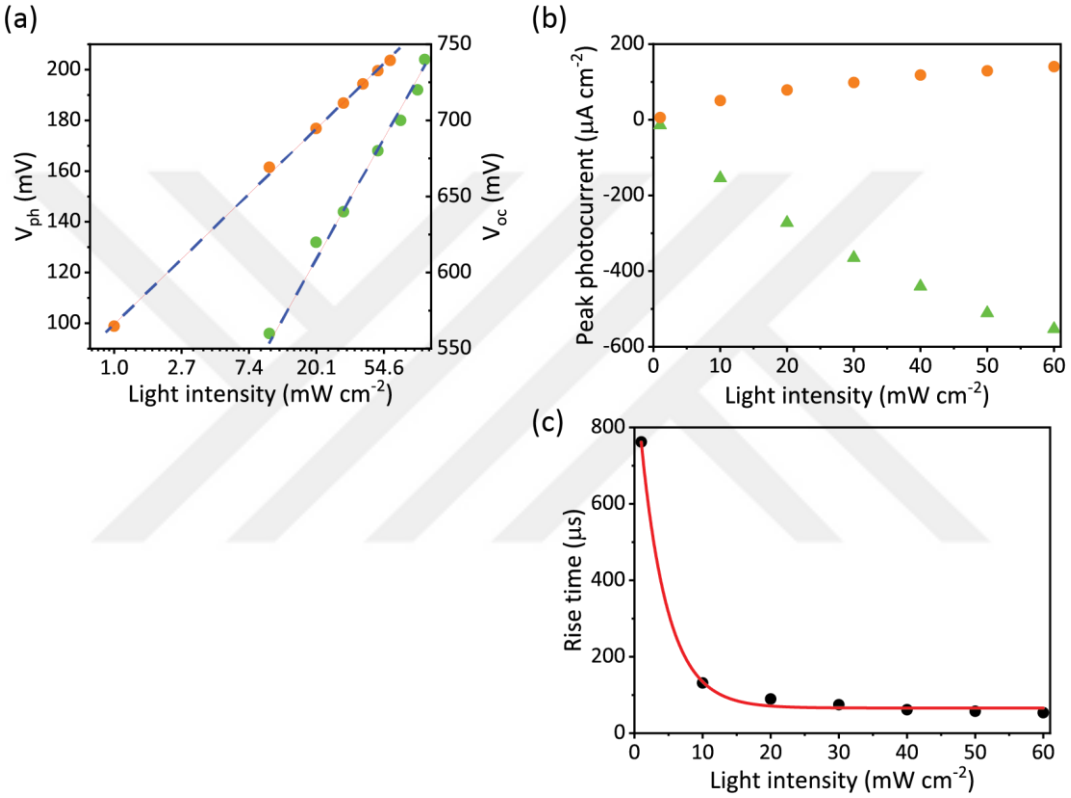

Figure 5.4: (a) Photovoltages (V_{ph}) and their corresponding open-circuit voltages (V_{oc}) of high V_{oc} biointerface under different light intensity levels. Orange dots correspond to the V_{ph} values, green dots correspond to the V_{oc} values, and the dotted lines signify the linear fitting. (b) The relationship between light intensity and peak photocurrent for both negative (orange color dots) and positive spikes (green color dots). (c) V_{ph} rise time for different light intensity levels.

Hence, we can consider that the conduction current is approximately zero and $V \approx V_{oc}$. Since this case analogically correspond to the shunt resistance much larger than the series

resistance in wired photovoltaic devices, V_{oc} can be approximated as in Equation 5.2 showing the relation between the intensity and open-circuit voltage of the biointerface.

$$J = \frac{R_{sh}}{R_{sh}+R_s}\left\{ J_0\left[\exp\left(\frac{q\left(V - JR_s\right)}{nk_BT} \right) - 1 \right] + \frac{V}{R_{sh}} \right\} - J_{ph} \tag{5.1}$$

$$V_{oc} \propto \frac{nk_BT}{q} \ln\left(C\frac{I_{ph}}{I_0} + 1 \right) \tag{5.2}$$

To explore the correlation between the open-circuit voltage of photovoltaic devices and photovoltage of the biointerface, the photovoltaic device BI-2/MoO_x/Ag was characterized under blue light with the similar intensity levels and wavelengths that are used for photocurrent measurement of biointerface. Figure 5.4(a) compares V_{ph} and V_{oc} as a function of light intensity for BI-2. The logarithmic dependence of V_{oc} and V_{ph} on incident light intensity was observed, which confirms the direct proportional relationship between V_{oc} and V_{ph} and their dependence on light intensity as in Equation 5.2.

We investigated the photoresponse of the biointerface under different illumination conditions. Figure 5.4(b) shows the variation of photocurrent for BI-2 biointerface within the light intensity range from 1 mW cm^{-2}, which is inside the retinal irradiance levels, to 60 mW.cm^{-2}. We observed 14 µA cm^{-2} at low intensity level of 1 mW cm^{-2}, and as the light intensity increases, the peak value of both negative and positive spikes of the capacitive photocurrent almost linearly increases revealing single photon-induced absorption processes.[96, 97] Moreover, we observed that while the light intensity increases, it leads to a faster switching of capacitive stimuli (Figure 5.4(c)). Under the same range of intensity, the rise time of BI-2 biointerface induces a larger variation from 762 to 54 µs. Moreover, since the dependence of the rise time is exponential with the light intensity, this also proves the direct correlation of rise time with open-circuit voltage. Hence, light-intensity defines an unconventional variable of stimulating pulses in electrode-electrolyte junctions.

5.4 Viability and Electrophysiology of Neuron Cells

Before interfacing with cells, we investigated cytotoxic effects of the biointerfaces by assessing the mitochondrial activity of SH-SY5Y cells by MTT assay.[58, 98] Cells grown on BI-2 biointerfaces exhibited comparable cell viability with respect to BI-1 and ITO controls suggest that the biointerfaces do not exhibit any toxic effect on the cells (Figure 5.7(a)). Furthermore, morphology of the cells grown on photoelectrodes was assessed by immunolabelling and fluorescence microscopy. Beta-III-tubulin primary antibody was used as neuronal marker; and DAPI staining was performed for nucleus visualization. Results suggested no morphological difference between cells grown on control substrate and cells grown on photoelectrodes (Figure 5.7(b)).

To investigate the membrane potential variation and generation of action potential, we used primary hippocampal neurons extracted from decapitated E15-E17 Wistar Albino rats. We performed single-cell patch clamping in whole-cell configuration in the current clamp mode ($I = 0$) (Figure 5.5(a)). The image (in the inset of Figure 5.5(a)) shows a patched primary hippocampal neuron during the electrophysiological recording. The primary cells are grown on the BI-2 and Figure 5.5(b) shows confocal microscopy image of the hippocampal cells. Figure 5.5(c) shows a typical *IV* characteristic of primary hippocampal cells from BI-2 biointerface, which was measured with a voltage clamp in dark condition. The cells have quasi-linear response around the resting potential. The average resting potential of the cells ($N=12$) was observed as -78 mV. Similar to the photocurrent experiments, the electrophysiology is performed in the wireless and free-standing mode, and light pulses with an intensity level of 20 mW cm^{-2} with a pulse width of 10-ms were used for the photostimulation experiments.[45, 58] When the light was illuminated on the biointerface, the photogenerated excitons are separated at the donor-acceptor interfaces and according to the energy diagram electrons were guided towards ITO electrode because of electron transport layer (ZnO), and holes were transferred

toward the respective higher hole energy molecule of PTB7-Th for BI-2 biointerface (Figure 5.2 (d)).[58]

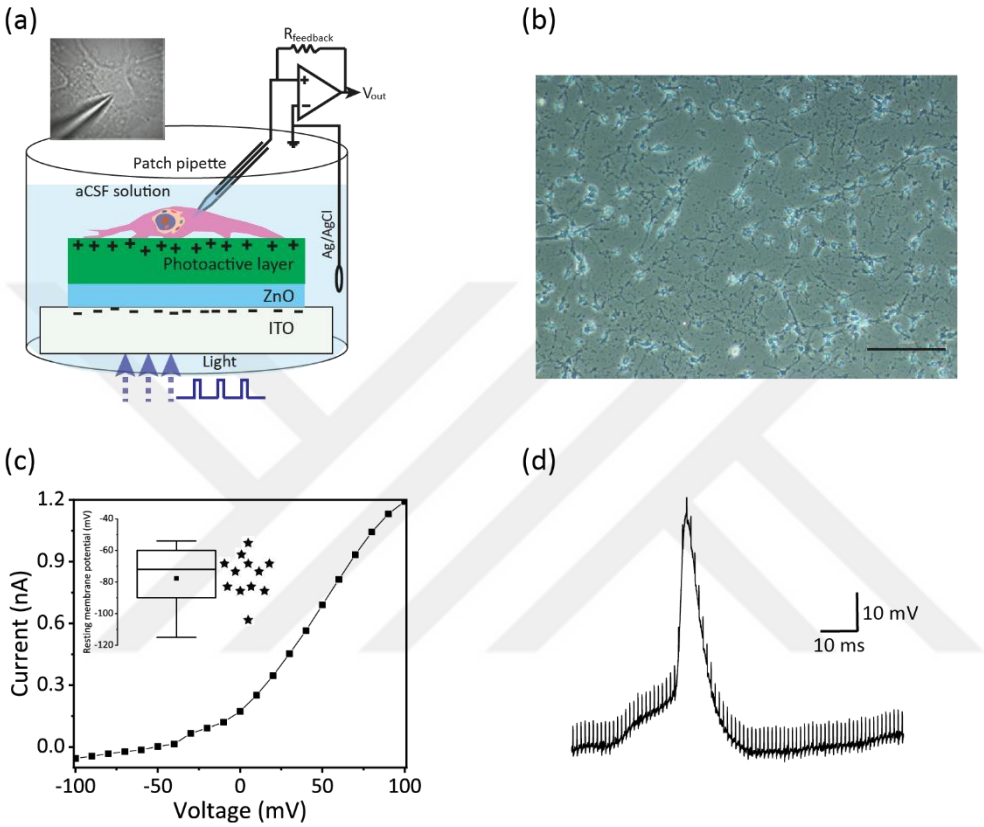

Figure 5.5: (a) Schematic of the whole-cell patch clamp recoding configuration of the biointerface in free-standing mode. The cells are grown on the biointerface and adhere on the biointerface. A LED at far field is used to illuminate and activate the biointerface. Primary hippocampal neurons were incubated for 3 days on the photoelectrode and afterward, they were patched (as shown in the inset) and recorded under the whole-cell configuration. (b) Bright-field microscopy image of the primary hippocampal cells on the BI-2 biointerface. Scale bar is 200 µm. (c) Typical IV-characteristics of the primary hippocampal neurons recorded in the voltage-clamp configuration under dark condition. Inset shows the resting membrane potential distribution for N=12 cells. (d) Light-evoked membrane potential modulation in the current-clamp configuration subjected to 1/0.1 ms light stimulation (burst waveform), which resulted in action-potential of primary neurons (N=10).

The accumulation of holes attracted the negative ions inside the electrolyte at the semiconductor-electrolyte interface. This generated a displacement current with a

direction from the semiconductor toward the electrolyte. As per our assumption, it should lead to hyperpolarization of the attached membrane and depolarization of the free membrane. Since the longer light pulse (10 ms on-time and 10 ms off-time) with square waveform has shown marginal neuromodulation at 20 $mW.cm^{-2}$, the action potential was generated when a burst waveform (1 ms on-time and 0.1 ms off-time) was applied (Figure 5.5(d)), which has been previously proposed and demonstrated by Fromherz and co-workers by using electrical stimulation.[99] This is the first demonstration of using burst light pulses for capacitive photostimulation that result in action potential generation at low light intensity levels. Since the biointerface has fast switching response (ca. 50 µs light pulses) and the capacitive currents relies on the time-dependent variation of the photovoltage change, it is one of the reasons of photostimulation at low light intensities. The stimulation is mainly triggered due to the repetitive activation of sodium channels and a summation of small inward currents pulses. Some of the visual attributes can only be perceived at threshold for the specific light pulses (in sub-µs region) and train frequency.[75, 100, 101] Hence, the high-Voc biointerface can satisfy these crucial aspects as well.

To avoid any damage on the electrode due to corrosion or on the cell due to Faradaic reactions, the stimuli must be as weak as possible. Hence, optical excitation at low light intensity levels with burst waveforms allows for a safe and efficient neuromodulation scheme. During optical excitation, photothermal effects may also contribute to the stimulation of neurons. It can be induced because of phase transition in the phospholipid ordering, change in membrane conductance and rearrangement of the ions.[84, 85] To explore thermal effects, we calculated the heat generated at the biointerface surface due to 20 $mW.cm^{-2}$ optical excitation of blue light. We found that the increase in temperature is merely 0.001 °C (see Section 5.5.1), which is insufficient for such a photothermal stimulation of the cells. Moreover, the level of intensities that we use in this study is comparatively much lower than the reports studying the thermal activation of neurons.[36]

5.5 Supporting Information

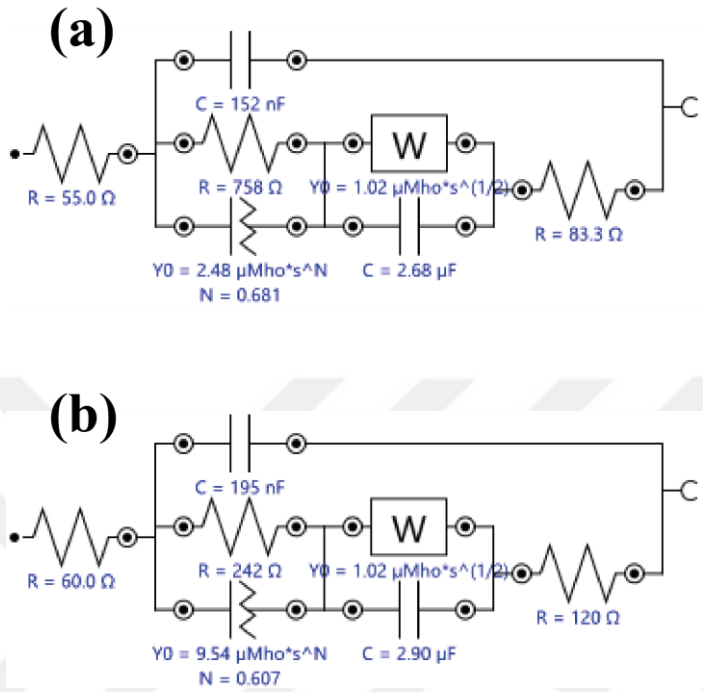

Figure 5.6: The equivalent circuit model for fitting the Nyquist plot of biointerfaces in 3-electrode configuration. (a) Equivalent circuit with physical parameters of the BI-1 biointerface. (b) Equivalent circuit with physical parameters of the BI-2 biointerface.

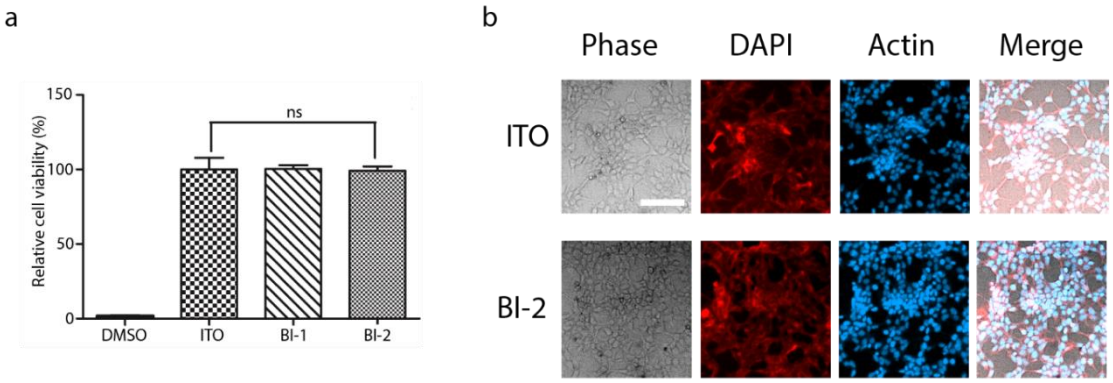

Figure 5.7: Cytotoxicity assessment and immunofluorescence microscopy. (a) The effect of photoelectrodes on the metabolic activity of SH-SY5Y cells were assessed by MTT assay. DMSO samples corresponds to the cytotoxic control samples that are incubated with 10% DMSO. ITO was used positive

*control and % cell viability was calculated relative to ITO controls. Experiment was repeated for three times (n=3) with at least three technical replicates. Results are presented in a column graph plotting the mean with standard error of the mean. Unpaired two-tailed t-test was performed to determine level of significance; *p < 0.05 was considered as statistically significant, and nonsignificant differences are presented as "ns". (b) Morphology of the cells grown on photoelectrodes were visualized by fluorescence microscopy after DAPI staining and anti-beta III tubulin immunolabelling (scale bar = 100 μm).*

5.5.1 Thermal Effect at Neuron Surface due to Light Illumination

Here we determine the maximum temperature change that can be induced by the biointerface.

For water;

$$d_q(rev, p) = mC_p dT \tag{5.3}$$

Where, d_q is related to light energy, C_p is the molar heat capacity of water, m is the molar amount of water.

Temperature change of dT can be calculated from the equation (5.3).

We use the integral form of the equation and apply experimental parameters as follows

$$\int_0^q dq(rev, p) = mC_p \int_{295K}^{T} dT \tag{5.4}$$

Considering water heat capacity as C_p=75.291 $JK^{-1}mol^{-1}$:

$$q = mC_p \Delta T \tag{5.5}$$

We can calculate the thermal energy (q) because of light illumination of 10 $mW.cm^{-2}$ (if all the light energy is converted to heat):

$$q = I \times t = 10ms \times 10mW = 1 \times 10^{-4} J \tag{5.6}$$

From equations (5.5) and (5.6) we obtain the temperature change:

$$2\times10^{-4}\,J = (0.0332g/18g/mol)\times 75.291JK^{-1}mol^{-1}\Delta T \quad (5.7)$$

$$\Delta T = 0.0014\,^{0}C$$

The light induced temperature rise should be below 1^{o}C (physiological range) as per ocular safety regulation. Therefore, the thermal change of 3-order less than the physiological range is not responsible for the photostimulation of the cell

Chapter 6: Bidirectional Optical Neuromodulation Using Capacitive Charge-Transfer

(Reprinted (adapted) with permission from **Melikov, R.,** Srivastava, S. B., Karatum, O., Dogru-Yuksel, I. B., Dikbas, U. M., Kavakli, I. H., & Nizamoglu, S. (2020). Bidirectional optical neuromodulation using capacitive charge-transfer. *Biomedical Optics Express*, *11*(11), 6068-6077. Copyright 2020 The American Physical Society (APS).)[102]

Here, we show that utilization of photovoltaic biointerfaces combined with light waveform shaping can generate safe capacitive currents for bidirectional modulation of neurons. The differential photoresponse of the biointerface due to double layer capacitance facilitates the direction control of capacitive currents depending on the slope of light intensity. Moreover, the strength of capacitive currents is controlled by changing the rise and fall time slope of light intensity. This approach allows for high-level control of the hyperpolarization and depolarization of membrane potential at single-cell level. Our results pave the way toward advanced bioelectronic functionalities for wireless and safe control of neural activity.

6.1 Biointerface characterization

We fabricated a capacitive charge-injecting biointerface developed by Srivastava et. al.[46], which is comprised of ITO on top of glass substrate as the back electrode, ZnO as the electron transport layer, and P3HT:PC61BM blend thin film as the photoactive layer (Figure 6.1 (a)).The cross-sectional SEM image shows that the thickness of the

photoactive layer is □ 100 nm and the thickness of the ZnO layer is □ 50 nm (Figure 6.1 (b)). The energy band alignment (Figure 6.1(c)) reveals that the electron transport is favorable towards ZnO and hole transport towards P3HT. The absorption spectra of the photocapacitor (Figure 6.1 (d)) advantageously covers almost the whole visible range that originate by the collective absorption of the bulk heterojunction composites from violet to red spectral window and ZnO layer in the ultra-violet region.

After the incoming light-radiation in the visible range is absorbed by the photoactive blend, the photogenerated charge carriers dissociate due to the band alignment. Electrons are drifted toward ITO and holes are localized in the P3HT to induce a displacement current. Here the integration of the intermediate layer of ZnO between ITO and the photoactive layer decreases the strength of the Faradaic portion of the photocurrent [46]. Moreover, ZnO thin film acts as a hole blocking layer, which reduces electron-hole recombination and thereby, it enhances the output capacitive photocurrent. Since LUMO energy of P3HT is above water oxidation energy, Faradaic current due to hole transfer into the electrolyte is significantly suppressed. Hence, the hole accumulation in the biointerface close to the electrolyte can generate a capacitive photocurrent.

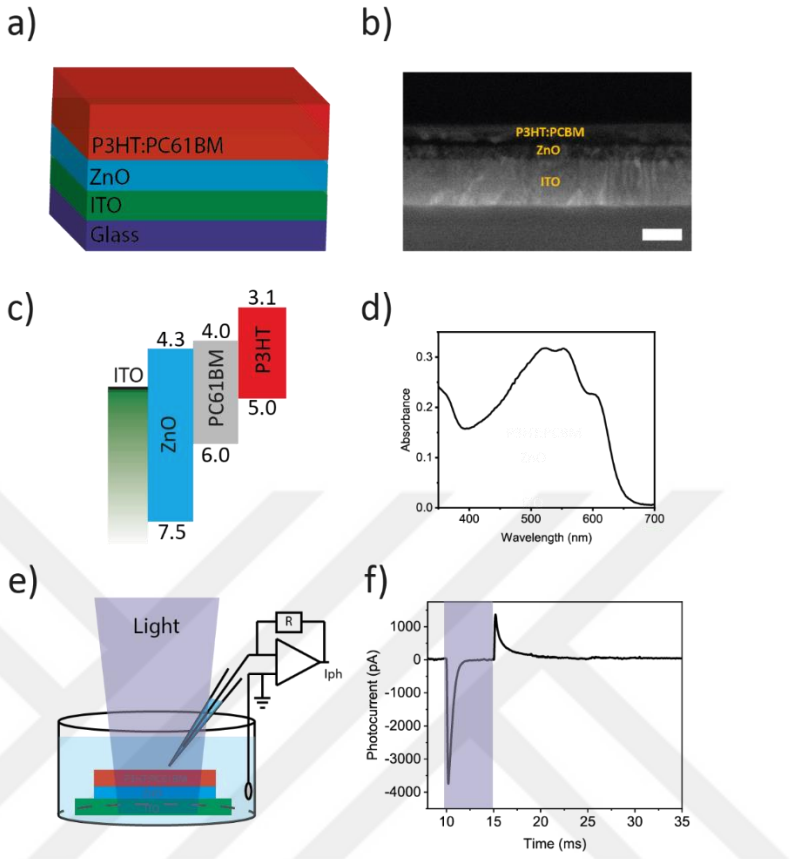

Figure 6.1: (a) Schematic of device structure of the photocapacitor (ITO/ZnO/P3HT:PC61BM). (b) Cross-sectional SEM image of photocapacitor. (c) Energy band diagram of the photocapacitor. (d) Ultraviolet-to-visible (UV-Vis) absorbance spectrum of ZnO/P3HT:PC61BM thin film. (e) Schematic of the photocurrent measurement set-up. The patch pipette is kept close to the surface and the current is measured with a voltage-clamp mode under free-standing configuration. (f) Photocurrent under 5 ms pulsed illumination.

6.2 Biointerface photoresponse

The photocapacitor is probed for the photocurrent response inside the aCSF (artificial cerebrospinal fluid) solution using patch-clamp system (HEKA, EPC800) in voltage-clamp mode with 6 MΩ patch pipette tips in free-standing condition (Figure 6.1(e)). We built an optomechanical setup that allowed light illumination from the top side on the biointerface surface impinging initially on the photoactive layer (Figure 6.1 (e)). First,

we characterized the photocapacitor with 5-ms square-wave blue light illumination at the peak intensity level of 150 mW cm^{-2} and found the capacitive photocurrent with asymmetric negative spike of 3.86 nA and positive spike of 1.35 nA, respectively (Figure 6.1 (f)). Since the holes mainly attract negative ions and repulse the positive ions, the light rise-time induces a negative capacitive transient current that corresponds to a direction from electrode to electrolyte. In contrast, while the light is turned off, since the hole accumulation and potential decreases due to recombination of photogenerated charge carriers, a positive current spike is observed. Rand et. al. [43] reported 17 mV transmembrane potential change by a photocapacitor consisting of sequentially deposited Cr/Au and H2Pc (p-type) and PTCDI (n-type). Abdullaeva et. al [103]. reported photocurrent levels of 100 pA and transmembrane potential change up to 100 µV by using SQIB:PCBM photocapacitor. Hence, the photocurrents and transmembrane potential changes reported in this study are at comparable levels.

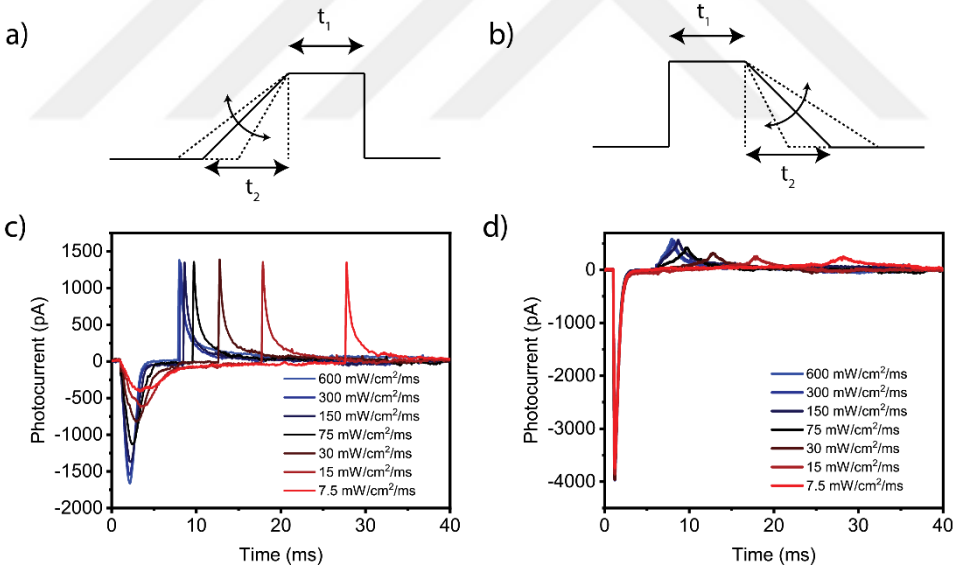

Figure. 6.2: Photocurrents generated by the photocapacitors under free-standing mode. (a) Pulse waveforms modulating the negative capacitive transient part of the photocurrent. (b) Pulse waveform modulating the positive capacitive transient part of the photocurrent. (c) Modulation of negative capacitive transients under different intensity slopes. (d) Modulation of positive capacitive transients under different intensity slopes.

In order to study the controlling behavior of the shape of light pulse waveform on capacitive photocurrents, we varied input light waveforms from square to asymmetric trapezoidal shapes.

For that we changed the illumination rise time (t_2) in Figure 6.2(a) from 250 µs to 20 ms while keeping t_1 (t_1= 5 ms) fixed at the peak light intensity of 150 mW cm^{-2}. Under these conditions, the negative peak decreased from 1720 pA to 410 pA while the slope changed from 600 mW cm^{-2} ms^{-1} to 7.5 mW cm^{-2} ms^{-1}, respectively (Figure 6.2 (c)). The photocurrent during the termination of light was relatively constant around 1.35 nA.

Similarly to analyze the effect of illumination fall time on the capacitive photocurrent, trapezoidal light pulse was used to illuminate the biointerface having 5-ms constant illumination of 150 mW cm^{-2} (t_1= 5 ms) while the fall time of t_2 was varied from 250 µs to 20 ms in Figure 6.2(b) that corresponds to the illumination slopes ranging from 600 mW cm^{-2} ms^{-1} to 7.5 mW cm^{-2} ms^{-1}. The negative peak of the measured photocurrent remained relatively constant at the level of 3.86 nA, and the positive peak decreased from 572 pA to 244 pA for the slopes ranging from 600 mW cm^{-2} ms^{-1} to 7.5 mW cm^{-2} ms^{-1} fall time, respectively (Figure 6.2(b), (d)).

To analyze the photocurrent trends, we mathematically fitted the negative and positive current peaks with R^2=98.6 % and 99.5 %, respectively (Figure 6.3(a) and (b)). Maximum negative and positive capacitive transient peaks are 3860 pA and 1350 pA that are generated by square response of LED driver (Figure 6.1 (f)). Here the slope of the square wave is limited by the illumination system. According to the fits of equations 1 and 2, the maximum rise and fall time limited by the illumination system were calculated as 101.7 ns and 102.1 ns showing the square-wave response, which correspond to the slopes of 1430 W cm^{-2} ms^{-1} and 1437 W cm^{-2} ms^{-1}. Moreover, using fitted equations 6.1 and 6.2, we can also predict light intensity rate to obtain desired negative and positive capacitive transient peaks. For example, to obtain negative capacitive transient current peak of 38.6 pA (1% of the maximum negative capacitive transient current peak of the square-wave photoresponse) the light intensity rate should be 1.0 mW cm^{-2} ms^{-1}, which corresponds

to t_2 of 115.4 ms. Similarly, to obtain positive capacitive transient current peak of 13.5 pA (1% of the maximum positive capacitive transient current peak of the square-wave photoresponse) the light intensity rate should be 1.3 mW cm^{-2} ms^{-1}, which corresponds to t_2 of 144.2 ms. While the negative and positive peaks were varied, the amount of charge was constant around 1.2 pC (Figure 6.3(c) and (d)).

$$y(pA) = -47.13 + 618.49 \ln(x(\frac{mW}{cm^2 ms})) \quad (6.1)$$

$$y(pA) = -1.00 + 218.57 \ln(x(\frac{mW}{cm^2 ms})) \quad (6.2)$$

While linear rising or falling voltage ramps generate constant capacitive currents in electrical stimulation, the case for light-evoked optoelectronic biointerfaces is different. When the photoelectrode is interfaced with the electrophysiological media in the wireless mode, it operates more closely under the open-circuit condition like a solar cell. Hence, we can consider that the conduction current is approximately zero and $V \approx V_{oc}$. Since this case analogically corresponds to the shunt resistance much larger than the series resistance in wired photovoltaic devices, V_{oc} can be approximated as in equation 6.3, which shows a logarithmic relation with the light intensity (P_{opt}) [104]. Since the capacitive current is proportional with the derivative of the voltage (i.e., photovoltage or open-circuit voltage) (equation 6.4 and 6.5), the capacitive current is proportional with the first derivative of logarithm of applied light intensity.

$$V_{oc} \propto \frac{nk_BT}{q} ln(P_{opt}) \quad (6.3)$$

$$I_{cap} \propto C \frac{d}{dt}(V) \quad (6.4)$$

$$I_{cap} \propto \frac{d}{dt}(V_{ph}) \propto \frac{d}{dt}(V_{oc}) \propto \frac{d}{dt}(\ln(P_{opt})) \quad (6.5)$$

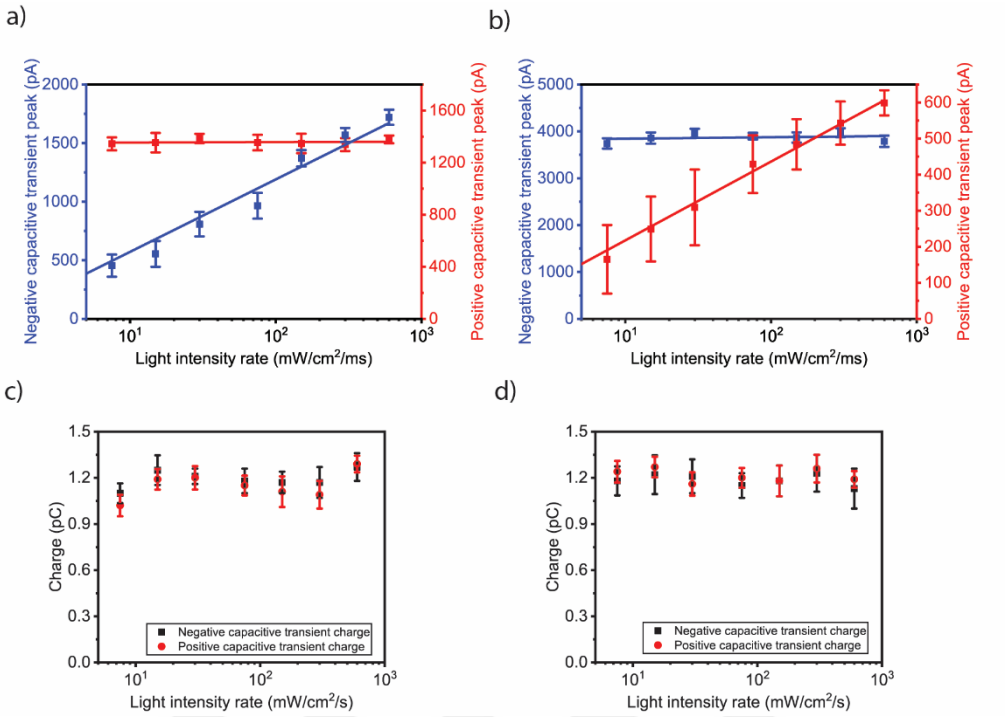

Figure 6.3: (a) Negative capacitive transient peaks (blue squares) under different light intensity slopes. Since the illumination fall time are kept constant, the positive capacitive peaks (red squares) remained at similar level. Blue and red line is the fit with R^2 as 99.4 % and 99.5 %, respectively. (b) Positive capacitive transient peaks (blue squares) under different light intensity slopes. Since the illumination fall time are kept constant, the negative capacitive peaks (red squares) remained at similar level. Blue and red line is the fit with R^2 as 99.8 % and 98.6 %, respectively. (c)-(d) Negative and positive transient charges under different light intensity slopes. (N=3 and error bars show the relative standard deviation.)

6.3 Photostimulation of neurons

To investigate the electrophysiological cellular photoresponse, we performed the patch clamping of SHSY-5Y cells seeded on the biointerface in whole-cell configuration (Figure 6.4(a)). For the cell growth on the biointerface we used the cell culture methodology as in reference [46]. The I-V characteristics of SHSY-5Y cells grown on photocapacitor under dark condition was performed in voltage clamp mode, which shows that the SHSY-5Y cells exhibit typical resting membrane potential in the range of -20 to -50 mV (Figure 6.4b). The SHSY-5Y cells exhibits quasi-linear response around the resting membrane potential. Under pulsed illumination we see depolarization followed

by hyperpolarization of the membrane potential with photocapacitor having first negative transient current peak followed by positive transient current peak. Fromherz and co-workers demonstrated in their analysis that depolarization occurring at junction membrane results hyperpolarization at free membrane (or vice versa) [21]. Since the junction membrane is attached to photoelectrode, we observe first depolarization then hyperpolarization at the free-membrane. Moreover, the biointerface does not induce any toxicity on cells in-vitro[46].

The change in membrane potentials under light modulation is shown in Figure 6.4(c) and 5.4(d). When the biointerface was illuminated by a trapezoidal pulse that has a rise time (t_2) ranging from 250 µs to 20 ms corresponding to the rising slope from 600 mW cm^{-2} ms^{-1} to 7.5 mW $cm^{-2}ms^{-1}$, the depolarization of the membrane potential peak decreased from 11.9 mV to 3.1 mV under, respectively (Figure 6.4 (e)). The depolarization peak of the membrane varied logarithmically under variation of the rise time slope with R^2 = 98.6 % fit (Figure 6.4e) (Equation 6.6). At the same time, hyperpolarization membrane potential remained constant as 5.6 mV due to the keeping the fall time fixed. Furthermore, for the trapezoidal pulse that has variation in fall time from 600 mW cm^{-2} ms^{-1} to 7.5 mW cm^{-2} ms^{-1} and constant rise time, the depolarization of membrane potential remained relatively constant as 27 mV and hyperpolarization of membrane potential decreased from 3.4 mV to 1.2 mV, respectively (Figure 6.4(f)). The hyperpolarization peak of the membrane potential varied logarithmically under variation of the fall time slope with R^2 of 99.5 % fit (see fig 6.4f) (see Equation 6.7). Under variation of the fall time slope, depolarization peak of the membrane remained constant.

$$y(mV) = -1.34 + 4.89 \ln\left(x\left(\frac{mW}{cm^2 ms}\right)\right) \quad (6.6)$$

$$y(mV) = 0.36 + 1.00 \ln\left(x\left(\frac{mW}{cm^2 ms}\right)\right) \quad (6.7)$$

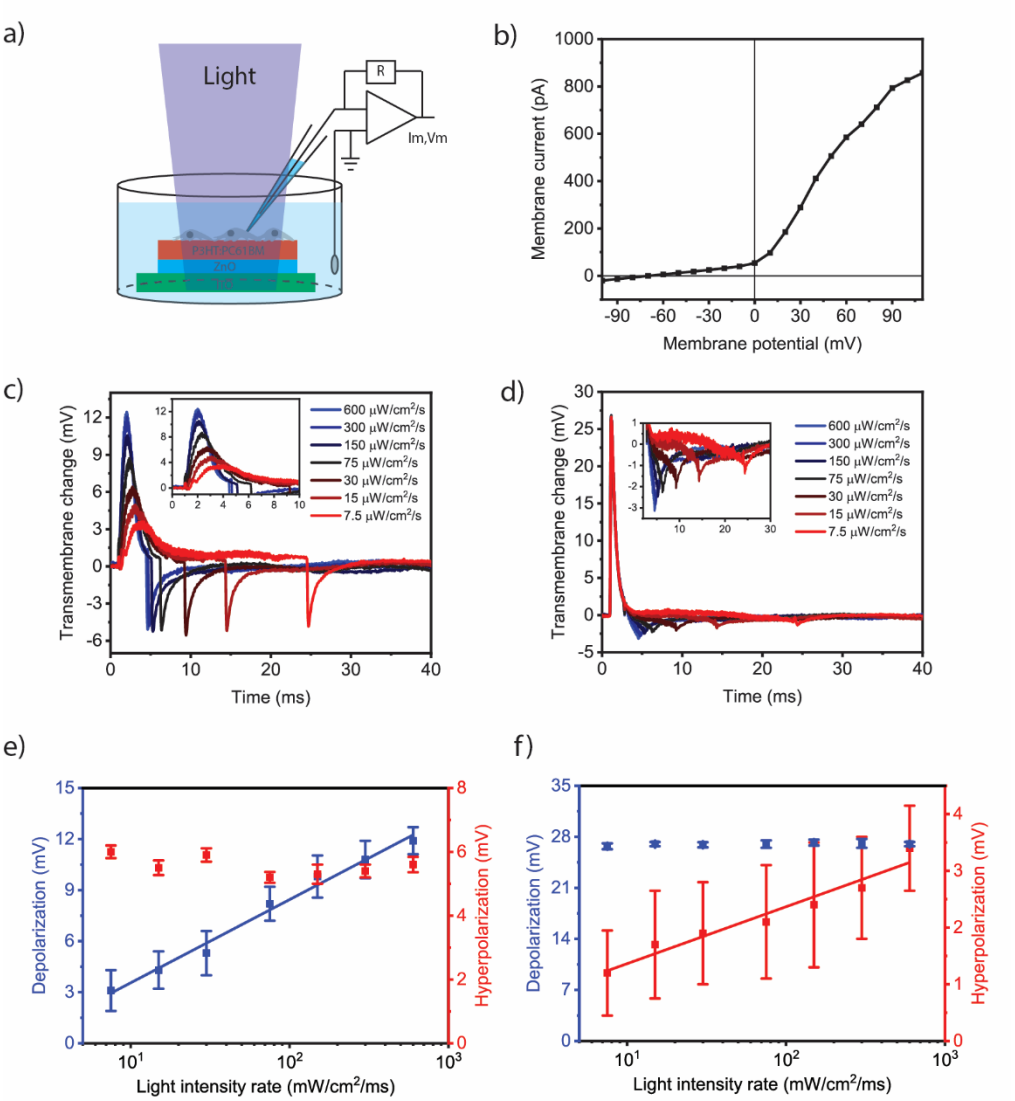

Figure 6.4: (a) Schematic of the whole-cell patch clamp recording configuration. The cells are grown on the photocapacitor and adhere on the surface. Collimated LED is used to illuminate and activate the photocapacitor. (b) Current-voltage characteristics of a typical SHSY-5Y cell on the photocapacitor. (c) Transmembrane potential change vs time of the SHSY-5Y cells on the photocapacitor with different levels of negative capacitive transient modulation. (d) Transmembrane potential change vs time of the SHSY-5Y cells on the photocapacitor with different levels of positive capacitive transient modulation. (e) Depolarization and hyperpolarization peak under different levels of negative capacitive transient modulation. Blue line is the fit with an R^2 of 99.4%. (f) Depolarization and hyperpolarization peak under different levels of positive capacitive transient modulation. Blue line is the fit with an R^2 of 97.4. (N=3 and error bars show the relative standard deviation.)

Chapter 7: Plasmon-Coupled Photocapacitor Neuromodulators

(Reprinted (adapted) with permission from **Melikov, R**., Srivastava, S.B., Karatum, O., Dogru, I.B., Jalali, H.B., Sadeghi, S., Dikbas, U.M., Ulgut, B., Kavakli, I.H. and Nizamoglu, S., 2020. Plasmon-Coupled Photocapacitor Neuromodulators. *Journal of Applied Materials and Interfaces,* 12(32), 35940–35949. Copyright 2020 The American Chemical Society (ACS).)[105]

Finally, we demonstrate that plasmonic coupling to photocapacitor biointerfaces improves safe and efficacious neuromodulating displacement charges for an average of 185% in the entire visible spectrum while maintaining the Faradaic currents below 1%. Hot-electron injection dominantly leads the enhancement of displacement current at blue spectral window, and nanoantenna effect is mainly responsible for the improvement at red-spectral region. The plasmonic photocapacitor facilitates wireless modulation of single cells at 3-orders of magnitude below the maximum retinal intensity levels corresponding to one of the most sensitive optoelectronic neural interfaces. This study introduces a new way of using plasmonics for safe and effective photostimulation of neurons and paves the way toward ultra-sensitive plasmon-assisted neurostimulation devices.

7.1 Structure of plasmonic biointerface

Capacitive charge-injection, which is a safe method for stimulation of neurons [45], is based on the electromagnetic attraction and repulsion of the ions in the biological medium due to charge movement in the stimulating electrode. For that the fabrication of plasmonic

biointerface architecture (Figure 7.1a) started with the sequential deposition of the ZnO and bulk heterojunction composite PTB7-Th:PC71BM layers on ITO (indium tin oxide) substrate. According to the cross-sectional scanning-electron microscopy (SEM) (Figure 7.1a, left), the thickness of the ZnO and PTB7-Th:PC71BM layers correspond to 52 nm and 104 nm, respectively. Afterward, gold (Au) thin film is deposited and annealed to form self-assembled nanoislands [106, 107]. The surface morphology of plasmonic biointerface confirms the formation of gold nanoislands (AuNIs) on the photoactive layer (Figure 7.1a, right) which leads to a plasmonic peak around 626 nm (Figure 7.1b inset). The broad plasmonic band stem from low annealing temperature [106] which is required to retain optical properties of organic photoactive layer. The absorption band of the plasmonic biointerface covers all the visible range, which is useful for the conversion of light within the entire visible range to bioelectrical stimuli (Figure 7.1b).

7.2 Photocurrent analysis

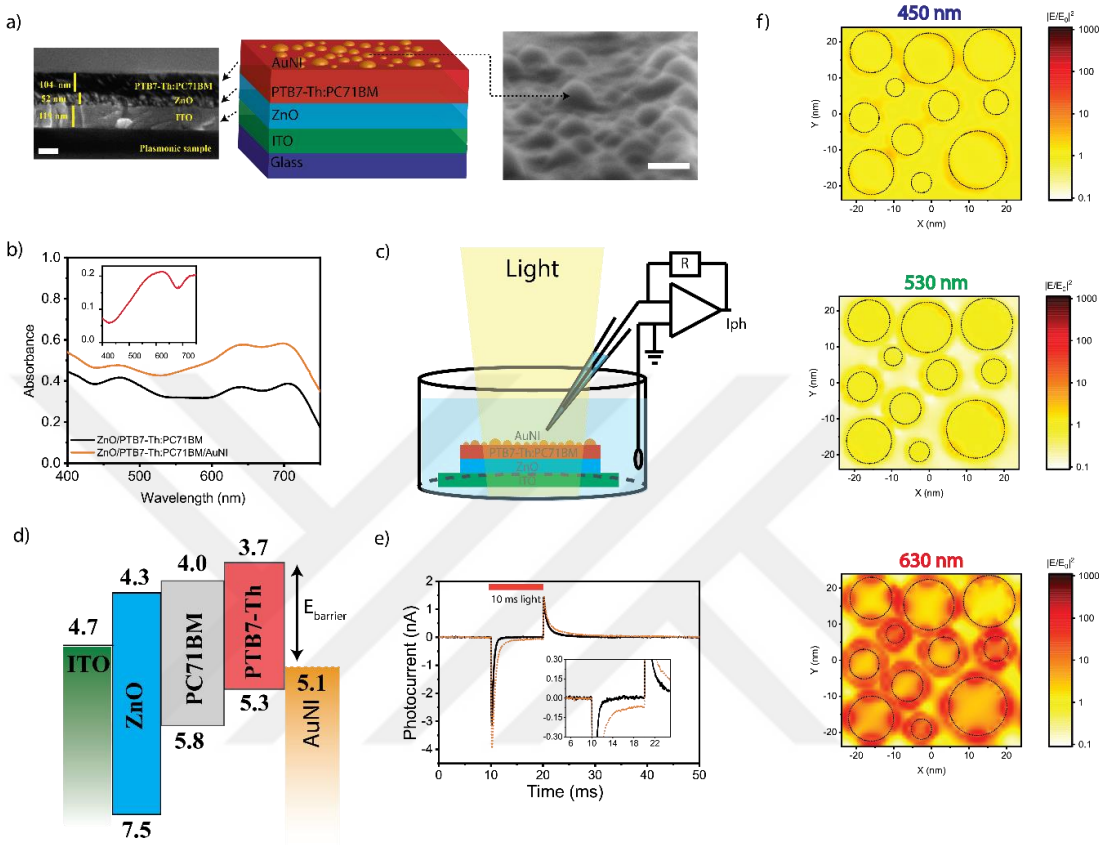

Figure 7.1: (a) (Left) Cross-sectional scanning electron microscopy (SEM) image of the plasmonic biointerface (scale bar, 100 nm). (Middle) Schematic device structure of the plasmonic (ITO/ZnO/PTB7-Th:PC71BM/AuNI) biointerface. (Right) SEM image of nanoislands on the plasmonic biointerface. (b) Absorption spectrum of ZnO/PTB7-Th:PC71BM (black line) and ZnO/PTB7-Th:PC71BM/AuNI (orange line) thin films. The inset shows absorbance of AuNI layer (red line), which is calculated by extracting it from the control biointerface without gold layer that has a smooth surface due to the absence of nanoislands (Fig. S1a and S1b). (c) Schematic of the photocurrent measurement set-up. The patch pipette is kept close to the surface and the current is measured with a voltage-clamp mode. (d) Energy band diagram of the plasmonic biointerface (with respect to vacuum). (e) Photocurrent of control (black line) and plasmonic (orange dotted line) biointerfaces illuminated under green light at 8.8±0.2 x 10^{16} photons $s^{-1}.cm^{-2}$ with 10 ms pulse-widths. The inset zooms on low photocurrent levels. The capacitive current amplitude is defined as the maximal current amplitude reached after the light onset. Faradaic current is defined as the current amplitude for 9 ms after the start of illumination (Figure A3.5). f) Lumerical FDTD simulation of AuNI of plasmonic biointerface. Top, middle, and down panels show field profile at 450, 530 and 630 nm. KEelectron = Ephoton - Ebarrier - Edeep traps, Ebarrier = 1.4 eV, Edeep trap = [0.5-0.8] eV. KEelectron at 450 nm = 2.75 – 1.4 – 0.8 = +0.55 eV, KEelectron at 530 nm = +0.14 eV and KEelectron at 630 nm = -0.23 eV. While there is hot electron injection at blue and green spectral region, at red spectral region we observe nano antenna effect.

We investigate the photocurrent response of the plasmonic biointerface in aCSF (artificial cerebrospinal fluid) solution. We use a patch-clamp system (HEKA, EPC800) in voltage clamp mode (with ~ 6 MΩ patch pipette tips) under the free-standing condition (Figure 7.1c). Since the optoelectronic processes are quantal, the biointerfaces were pumped under illumination of blue, green and red lights by keeping the photon counts at the same level (Figure 7.7-7.8), which correspond to 8.8±0.2 x 10^{16} photons $s^{-1}.cm^{-2}$ with 10 ms pulse-widths. The plasmonic biointerface generates several nanoamperes of photocurrent in aCSF in the entire visible spectrum (Figure 7.9). Among different excitation wavelengths, green spectral window shows the highest photocurrent for both biointerfaces due to higher absorption strength and external quantum efficiency of the photoactive blend [108] in comparison with the blue and red excitation (Figure 7.9). Two spikes were observed at the onset and offset of light illumination. These two spikes (i.e., onset and offset peaks) show that the charge-transfer transfer mechanism is based on the capacitive charge-transfer [74].

Here the current generation mechanism is controlled by the energy band alignment of the layers in the biointerface (Figure 7.1d). Photogenerated charge carriers initially dissociate in the photoactive blend and electron transport toward ZnO layer takes place. Holes are mainly localized in the proximity of the electrolyte interface that induces a displacement current. Hence, the initial hole accumulation near electrolyte interface generates onset capacitive photocurrent from the biointerface to the electrolyte (Figure 7.1e). After the light is turned off, the decrease of the hole concentration due to recombination leads to another offset capacitive spike in the opposite direction.

We compared the light-induced current and charge generation characteristics of the biointerface with the control biointerface. For the analysis we identified Faradaic and capacitive contributions at blue, green and red spectral windows under the same photon counts (Figure 7.10 Equation 7.1-7.4). The total capacitive charge transfer to the electrolyte is improved for 185.6%, 163.2% and 207.9% at blue, green and red spectral

windows, respectively, which correspond to an average increase of 185% in the entire visible spectrum (Figure 7.2a, Table 7.1, 7.2). Furthermore, the plasmonic biointerface enhanced the peak photocurrents at the level of 34.5%, 28.0% and 25.7% for blue, green and red illumination, respectively (Figure 7.2b) (Table 7.3, 7.4). We observed that since LUMO energy of PTB7-Th is above water oxidation energy, the Faradaic current due to hole transfer to electrolyte is significantly suppressed that correspond less than 1% of the total photocurrent (Figure 7.11). The linear response of the biointerface to the light intensity indicates a single-photon-absorption induced charge carrier generation (Figure 7.2c, Figure 7.12). We also analyzed the possible contribution by the photothermal effects and since the intensity levels that the plasmonic biointerface operates several orders of magnitude lower than the heat-induced neurostimulation, we did not observe any temperature variation in the solution even under 170 $mW.cm^{-2}$ (Figure 7.13). Furthermore, we varied the pulse width between 50 µs-100 ms, and we observed that the peak capacitive currents are well maintained for the pulses longer than 200 µs, which are sufficiently short to elicit targeted electrophysiological processes. The decrease of the photocurrent amplitude below 200 µs stems from the strong overlap between the onset and offset peaks of the capacitive spikes (Figure 7.2d, Figure 7.11).

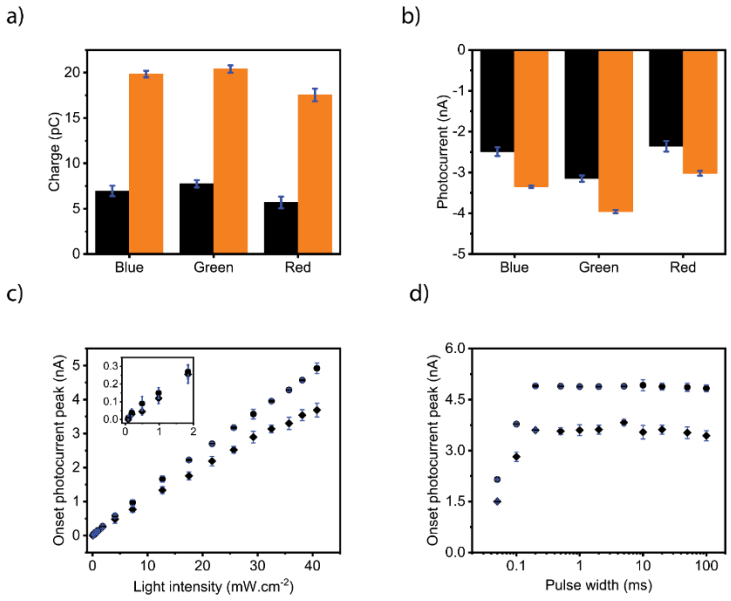

Figure 7.2: (a) Injected amount of charges and (b) current peaks of the control (black) and plasmonic biointerfaces (orange) at 8.8±0.2 x 10^{16} photons $s^{-1}.cm^{-2}$ with 10 ms pulse-widths. (c) Magnitude of peak of capacitive photocurrentcurrents of the control (rhombus dots) and plasmonic (circle dots) biointerfaces under different light intensity levels. (d) Magnitude of the peak capacitive currents generated by the control (rhombus dots) and plasmonic (circle dots) biointerfaces under different pulse widths having light intensity at 8.8±0.2 x 10^{16} photons $s^{-1}.cm^{-2}$.

7.3 Electrochemical investigation of plasmonic enhancement

We investigate the enhancement of the displacement current by the plasmonic biointerface using electrochemical impedance spectroscopy. For that we did 3-probe measurements in aCSF media using Ag/AgCl as a reference electrode, platinum as a counter electrode and biointerface as the working electrode [109]. To verify enhancement in electrophysiology setup, initially we measured the photocurrent levels and we observed a current level of 862 $\mu A.cm^{-2}$ that inject 1.2 $\mu C.cm^{-2}$ under 50 $mW.cm^{-2}$ blue LED excitation for plasmonic photoelectrode. Hence, with respect to the control group the capacitive charge-transfer and peak photocurrent was improved for 182% and 24%, respectively, which is similar to the enhancement observed by electrophysiology setup (Figure 7.3a). The physical mechanisms at the various interfaces are probed in response to a small AC perturbation of 10 mV (V_{rms}) varied over a frequency range from 1 Hz to 0.1 MHz at zero DC bias. Impedance response of the control and plasmonic biointerfaces are semicircle in the high to mid frequency region and depressed semicircle with a linear extension in the low frequency region in the complex plane (Figure 7.3 (b)-(d)). The Bode plot at high frequency is generally interpreted as the electrolyte region and the kHz frequency region corresponds to the double layer formed at the photoelectrode/electrolyte interface (Figure 7.14). Bode phase angle (56^0) is found similar for both biointerfaces under blue and green light illumination, and it is interestingly observed higher (62^0) for the plasmonic biointerface under red light illumination (Figure 7.3 (e), (f)).

To correlate with the physical mechanisms in the plasmonic biointerface we analyzed the frequency response and fitted the equivalent circuit model (χ^2=0.01-0.03) comprised of metal-insulator-metal structure (Figure 7.3g). C_g represents the geometrical capacitance of the device and R_s is assigned to the electrical resistance that present at metal electrodes and electrode/contact layer/active layer interfaces. The recombination resistance (R_{rec}) in parallel with constant phase element (CPE1) corresponds to the charge dynamics in the photoactive bulk heterojunction. The random characteristics of the blend active layer in organic bulk heterojunction can be attributed to the distribution of relaxation times and are related to the impedance as $Z = Y_0^{-1}(j\omega)^{-n}$, where Y_0 is the CPE coefficient and the ideality factor n – 0 for pure resistive and 1 for pure capacitive behavior – is the characteristic of the distribution of relaxation times [73]. The plasmonic photoelectrode/electrolyte interface is defined by the parallel combination of Warburg element (W) with double layer capacitance (C_{dl}). Using the fitted macro-electrical parameters (Table 7.5), the optoelectronic parameters of the biointerfaces such as effective lifetime (τ_n) and mobility (μ_n) of charge carriers are determined (Table 7.6).

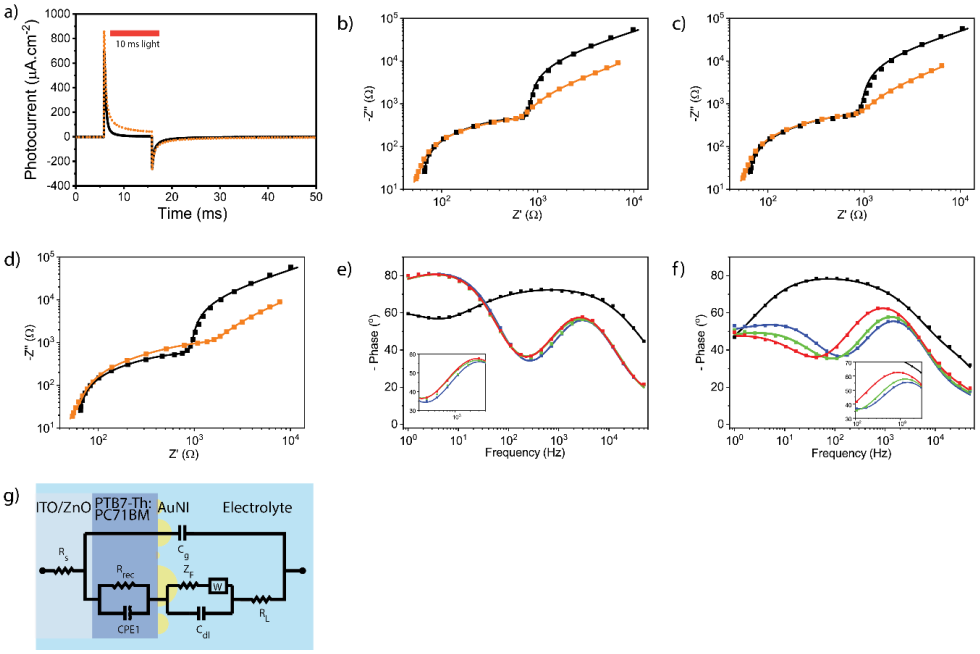

Figure 7.3: Electrochemical characterization of the control and plasmonic biointerfaces. (a) Photocurrent of control (black line) and plasmonic (orange dotted line) biointerfaces measured by two-probe electrochemical setup, where working electrode connected to ITO and counter and reference electrode is in extracellular solution. Nyquist plot of the control (black) and plasmonic biointerfaces (orange) (b) under blue, (c) green and (d) red excitation. Bode phase of (e) the control and (f) plasmonic biointerface measured by three-probe electrochemical setup. The inset zooms between 50-5000 Hz. (g) Circuit diagram fitting the Nyquist and Bode plot for both the control and plasmonic biointerfaces.

We observed that while the recombination resistance (R_{rec}) is similar both for control and plasmonic biointerfaces under blue and green light, it increases approximately 2-times (R_{rec} =1.6 kΩ) for the plasmonic biointerface under red light in comparison with the control biointerface. This leads to a rise of effective recombination lifetime and indicates a higher number of photo-activated charge generation. Since the peak plasmonic absorption by the gold nanoislands is at red-spectral range, the presence of gold nanoislands at the biointerface can increase the electron concentration by near-field enhancement of the incoming electromagnetic wave, which is observed by the corresponding recombination lifetime increase (Table 7.6).

In blue spectral region, while the recombination resistance (R_{rec} = 0.66 kΩ) and effective lifetime (τ_n = 0.3 ms) remain at similar level with the control biointerface, there is an increase in electron mobility for the blue excitation compared to the red excitation of the plasmonic biointerface. This means that electron injection becomes more probable in blue spectral range. According to the band energy diagram, the energy of blue photons can lead to the excitation of the electrons to an energy level, which is higher than the barrier between gold nanoislands and HOMO level of donor the molecules (PTB7-Th). Hence, the hot electrons with high kinetic energy have higher probability to reach the ITO/ZnO interface [110]. This shows that while at red spectral region nanoantenna effect is dominantly responsible for near-field enhancement, at blue spectral range hot carrier injection becomes the leading factor. Furthermore, the increase of the double layer capacitance at all wavelengths from 2.1 to 3.1 μF/cm^2 supports the plasmonic enhancement of capacitive photocurrent at each color.

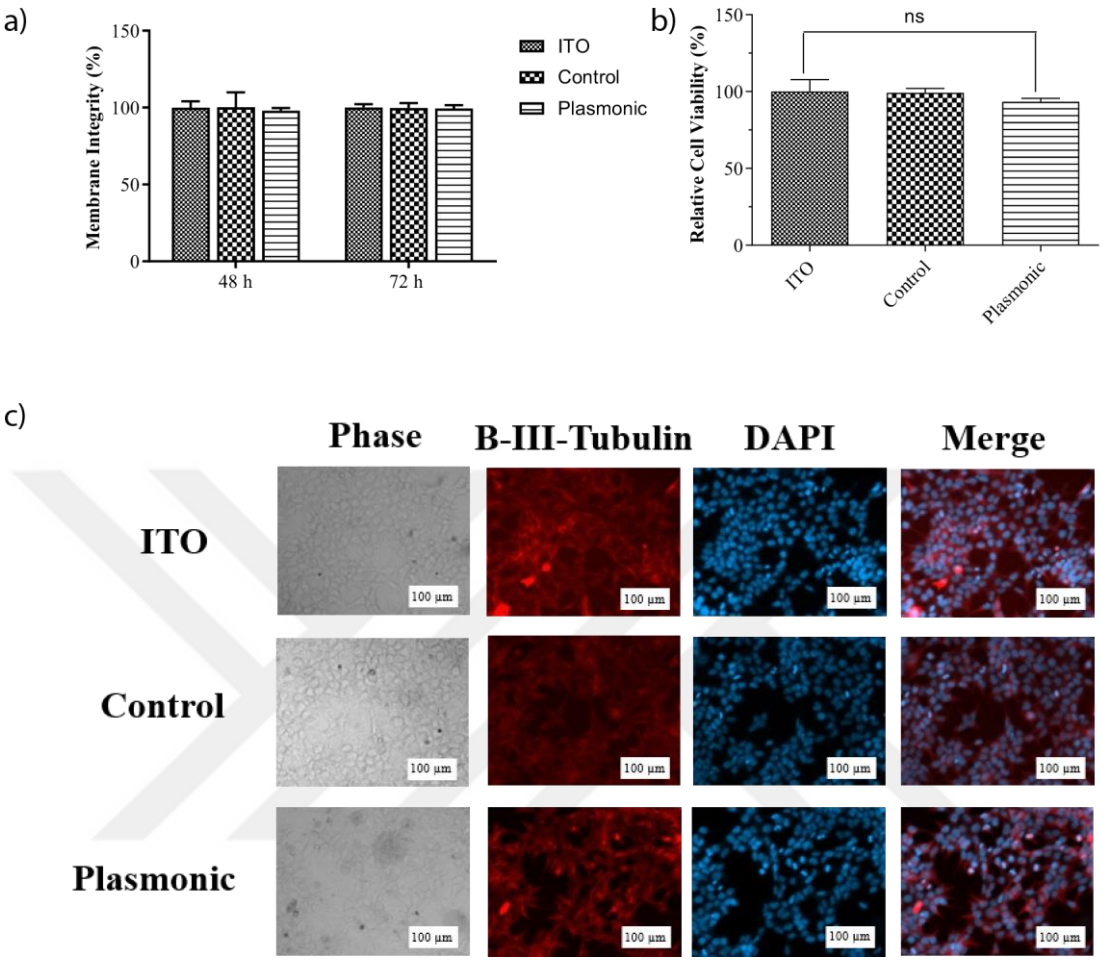

*Figure 7.4: (a) MTT assay, assessment of the effect of plasmonic biointerfaces on mitochondrial activity of SHSY-5Y cells. Cell viability on biointerfaces was presented relative to ITO control. Results are presented in a column graph plotting the mean with standard error of the mean (SEM). Experiments were performed with at least three technical replicates and repeated three times (n=3). An unpaired two-tailed t test was performed to determine the level of significance. *p < 0.05 was considered as statistically significant, nonsignificant differences are presented as 'ns'. (b) LDH leakage assay, assessment of membrane integrity of the cells grown on biointerfaces. Experiments were performed with at least three technical replicates and repeated three times (n=3). (c) Immunofluorescence imaging, effect of biointerfaces on the morphology of SHSY-5Y cells. Morphology of the cells grown on biointerfaces was visualized by fluorescence microscope after beta-III tubulin immunolabeling and DAPI staining (scale bar: 100 µm).*

7.4 Biocompatibility

To test the biological and electrophysiological activity we used SHSY-5Y cells. These kinds of non-spiking cells such as N2A, oocytes are already used to prove the neuromodulation ability [111, 112]. Initially, we tested the mitochondrial activity with 3-(4,5-dimethylthiazol-2-yl)-2,5-diphenyltetrazolium bromide (MTT) and lactate dehydrogenase (LDH) assays to determine the toxicity of the plasmonic biointerfaces on SHSY-5Y cell line. In these assays we used ITO substrate as the control group. Plasmonic biointerfaces did not exhibit any toxicity on the cells by either assay (Figure 7.4a, 7.4b). We also evaluated the effect of plasmonic biointerfaces on cell growth by investigating morphology of the SH-SY5Y cells via fluorescence microscopy. Cells grown on the samples were fixed with 4% paraformaldehyde (PFA). Nucleus of the cells were stained with 4',6-diamidino-2-phenylindole (DAPI) and the cytoplasm was visualized by anti-beta-III tubulin immunolabeling. As can be seen in Figure 7.4c, cells grown on biointerfaces exhibited comparable morphology with the cells grown on ITO control. All these results suggested that plasmonic biointerfaces are suitable for biological experiments with SHSY-5Y cells.

7.5 Photostimulation of neurons

To investigate the membrane potential variation, we perform patch clamping in whole-cell configuration (Figure 7.5a). The I-V characteristics of SHSY-5Y cells grown on both control and plasmonic biointerfaces under dark condition shows that the SHSY-5Y cells exhibit typical resting membrane potential in the range -20 mV and -40 mV (Figure 7.5b). The SHSY-5Y cells exhibit quasi-linear response around the resting membrane potential on both biointerfaces. Under 10-ms green light (1 $mW.cm^{-2}$ - 40 $mW.cm^{-2}$) an initial depolarization of a single-cell membrane depolarization is followed by a hyperpolarization (Figure 7.5c). Since the current direction of the first capacitive peak current is from the biointerface toward the substrate in the attached membrane part, the

current leads to a depolarization in the free membrane. In contrast, the second peak of the capacitive current leads to a hyperpolarization of the free membrane (Figure 7.15). Similar membrane behavior under illumination is also observed for green and red illumination as well (Figure 7.16). Moreover, under repetitive excitation the peak membrane potential change is also stable under different illumination colors (Figure 7.17, Figure 7.5e and Table 7.8).

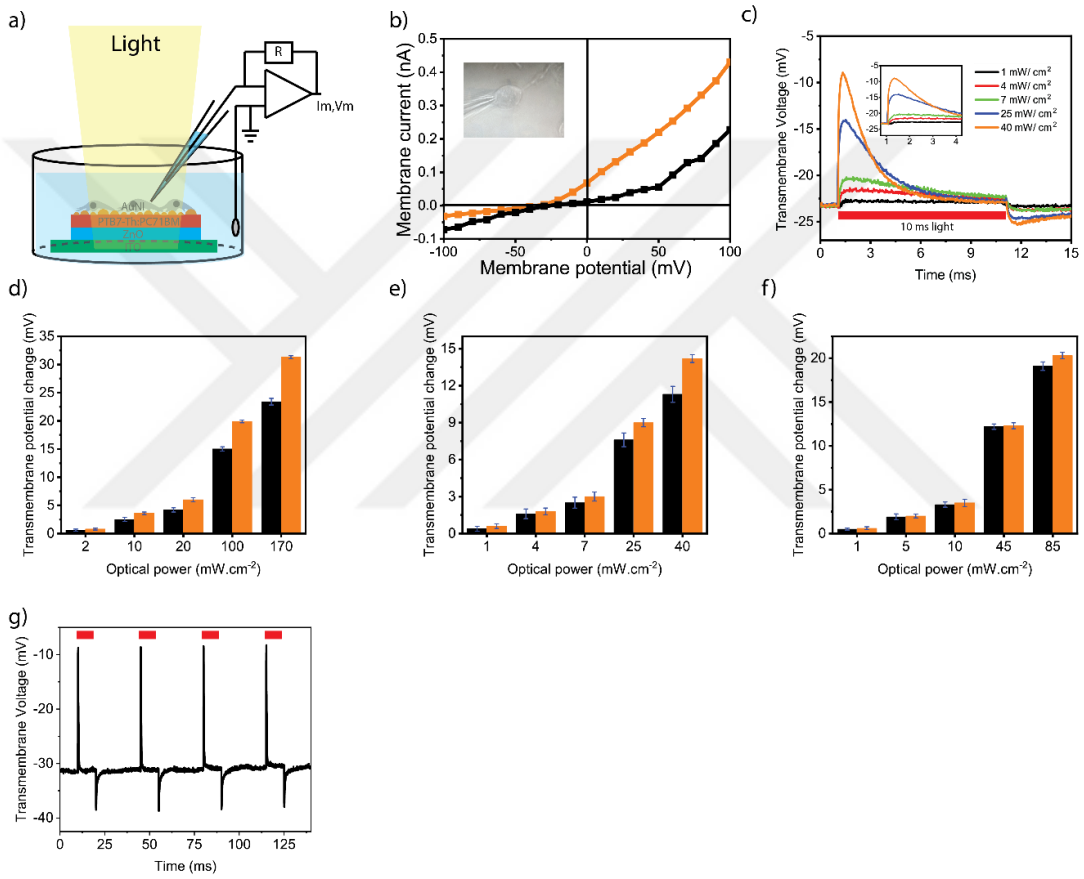

Figure 7.5 (a) Schematic of the whole-cell patch clamp recording configuration of the biointerface in wireless and free-standing mode. The cells are grown on the biointerfaces and adhere on the surface. (b) Current-voltage characteristics of a typical SHSY-5Y cell adhered on the control (black line) and plasmonic (orange line) biointerfaces. The inset shows photograph of a SHSY-5Y cell on the plasmonic biointerface patched with a glass micropipette. (c) Transmembrane potential variation of SHSY-5Y cells on the plasmonic biointerface under green light illumination with 10 ms pulse width. (d) – (f) Transmembrane potential variation of SHSY-5Y cell on the control (black) and plasmonic (control) biointerfaces under blue (d), green (e) and red (f) light illumination with 10 ms pulse width. (g) Transmembrane potential under 10-ms pulse train.

In comparison with the control biointerface, we observed a 37.3 % enhancement in the peak depolarization of the transmembrane potential of the SHSY-5Y cells for blue excitation (Figure 7.5d). While the excitation is shifted to green and red colors, we observed lower peak enhancement of 25.3 % and 7.7 %, respectively (Figure 7.5(e)-(f), Equation 7.5-7.6 and Table 7.7). This shows that the strength of the stimuli due to nano-antenna effect has a reduction in comparison with the hot electron injection. We attribute that since the wave vector orthogonality to the plane of the biointerface is important for the nano-antenna effect (Figure 7.18 and 7.19), the refractive index profile change due to the cell membrane and intracellular environment surrounding the metallic nanoislands possibly disturbs the wave vector of the biointerface [113] and decrease the enhancement in the red-spectral window.

7.6 Discussion

Hot-electron injection is the dominant electronic mechanism for the enhancement of capacitive stimulation. The photons both in the blue and red spectral windows have sufficient energy to generate hot electrons. Since the excited state energy of hot electrons under blue excitation is higher than the red excitation, the hot electron injection to the biointerface at blue pump is more probable. But the decrease in the hot-electron injection probability in the red-spectral region is compensated with the near-field enhancement of the optical energy in the bulk heterojunction (BHJ) composite.

To capture the hot electrons efficiently we formed a Schottky barrier with the PTB7-Th:PC71BM bulk heterojunction (BHJ) composite. Since the generated hot electrons with energies higher than the Schottky barrier energy see lower interfacial resistance toward the BHJ in comparison with the electrode-electrolyte interface, they can be efficiently transferred into the photoactive layer, instead donating the electron to the electrolyte for Faradaic reactions. We also observed this fact from the low magnitude of the Faradaic photocurrents. After the hot electron is injected to the optoelectronic

biointerface, the gold nanoislands are left with a hole. Since the capacitive current in the plasmonic biointerface is effectively based on the hole accumulation at the electrode-electrolyte interface, the holes remained after hot electron injection inside the gold nanoislands and the ones that moved to the PTB7-Th due to low potential barrier lead to the capacitive enhancement. Therefore, even though electron relaxation through electron–electron and electron–phonon collisions that are converted into heat energy was generally used as the main mechanism for cell stimulation [29, 43, 45, 114, 115], differently in this study both hot electron injection and near-field enhancement are used to improve the displacement currents.

The intensity levels that are applied here for cell stimulation can be safely used for all the tissue or cell types. For example, the most light-sensitive part of human body is the retina, and the design of the biointerfaces need to satisfy maximum permissible exposures for ocular safety limits allowed for ophthalmic applications. In this regard, 1 mW. cm^{-2} light sensitivity of plasmonic biointerface corresponds to more than 3 orders of magnitude smaller than ocular safety limits (see Methods section). Though the transmembrane potential variation in the free membrane seems low, the variation in the attached membrane is significantly larger [112], moreover the current levels (over 100 pA) that are observed by using similar electrophysiological measurements [116] are enough to elicit action potentials. Therefore, these plasmonic biointerfaces are potentially applicable to recover the vision due to photoreceptor loss in the retina [29]. This kind of sight loss is frequent in the clinics due to age-macular degeneration, retinitis pigmentosa, Stargardt's disease [117-119].

Gold nanoislands have high potential for biological applications due to its biocompatibility, easy fabrication, and control over optical properties. They have strong absorption from the visible to NIR region, therefore, plasmon-coupled biointerfaces can lead to a new solution for capacitive stimulation for deep-brain regions. The plasmonic absorption arises due to collective oscillation of the conduction-band electrons in the resonance peak of the absorbance spectrum, and its resonance peak of the nanometals can

be further controlled by alloying with different metals (e.g., silver) or using different shapes (e.g., cube) [120]. Hence, the combination of the plasmonics with optoelectronic biointerfaces offers a wide variety of device architectures for cell stimulation that can operate at different spectral windows for photomedicine.

7.7 Supporting Information

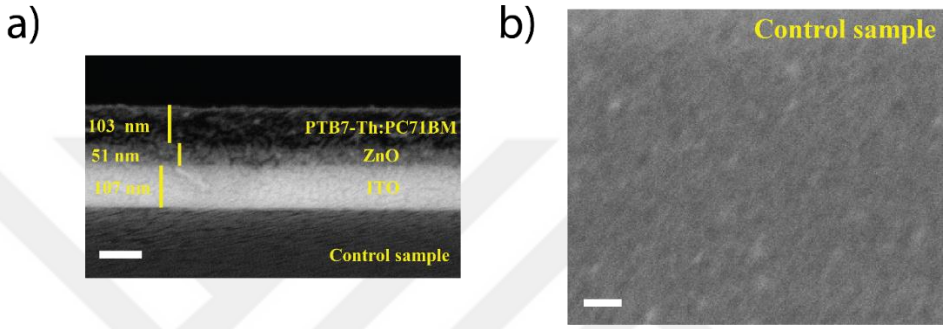

Figure 7.6: (a) Cross-sectional scanning electron microscopy image of the control biointerface (scale bar, 100 nm). (b) Scanning electron microscopy image of the control biointerface surface (scale bar, 100 nm).

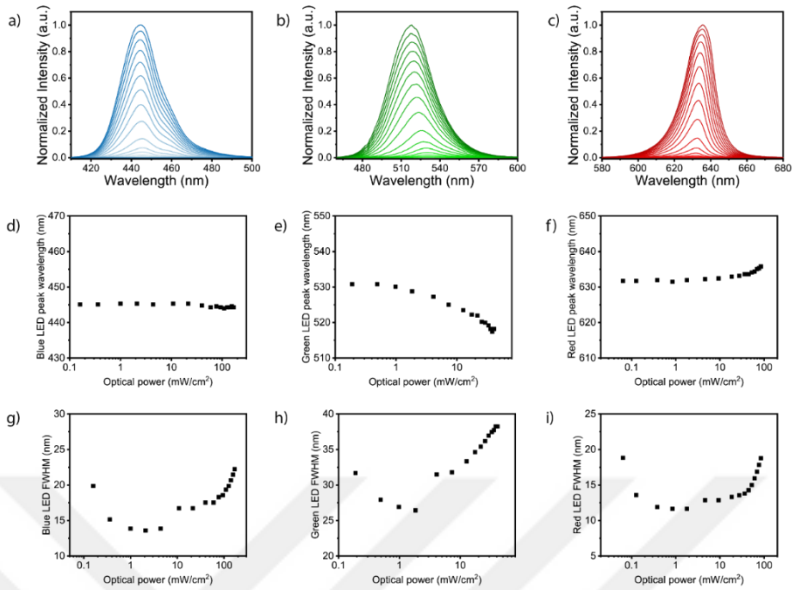

Figure 7.7: (a) – (c) Spectral intensity, (d) – (f) peak wavelength and (g) – (i) FWHM properties of blue (a,d,g), green (b,e,h) and red (c,f,i) illumination sources at different optical powers.

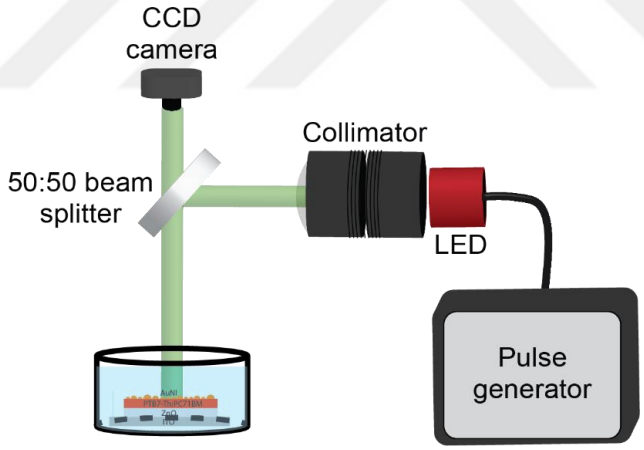

Figure 7.8: Optical set-up during photocurrent and electrophysiology experiments.

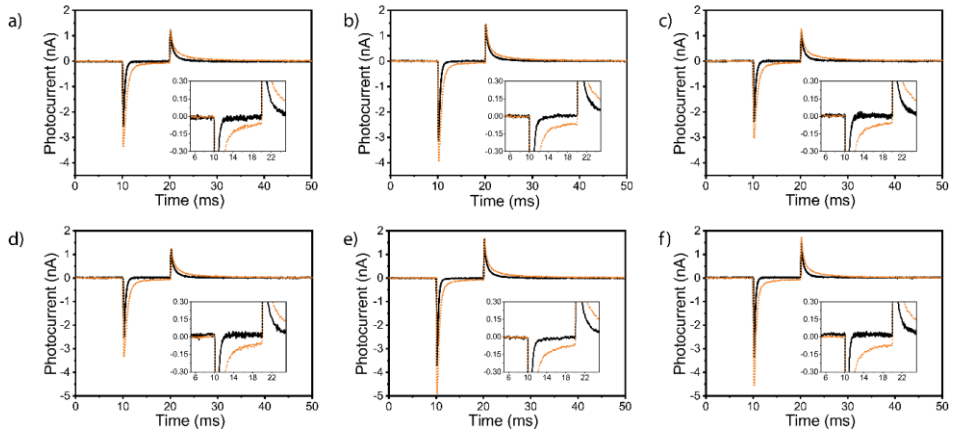

Figure 7.9: Photocurrents generated by the control and plasmonic biointerfaces under free standing mode. (a) – (c) Photocurrent vs time for control (black line) and plasmonic (orange dotted line) biointerfaces illuminated under same photon counts. The inset zooms low photocurrent levels. All axes are kept equal. (d) – (f) Photocurrent vs time for control (black line) and plasmonic (orange dotted line) biointerfaces excited under same optical power. The inset zooms low photocurrent levels. All axes are kept equal. ((a,d) – blue light illumination, (b,e) – green light illumination and (c,f) – red light illumination).

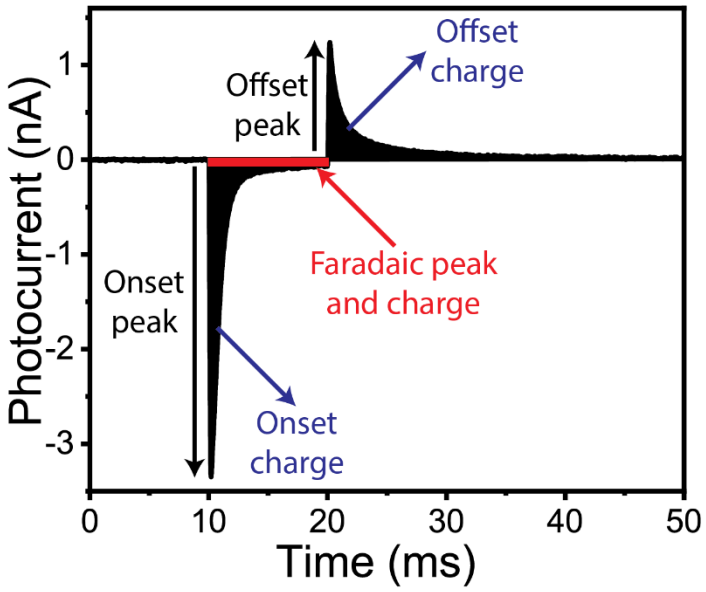

Figure 7.10: Peaks and charges of capacitive and faradaic photocurrent components.

$$Enhancement\ in\ onset\ peak = 100 \times \left(\frac{plasmonic\ onset\ peak - control\ onset\ peak}{control\ onset\ peak}\right) \quad (7.1)$$

$$Enhancement\ in\ onset\ charge = 100 \times \left(\frac{plasmonic\ onset\ charge - control\ onsetcharge}{control\ onset\ charge}\right) \quad (S6.2)$$

$$Faradaic\ peak\ percentage = 100 \times \left(\frac{Faradaic\ peak}{onset\ peak}\right) \quad (7.3)$$

$$Faradaic\ charge\ percentage = 100 \times \left(\frac{Faradaic\ charge}{onset\ charge}\right) \quad (7.4)$$

Table 7.1: Onset charge amount, Faradaic charge amount, Faradaic charge percentage, enhancement in charge for both control and plasmonic biointerfaces under blue, green and red light illumination having same photon counts (8.8±0.2 x 10^{16} photons $s^{-1}.cm^{-2}$).

	Blue		Green		Red	
	Control	Plasmonic	Control	Plasmonic	Control	Plasmonic
Onset charge (pC)	6.95	19.85	7.75	20.40	5.70	17.55
Faradaic charge (pC)	0.02	0.05	0	0.05	0	0.04
Faradaic charge (%)	0.1	0.25	0	0.24	0	0.24
Enhancement in onset charge (%)	185.6		163.2		207.9	

Table 7.2: Onset charge amount, Faradaic charge amount, Faradaic charge percentage, enhancement in charge for both control and plasmonic biointerfaces under blue, green and red light illumination having same optical power (42 ± 2 mW.cm^{-2}).

	Optical power					
	Blue		Green		Red	
	Control	Plasmonic	Control	Plasmonic	Control	Plasmonic
Onset charge (pC)	6.95	19.85	8.38	22.45	6.77	20.45
Faradaic charge (pC)	0.02	0.05	0	0.06	0	0.06
Faradaic charge (%)	0.1	0.25	0	0.26	0	0.29
Enhancement in onset charge (%)	185.6		167.9		202.0	

Table 7.3: Onset magnitude, Faradaic magnitude, Faradaic magnitude percentage, enhancement in magnitude for both control and plasmonic biointerfaces under blue, green and red light illumination having same photon counts (8.8±0.2 x 10^{16} photons s^{-1}.cm^{-2}).

	Counts					
	Blue		Green		Red	
	Control	Plasmonic	Control	Plasmonic	Control	Plasmonic
Onset peak (nA)	2.49	3.35	3.15	3.96	2.36	3.02
Faradaic peak (nA)	0.010	0.022	0	0.021	0	0.006
Faradaic peak (%)	0.40	0.65	0	0.53	0	0.35
Enhancement in onset peak (%)	34.5		25.7		28.0	

Table 7.4: Onset magnitude, Faradaic magnitude, Faradaic magnitude percentage, enhancement in magnitude for both control and plasmonic biointerfaces under blue, green and red light illumination having same optical power (42 ± 2 mW.cm^{-2}).

	Optical power					
	Blue		Green		Red	
	Control	Plasmonic	Control	Plasmonic	Control	Plasmonic
Onset peak (nA)	2.49	3.35	3.70	4.89	3.37	4.55
Faradaic peak (nA)	0.010	0.022	0	0.026	0	0.016
Faradaic peak (%)	0.40	0.65	0	0.06	0	0.35
Enhancement in onset peak (%)	34.5		32.2		35.0	

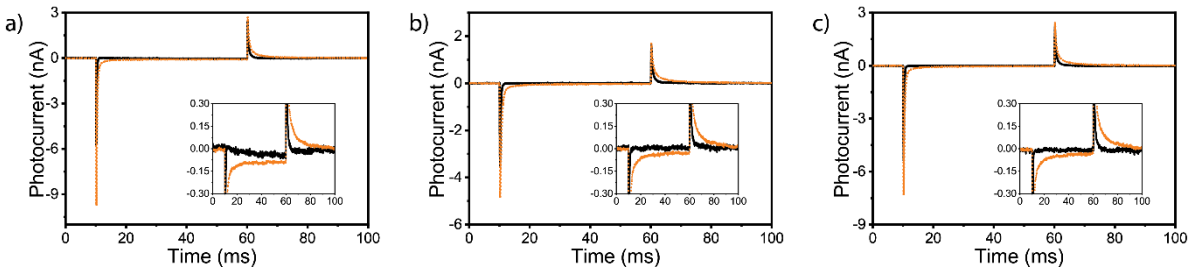

Figure 7.11: (a) – (c) Photocurrent vs time for control (black line) and plasmonic (orange line) biointerfaces illuminated under blue (a), green (b) and red (c) light with 50 ms pulse width and 100 ms period. The inset zooms low photocurrent level.

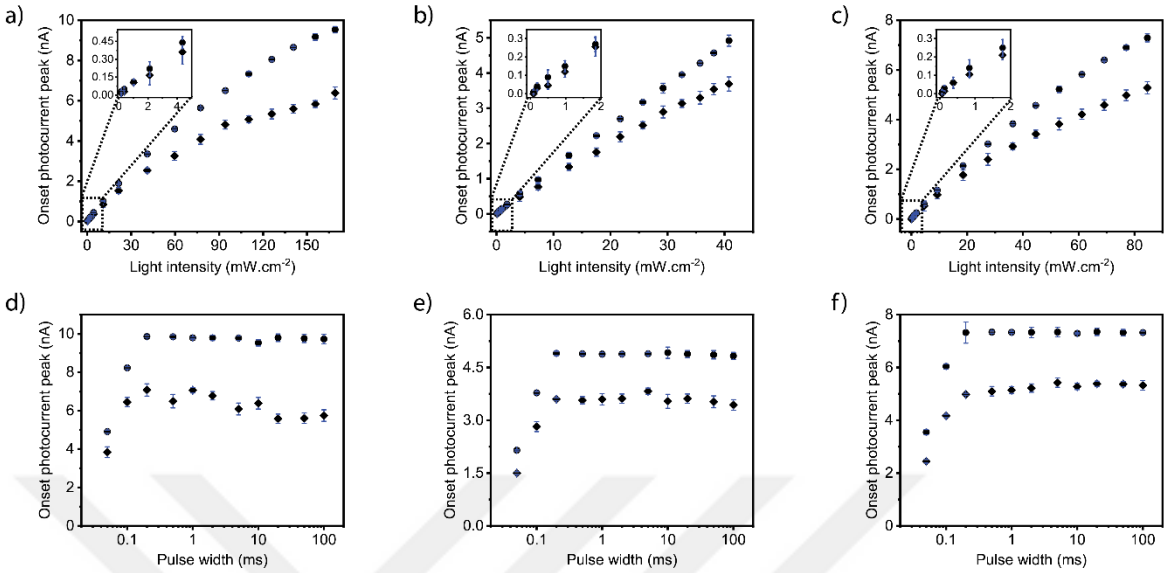

Figure 7.12: (a) - (c) Magnitude of onset peak of capacitive photocurrents of control (rhombus dots) and plasmonic (circle dots) biointerface as a function of light intensity. The inset zooms low light intensity levels. (d) - (f) Magnitude of onset peak of capacitive photocurrent of control (rhombus dots) and plasmonic (circle dots) biointerface as a function of pulse width under maximum light intensity. ((a,d) – blue light illumination, (b,e) – green light illumination and (c,f) – red light illumination.)

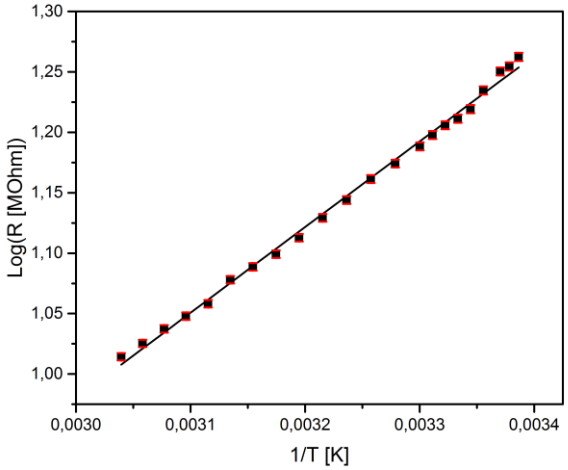

Figure 7.13: Temperature dependence of the pipette tip resistance. The pipette resistance did not change under continuous light illumination at 170 mW.cm^{-2}.

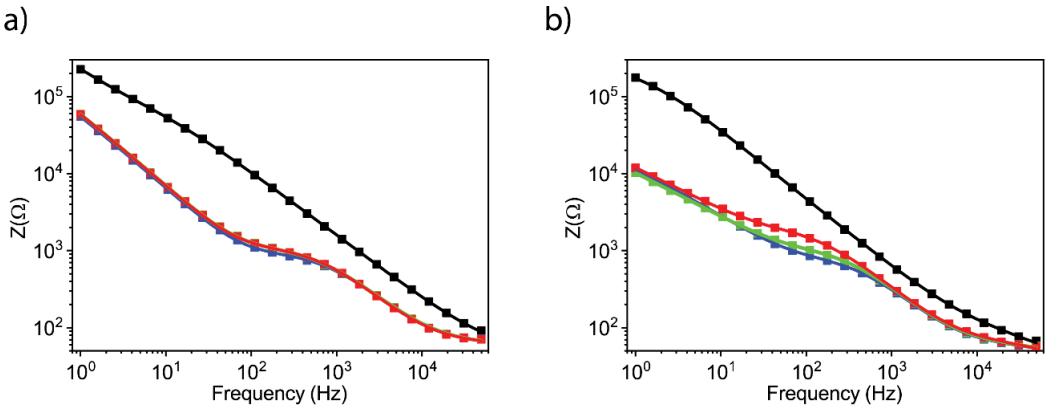

Figure 7.14: Electrochemical impedance spectroscopy of control and plasmonic biointerfaces under dark, blue, green and red light illumination at zero dc bias. (a) Bode magnitude of control biointerface. (b) Bode magnitude of plasmonic biointerface. (Squares - experimental data, lines – fitted data, black – no illumination, blue – blue light illumination, green – green light illumination and red – red light illumination)

Table 7.5: Fitted electrical parameters of the impedance analysis.

SAMPLE	Light	$R_s(\Omega)$	$R_{rec}(k\Omega)$	CPE1	W	$C_{dl}(\mu F)$	$R_l(\Omega)$	$C_g(nF)$	$\chi^2(\%)$
Plasmonic	Dark	45	26.300	3.50, 0.716	3.14	0.44	91.4	82.3	1.13
Plasmonic	Blue	45	0.663	1.14, 0.886	30.10	3.14	31.3	146.0	1.07
Plasmonic	Green	45	0.868	1.14, 0.882	35.80	3.06	33.7	137.0	1.10
Plasmonic	Red	45	1.610	1.32, 0.861	30.60	3.10	43.1	148.0	1.17
Control	Dark	45	72.600	0.84, 0.726	0.89	0.51	76.5	35.6	0.81
Control	Blue	45	0.777	0.50, 0.906	1.95	2.28	30.7	41.6	1.39
Control	Green	45	0.923	0.67, 0.880	1.82	2.13	24.7	31.3	3.10
Control	Red	45	0.919	0.57, 0.894	1.80	2.14	29.7	42.3	1.40

Table 7.6: Mobility and effective lifetime estimation using impedance analysis.

SAMPLE	Light	C_{μ}(μF)	τ_d(μs)	τ_n(μs)	D_n(nm)	μ_n(cm^2/Vs)(x10^{-5})
Plasmonic	D	1.36	61.14	35700.00	0.16	0.63
Plasmonic	B	0.45	20.16	297.02	0.50	1.92
Plasmonic	G	0.45	20.33	392.15	0.49	1.90
Plasmonic	R	0.49	21.99	786.93	0.46	1.76
Control	D	0.29	13.22	21300.00	0.80	3.10
Control	B	0.22	9.96	172.00	1.06	3.73
Control	G	0.24	10.99	225.40	0.96	3.91
Control	R	0.23	10.47	213.89	1.01	3.10

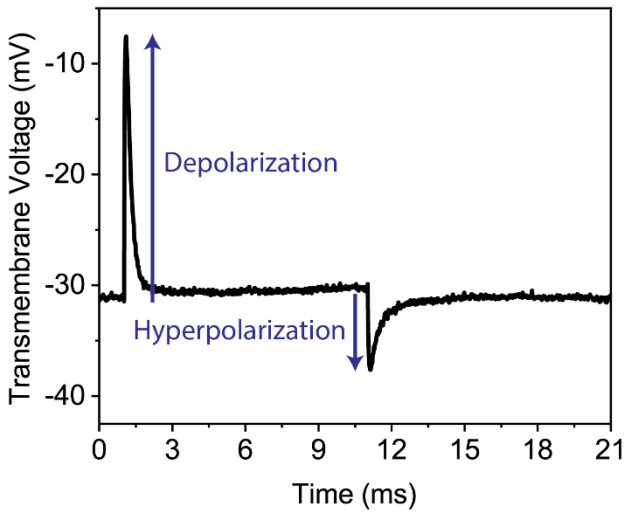

Figure 7.15: Transmembrane potential variation of SHSY-5Y cell on the plasmonic biointerface under blue LED excitation with 10 ms pulse width.

$$Enhancement\ in\ depolarization = 100 \times \left(\frac{plasmonic\ depolarization - control\ depolarization}{control\ depolarization}\right) \quad (7.5)$$

$$Overall\ enhancement\ in\ depolarization = \sum_{optical\ power/frequency}^{N} \frac{Enhancement\ in\ depolarization}{N} \quad (7.6)$$

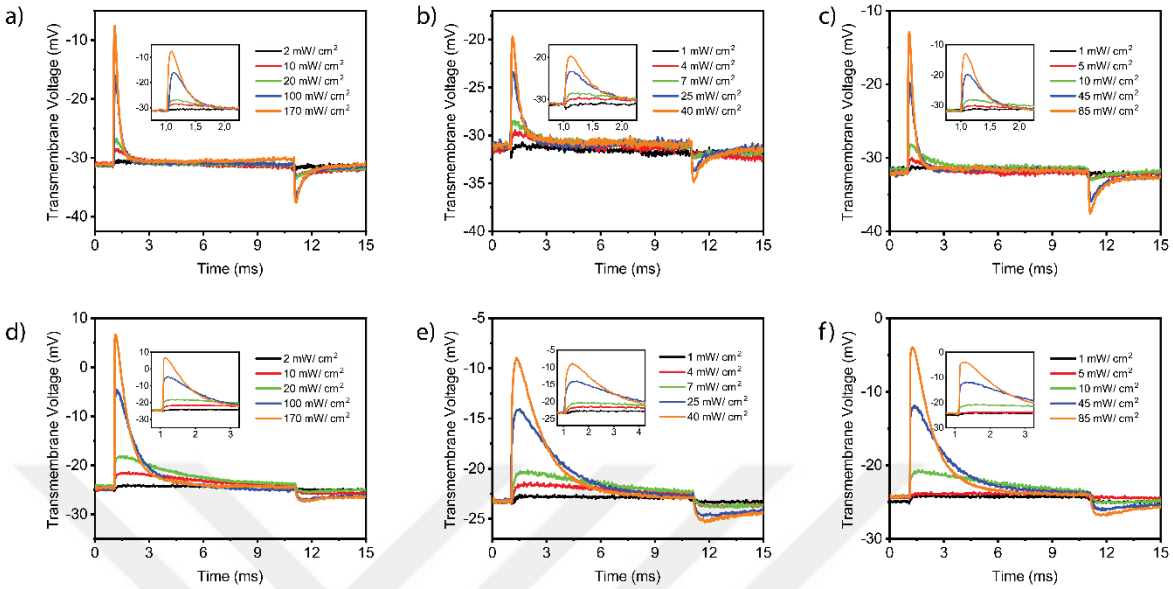

Figure 7.16: (a)-(c) Transmembrane potential variation of SHSY-5Y cell on control biointerface under light illumination with 10 ms pulse and 100 ms period. (d)-(e) Transmembrane potential variation of SHSY-5Y cell on plasmonic biointerface under light illumination with 10 ms pulse and 100 ms period. ((a,d) – blue light illumination with optical power of 2, 10, 20, 100 and 170 mW. cm^{-2} (b,e) – green light illumination with optical power of 1, 4, 7, 25 and 40 mW. cm^{-2} and (c,f) – red light illumination with optical power of 1, 5, 10, 45 and 85 mW/ cm^{-2} .

Table 7.7: Depolarization enhancement for both control and plasmonic biointerfaces for blue, green and red light illumination.

	Optical power (mW cm^{-2})	Depolarization (mV)		Enhancement in depolarization (%)	Overall enhancement in depolarization (%)
		Control	Plasmonic		
Blue	2	0.6	0.8	33.3	37.3
	10	2.5	3.6	44.0	
	20	4.2	6.0	42.9	
	100	15.0	19.9	32.6	
	170	23.4	31.3	33.8	
Green	1	0.4	0.6	50.0	25.3
	4	1.6	1.8	12.5	
	7	2.5	3.0	20.0	
	25	7.6	9.0	18.4	
	40	11.3	14.2	25.7	
Red	1	0.5	0.6	20.0	7.7
	5	1.9	2.0	5.3	
	10	3.3	3.5	6.1	
	45	12.2	12.32	1.0	
	85	19.1	20.3	6.3	

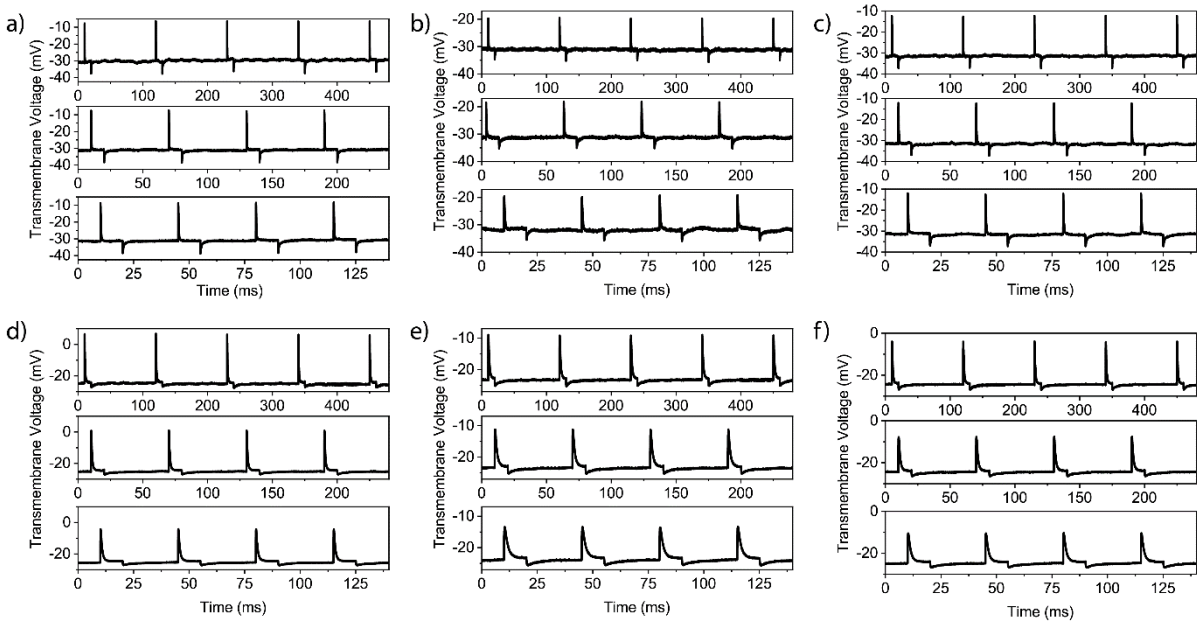

Figure 7.12: Effect of light evoked pulse trains on control and plasmonic biointerfaces under 10, 20 and 40 Hz illumination (pulse duration 10 ms). (a)-(c) Transmembrane potential variation of SHSY-5Y cell on control biointerface under light illumination with 10ms pulse with 100 ms (10 Hz, top) 50 ms (20 Hz, middle) and 25 ms (40 Hz, bottom) periods. (d)-(f) Transmembrane potential variation of SHSY-5Y cell on plasmonic biointerfaces under LED excitation with 10 ms pulse width with (10 Hz, top), (20 Hz, middle) and (40 Hz, bottom) periods. ((a,d) – blue LED excitation with optical power of 170 mW. cm^{-2} (b,e) – green LED excitation with optical power 40 mW cm^{-2} and (c,f) – red LED excitation with optical power of 85 mW cm^{-2}.)

Table 7.8: Depolarization enhancement for both control and plasmonic biointerfaces for blue, green and red light illumination with 10 ms pulse width and 100 ms, 50 ms and 25 ms periods.

Light	Frequency (Hz)	Depolarization (mV)		Enhancement in depolarization (%)	Overall enhancement in depolarization (%)
		Control	Plasmonic		
Blue	10	23.3	31.8	36.5	15.4
	20	23.4	26.7	14.1	
	40	22.7	21.7	-4.4	
Green	10	11.2	14.5	29.5	1.3
	20	12.9	12.3	-4.6	
	40	12.7	10.5	-20.9	
Red	10	19.0	20.6	10.0	-9.6
	20	19.4	17.0	-12.4	
	40	19.5	14.4	-26.4	

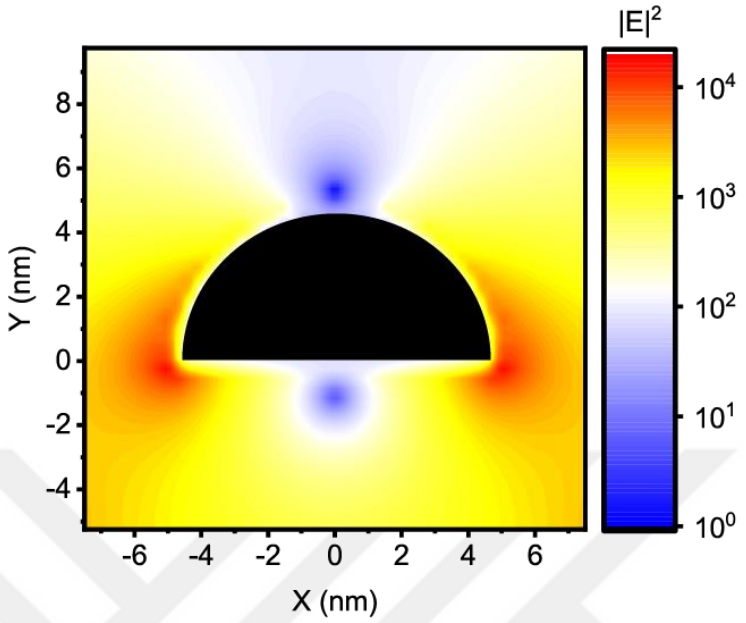

Figure 7.18: Electric field enhancement profile for AuNI using Lumerical FDTD software.

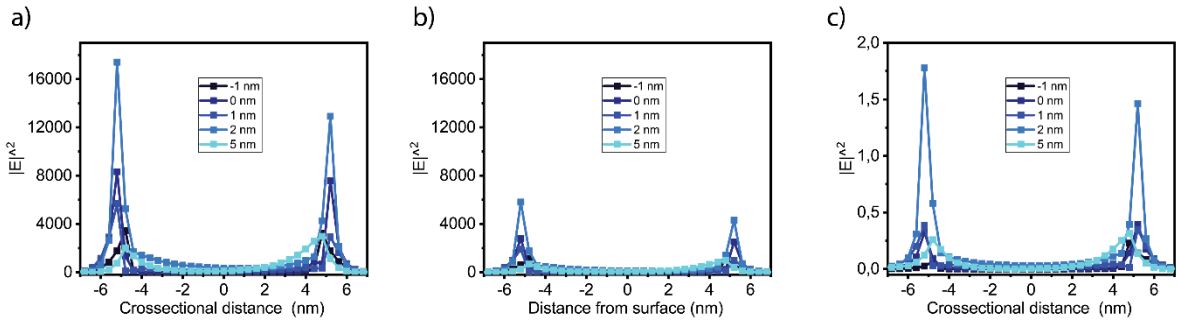

Figure 7.19: (a) Angle of k vector is 0^0. The wave illuminated perpendicular to biointerface surface. (b) Angle of k vector is 45^0. The wave illuminated diagonal to biointerface surface. (c) Angle of k vector is 90^0. The wave illuminated parallel to biointerface surface

Chapter 8: Conclusion

In project 1, without changing the surface material of the photoelectrode, we demonstrated that the band engineering of the photoelectrodes enables the control of the strength and type of photostimulation mechanisms. Via the proper selection of the intermediate layer, the strength of the Faradaic charge transfer can be adjusted and even it can be drastically suppressed and be converted to a capacitive mechanism. This approach is different from the conventional one that modifies the cell-electrode interaction by changing the material on the surface [20]. Moreover, the incorporation of quantum dots into the organic bulk-heterojunction blend significantly enhances the amount of photogenerated charge carriers that enabled to identify the Faradaic and capacitive charge-transfer mechanisms. In perspective, utilization of controlling photostimulation mechanism provides a new opportunity for neural prosthesis. Some important challenges in neural prosthesis, such as Faradaic degradation because of irreversible reactions at photoelectrode-neuron interface, long term biocompatibility, and finding-out a compatible material can be solved. Therefore, the results point to a new direction in engineering of neural interfaces for effective and safe photostimulation.

In project 2, we introduced a new photoactive bulk-heterojunction material system, PTB7-Th:PC71BM, for photostimulation of cells and we incorporated it into a capacitive charge-injecting biointerface design. By using this biointerface, we investigated the effect of the open-circuit voltage on the photoresponse of the bulk-heterojunction, and we observed that high-V_{oc} can simultaneously lead to strong and fast capacitive currents at the electrode-cell interfaces. In addition, light can also control the switching speed of capacitive currents that are caused by the variation of open-circuit voltage. Hence, the open-circuit voltage is an important design parameter for fast and effective switching of the neurons that can be controlled by light and electronic energy levels of the heterojunctions. Moreover, the wide absorption ranges from visible to near IR of the photoactive material system can be utilized for deep-tissue photostimulation such as brain

and heart. Therefore, bulk heterojunction composite based biointerfaces have high potential for safe, rapid, and controlled neural photostimulation of cells.

In project 3, we showed that modulation of rise and fall time slopes of light pulse waveforms control the direction and strength of currents generated by the photocapacitor. These capacitive currents facilitated high-level modulation of depolarization and hyperpolarization of the membrane potential. The control over hyperpolarization and depolarization by light can lead to an effective strategy for therapeutic purposes. Depending on the type of neural disorder, activation or silencing of neural activity is required. For example, Parkinson's disease requires depolarization of neural tissues to evoke action potential; on the other hand, in the case of epilepsy, suppression of neural activity is required. Moreover, since the maximum intensity levels illuminated at substrates are three orders of magnitude below maximum irradiance level for retinal cells, the control of capacitive currents via waveform shaping can be useful for retinal prosthetics as well. Our results pave the way toward non-genetic and safe light-activated implants for superior optical control of neural activity.

In project 4, we incorporated plasmonics to light-activated capacitive neurostimulators. Hot-electron injection and nanoantenna effect significantly enhanced the injected charge amounts and currents from the biointerface to the electrolyte. This facilitated variation of membrane potential at single-cell level within the low intensity levels of several $mW.cm^{-2}$, inside the safe limits for retinal photostimulation. In addition to the safe intensity levels, the capacitive charge-injection mechanism is a biocompatible neurostimulation strategy that can be applied long-term and repeatedly to the targeted neurological cell type. We believe that the marriage of plasmonics and optoelectronic biointerfaces point out a bright future for novel nanoengineered optoelectronic neural interfaces.

Bibliography

[1] L. Bareket-Keren and Y. Hanein, "Novel interfaces for light directed neuronal stimulation: advances and challenges," *Int J Nanomedicine,* vol. 9 Suppl 1, pp. 65-83, 2014.

[2] F. Di Maria, F. Lodola, E. Zucchetti, F. Benfenati, and G. Lanzani, "The evolution of artificial light actuators in living systems: from planar to nanostructured interfaces," *Chemical Society Reviews,* 2018.

[3] A. Steude, E. C. Witts, G. B. Miles, and M. C. Gather, "Arrays of microscopic organic LEDs for high-resolution optogenetics," *Sci Adv,* vol. 2, no. 5, p. e1600061, May 2016.

[4] V. Nikolenko, K. E. Poskanzer, and R. Yuste, "Two-photon photostimulation and imaging of neural circuits," *Nat Methods,* Article vol. 4, no. 11, pp. 943-50, Nov 2007.

[5] J. Rivnay, H. Wang, L. Fenno, K. Deisseroth, and G. G. Malliaras, "Next-generation probes, particles, and proteins for neural interfacing," *Sci Adv,* vol. 3, no. 6, p. e1601649, Jun 2017.

[6] S. Szobota and E. Y. Isacoff, "Optical control of neuronal activity," *Annu Rev Biophys,* vol. 39, pp. 329-48, 2010.

[7] E. Zrenner *et al.*, "Subretinal electronic chips allow blind patients to read letters and combine them to words," *Proceedings of the Royal Society B: Biological Sciences,* 10.1098/rspb.2010.1747 2010.

[8] X. Han and E. S. Boyden, "Multiple-color optical activation, silencing, and desynchronization of neural activity, with single-spike temporal resolution," *PLoS One,* vol. 2, no. 3, p. e299, Mar 21 2007.

[9] J. Delbeke, L. Hoffman, K. Mols, D. Braeken, and D. Prodanov, "And Then There Was Light: Perspectives of Optogenetics for Deep Brain Stimulation and Neuromodulation," *Frontiers in Neuroscience,* 10.3389/fnins.2017.00663 vol. 11, p. 663, 2017.

[10] J. S. Wiegert, M. Mahn, M. Prigge, Y. Printz, and O. Yizhar, "Silencing Neurons: Tools, Applications, and Experimental Constraints," *Neuron,* vol. 95, no. 3, pp. 504-529, Aug 2 2017.

[11] B. Tian *et al.*, "Roadmap on semiconductor-cell biointerfaces," *Phys Biol,* vol. 15, no. 3, p. 031002, Mar 9 2018.

[12] D. R. Merrill, M. Bikson, and J. G. Jefferys, "Electrical stimulation of excitable tissue: design of efficacious and safe protocols," *J Neurosci Methods,* vol. 141, no. 2, pp. 171-98, Feb 15 2005.

[13] B. S. Wilson, C. C. Finley, D. T. Lawson, R. D. Wolford, D. K. Eddington, and W. M. Rabinowitz, "Better speech recognition with cochlear implants," *Nature,* vol. 352, no. 6332, pp. 236-8, Jul 18 1991.

[14] A. L. Benabid, "Deep brain stimulation for Parkinson's disease," *Current opinion in neurobiology,* vol. 13, no. 6, pp. 696-706, 2003.

[15] T. R. Deer *et al.*, "The Appropriate Use of Neurostimulation of the Spinal Cord and Peripheral Nervous System for the Treatment of Chronic Pain and Ischemic Diseases: The N euromodulation A ppropriateness C onsensus C ommittee," *Neuromodulation: Technology at the Neural Interface,* vol. 17, no. 6, pp. 515-550, 2014.

[16] E. Zrenner *et al.*, "Subretinal electronic chips allow blind patients to read letters and combine them to words," *Proceedings of the Royal Society B: Biological Sciences,* vol. 278, no. 1711, pp. 1489-1497, 2011.

[17] D. E. Sanabria *et al.*, "Suppressing and amplifying neural oscillations in real-time using phase-locked electrical stimulation: concept, optimization and in-vivo testing," 2020.

[18] D. B. McCreery, T. G. Yuen, W. F. Agnew, and L. A. J. I. t. o. b. e. Bullara, "A characterization of the effects on neuronal excitability due to prolonged microstimulation with chronically implanted microelectrodes," vol. 44, no. 10, pp. 931-939, 1997.

[19] L. Ferlauto *et al.*, "Design and validation of a foldable and photovoltaic wide-field epiretinal prosthesis," *Nat Commun,* vol. 9, no. 1, p. 992, Mar 8 2018.

[20] S. F. Cogan, "Neural stimulation and recording electrodes," *Annu Rev Biomed Eng,* vol. 10, pp. 275-309, 2008.

[21] I. Schoen and P. Fromherz, "The mechanism of extracellular stimulation of nerve cells on an electrolyte-oxide-semiconductor capacitor," *Biophys J,* vol. 92, no. 3, pp. 1096-111, Feb 1 2007.

[22] G. G. Wallace, S. E. Moulton, and G. M. Clark, "Applied physics. Electrode-cellular interface," *Science,* 10.1126/science.1168346 vol. 324, no. 5924, pp. 185-6, Apr 10 2009.

[23] E. Pastrana, "Optogenetics: controlling cell function with light," *Nature Methods,* vol. 8, no. 1, pp. 24-25, 12/20/online 2010.

[24] D. Boinagrov *et al.*, "Photovoltaic Pixels for Neural Stimulation: Circuit Models and Performance," *IEEE Trans Biomed Circuits Syst,* vol. 10, no. 1, pp. 85-97, Feb 2016.

[25] E. Mosconi *et al.*, "Surface Polarization Drives Photoinduced Charge Separation at the P3HT/Water Interface," *ACS Energy Letters,* vol. 1, no. 2, pp. 454-463, 2016.

[26] F. Benfenati and G. Lanzani, "New technologies for developing second generation retinal prostheses," *Lab Anim (NY),* vol. 47, no. 3, pp. 71-75, Mar 2018.

[27] L. Bareket-Keren and Y. Hanein, "Carbon nanotube-based multi electrode arrays for neuronal interfacing: progress and prospects," *Front Neural Circuits,* vol. 6, p. 122, 2012.

[28] G. Simone *et al.*, "Near-Infrared Tandem Organic Photodiodes for Future Application in Artificial Retinal Implants," *Adv Mater,* vol. 30, no. 51, p. e1804678, Dec 2018.

[29] D. Ghezzi *et al.*, "A polymer optoelectronic interface restores light sensitivity in blind rat retinas," *Nat Photonics,* vol. 7, no. 5, pp. 400-406, May 2013.

[30] V. Gautam, D. Rand, Y. Hanein, and K. S. Narayan, "A polymer optoelectronic interface provides visual cues to a blind retina," *Adv Mater,* vol. 26, no. 11, pp. 1751-6, Mar 19 2014.

[31] D. Ghezzi, M. R. Antognazza, M. Dal Maschio, E. Lanzarini, F. Benfenati, and G. Lanzani, "A hybrid bioorganic interface for neuronal photoactivation," *Nat Commun,* Article vol. 2, p. 166, Jan 25 2011.

[32] V. Gautam, M. Bag, and K. S. Narayan, "Single-pixel, single-layer polymer device as a tricolor sensor with signals mimicking natural photoreceptors," *J Am Chem Soc,* vol. 133, no. 44, pp. 17942-9, Nov 9 2011.

[33] M. R. Antognazza, D. Ghezzi, D. Musitelli, M. Garbugli, and G. Lanzani, "A hybrid solid-liquid polymer photodiode for the bioenvironment," *Applied Physics Letters,* vol. 94, no. 24, p. 243501, 2009/06/15 2009.

[34] C. Sekirnjak, P. Hottowy, A. Sher, W. Dabrowski, A. M. Litke, and E. J. Chichilnisky, "Electrical stimulation of mammalian retinal ganglion cells with multielectrode arrays," *J Neurophysiol,* vol. 95, no. 6, pp. 3311-27, Jun 2006.

[35] M. G. Shapiro, K. Homma, S. Villarreal, C.-P. Richter, and F. Bezanilla, "Infrared light excites cells by changing their electrical capacitance," *Nature communications,* vol. 3, p. 736, 2012.

[36] N. Martino *et al.*, "Photothermal cellular stimulation in functional bio-polymer interfaces," *Sci Rep,* vol. 5, p. 8911, Mar 10 2015.

[37] K. Mathieson *et al.*, "Photovoltaic Retinal Prosthesis with High Pixel Density," *Nat Photonics,* vol. 6, no. 6, pp. 391-397, Jun 1 2012.

[38] G. Yu, J. Gao, J. C. Hummelen, F. Wudl, and A. J. Heeger, "Polymer Photovoltaic Cells: Enhanced Efficiencies via a Network of Internal Donor-Acceptor Heterojunctions," *Science,* vol. 270, no. 5243, pp. 1789-1791, 1995.

[39] D. Ghezzi *et al.*, "A polymer optoelectronic interface restores light sensitivity in blind rat retinas," *Nature Photonics,* Article vol. 7, p. 400, 03/17/online 2013.

[40] D. Ghezzi, M. R. Antognazza, M. Dal Maschio, E. Lanzarini, F. Benfenati, and G. Lanzani, "A hybrid bioorganic interface for neuronal photoactivation," *Nature Communications,* vol. 2, no. 1, p. 166, 2011/01/25 2011.

[41] B. Boveja, "Method and system for modulating the vagus nerve (10th cranial nerve) using modulated electrical pulses with an inductively coupled stimulation system," ed: Google Patents, 2003.

[42] A. M. Marzouk, A. Stanitzki, and R. Kokozinski, "Towards pulse-density modulated functional electrical stimulation of neural cells with passive membranes," in *PRIME 2012; 8th Conference on Ph. D. Research in Microelectronics & Electronics*, 2012, pp. 1-4: VDE.

[43] D. Rand *et al.*, "Direct Electrical Neurostimulation with Organic Pigment Photocapacitors," *Adv Mater,* vol. 30, no. 25, p. e1707292, Jun 2018.

[44] H. Bahmani Jalali *et al.*, "Effective neural photostimulation using indium-Based type-II quantum dots," vol. 12, no. 8, pp. 8104-8114, 2018.

[45] Y. Jiang *et al.*, "Rational design of silicon structures for optically controlled multiscale biointerfaces," *Nat Biomed Eng,* vol. 2, no. 7, pp. 508-521, Jul 2018.

[46] S. B. Srivastava, R. Melikov, M. M. Aria, U. M. Dikbas, I. H. Kavakali, and S. J. P. R. A. Nizamoglu, "Band Alignment Engineers Faradaic and Capacitive Photostimulation of Neurons Without Surface Modification," vol. 11, no. 4, p. 044012, 2019.

[47] T. Tatsuma, H. Nishi, and T. Ishida, "Plasmon-induced charge separation: chemistry and wide applications," *Chem Sci,* vol. 8, no. 5, pp. 3325-3337, May 1 2017.

[48] J. L. Carvalho-de-Souza, J. S. Treger, B. Dang, S. B. Kent, D. R. Pepperberg, and F. Bezanilla, "Photosensitivity of neurons enabled by cell-targeted gold nanoparticles," *Neuron,* vol. 86, no. 1, pp. 207-17, Apr 8 2015.

[49] K. Eom *et al.*, "Enhanced infrared neural stimulation using localized surface plasmon resonance of gold nanorods," *Small,* vol. 10, no. 19, pp. 3853-3857, 2014.

[50] S. Yoo, S. Hong, Y. Choi, J. H. Park, and Y. Nam, "Photothermal inhibition of neural activity with near-infrared-sensitive nanotransducers," *ACS Nano,* vol. 8, no. 8, pp. 8040-9, Aug 26 2014.

[51] J. W. Lee, H. Jung, H. H. Cho, J. H. Lee, and Y. Nam, "Gold nanostar-mediated neural activity control using plasmonic photothermal effects," *Biomaterials,* vol. 153, pp. 59-69, 2018.

[52] H. Nakatsuji *et al.*, "Thermosensitive Ion Channel Activation in Single Neuronal Cells by Using Surface-Engineered Plasmonic Nanoparticles," *Angewandte Chemie International Edition,* vol. 54, no. 40, pp. 11725-11729, 2015.

[53] P. Kollmannsberger, C. Bidan, J. Dunlop, and P. J. S. m. Fratzl, "The physics of tissue patterning and extracellular matrix organisation: how cells join forces," vol. 7, no. 20, pp. 9549-9560, 2011.

[54] U. A. Aregueta-Robles, A. J. Woolley, L. A. Poole-Warren, N. H. Lovell, and R. A. J. F. i. n. Green, "Organic electrode coatings for next-generation neural interfaces," vol. 7, p. 15, 2014.

[55] M. R. Antognazza, D. Ghezzi, D. Musitelli, M. Garbugli, and G. J. A. P. L. Lanzani, "A hybrid solid-liquid polymer photodiode for the bioenvironment," vol. 94, no. 24, p. 243501, 2009.

[56] E. Lanzarini *et al.*, "Polymer-based photocatalytic hydrogen generation," vol. 116, no. 20, pp. 10944-10949, 2012.

[57] D. Ghezzi, M. R. Antognazza, M. Dal Maschio, E. Lanzarini, F. Benfenati, and G. Lanzani, "A hybrid bioorganic interface for neuronal photoactivation," *Nat Commun,* vol. 2, no. 1, p. 166, Jan 25 2011.

[58] S. B. Srivastava, R. Melikov, M. M. Aria, U. M. Dikbas, I. H. Kavakli, and S. Nizamoglu, "Band Alignment Engineers Faradaic and Capacitive Photostimulation of Neurons Without Surface Modification," *Physical Review Applied,* vol. 11, no. 4, p. 044012, 04/04/ 2019.

[59] H. Yuk, B. Lu, and X. J. C. S. R. Zhao, "Hydrogel bioelectronics," vol. 48, no. 6, pp. 1642-1667, 2019.

[60] J. L. Carvalho-de-Souza, J. S. Treger, B. Dang, S. B. Kent, D. R. Pepperberg, and F. Bezanilla, "Photosensitivity of neurons enabled by cell-targeted gold nanoparticles," *Neuron,* vol. 86, no. 1, pp. 207-217, 2015.

[61] S. Yoo, S. Hong, Y. Choi, J.-H. Park, and Y. Nam, "Photothermal inhibition of neural activity with near-infrared-sensitive nanotransducers," *ACS nano,* vol. 8, no. 8, pp. 8040-8049, 2014.

[62] L. R. Hirsch *et al.*, "Nanoshell-mediated near-infrared thermal therapy of tumors under magnetic resonance guidance," *Proceedings of the National Academy of Sciences,* vol. 100, no. 23, pp. 13549-13554, 2003.

[63] X. Huang, I. H. El-Sayed, W. Qian, and M. A. El-Sayed, "Cancer cell imaging and photothermal therapy in the near-infrared region by using gold nanorods," *Journal of the American Chemical Society,* vol. 128, no. 6, pp. 2115-2120, 2006.

[64] J. L. Carvalho-de-Souza, B. I. Pinto, D. R. Pepperberg, and F. Bezanilla, "Optocapacitive generation of action potentials by microsecond laser pulses of nanojoule energy," *Biophysical journal,* vol. 114, no. 2, pp. 283-288, 2018.

[65] P. Bazard, R. D. Frisina, J. P. Walton, and V. R. J. S. r. Bhethanabotla, "Nanoparticle-based plasmonic transduction for modulation of electrically excitable cells," vol. 7, no. 1, pp. 1-13, 2017.

[66] H. Kang, G.-H. Lee, H. Jung, J. W. Lee, and Y. J. A. n. Nam, "Inkjet-printed biofunctional thermo-plasmonic interfaces for patterned neuromodulation," vol. 12, no. 2, pp. 1128-1138, 2018.

[67] A. G. Pattantyus-Abraham *et al.*, "Depleted-heterojunction colloidal quantum dot solar cells," *ACS Nano,* vol. 4, no. 6, pp. 3374-80, Jun 22 2010.

[68] S. A. McDonald *et al.*, "Solution-processed PbS quantum dot infrared photodetectors and photovoltaics," *Nat Mater,* vol. 4, no. 2, pp. 138-42, Feb 2005.

[69] R. J. Ellingson *et al.*, "Highly efficient multiple exciton generation in colloidal PbSe and PbS quantum dots," *Nano Lett,* vol. 5, no. 5, pp. 865-71, May 2005.

[70] F. Xi *et al.*, "Deposition temperature effect of RF magnetron sputtered molybdenum oxide films on the power conversion efficiency of bulk-heterojunction solar cells," *Journal of Physics D: Applied Physics,* vol. 44, no. 4, p. 045101, 2011.

[71] W. J. Beenken *et al.*, "Sub-bandgap absorption in organic solar cells: experiment and theory," *Phys Chem Chem Phys,* 10.1039/C3CP42236D vol. 15, no. 39, pp. 16494-502, Oct 21 2013.

[72] Y. Yan *et al.*, "Light-Soaking-Free Inverted Polymer Solar Cells with an Efficiency of 10.5% by Compositional and Surface Modifications to a Low-Temperature-Processed TiO2 Electron-Transport Layer," *Adv Mater,* vol. 29, no. 1, p. 1604044, Jan 2017.

[73] S. B. Srivastava, P. Sonar, and S. P. Singh, "Charge transport studies in donor-acceptor block copolymer PDPP-TNT and PC71BM based inverted organic photovoltaic devices processed in room conditions," *AIP Advances,* vol. 5, no. 7, p. 077177, 2015/07/01 2015.

[74] S. B. Srivastava, R. Melikov, M. M. Aria, U. M. Dikbas, I. H. Kavakali, and S. Nizamoglu, "Band Alignment Engineers Faradaic and Capacitive Photostimulation of Neurons Without Surface Modification," *Physical Review Applied,* vol. 11, no. 4, p. 044012, 2019.

[75] S. F. Cogan, "Neural Stimulation and Recording Electrodes," *Annual Review of Biomedical Engineering,* vol. 10, no. 1, pp. 275-309, 2008/08/01 2008.

[76] S. B. Srivastava, S. K. Srivastava, and S. P. Singh, "Molecular-Shape-Induced Efficiency Enhancement in PC61BM and PC71BM Based Ternary Blend Organic Solar Cells," *The Journal of Physical Chemistry C,* vol. 121, no. 32, pp. 17104-17111, 2017/08/17 2017.

[77] G. Garcia-Belmonte, A. Munar, E. M. Barea, J. Bisquert, I. Ugarte, and R. Pacios, "Charge carrier mobility and lifetime of organic bulk heterojunctions analyzed by impedance spectroscopy," *Organic Electronics,* vol. 9, no. 5, pp. 847-851, 2008/10/01/ 2008.

[78] C. H. Chuang, P. R. Brown, V. Bulovic, and M. G. Bawendi, "Improved performance and stability in quantum dot solar cells through band alignment engineering," *Nat Mater,* vol. 13, no. 8, pp. 796-801, Aug 2014.

[79] T. Ameri, P. Khoram, J. Min, and C. J. Brabec, "Organic ternary solar cells: a review," *Adv Mater,* vol. 25, no. 31, pp. 4245-66, Aug 21 2013.

[80] D. Shao *et al.*, "TiO 2–P3HT: PCBM photoelectrochemical tandem cells for solar-driven overall water splitting," *Journal of Materials Chemistry A,* vol. 6, no. 9, pp. 4032-4039, 2018.

[81] S. B. Srivastava, M. H. Modi, S. K. Ghosh, and S. P. Singh, "Investigation of the buried planar interfaces in multi-layered inverted organic solar cells using x-ray reflectivity and impedance spectroscopy," *J Phys Condens Matter,* vol. 31, no. 12, p. 124003, Mar 27 2019.

[82] S. B. Srivastava, P. Sonar, and S. P. Singh, "Analysis of degradation mechanisms in donor–acceptor copolymer based organic photovoltaic devices using impedance spectroscopy," *Materials Research Express,* vol. 3, no. 9, p. 096202, 2016.

[83] F. Wallrapp and P. Fromherz, "Ti O 2 and Hf O 2 in electrolyte-oxide-silicon configuration for applications in bioelectronics," *Journal of Applied Physics,* vol. 99, no. 11, p. 114103, 2006.

[84] M. Plaksin, E. Shapira, E. Kimmel, and S. Shoham, "Thermal Transients Excite Neurons through Universal Intramembrane Mechanoelectrical Effects," *Physical Review X,* vol. 8, no. 1, p. 011043, 2018.

[85] A. Varghese, E. M. Tenbroek, J. Coles, Jr., and D. C. Sigg, "Endogenous channels in HEK cells and potential roles in HCN ionic current measurements," *Prog Biophys Mol Biol,* vol. 90, no. 1-3, pp. 26-37, Jan-Apr 2006.

[86] R. Parameswaran *et al.*, "Photoelectrochemical modulation of neuronal activity with free-standing coaxial silicon nanowires," *Nat Nanotechnol,* vol. 13, no. 3, pp. 260-266, Mar 2018.

[87] M. C. Scharber *et al.*, "Design Rules for Donors in Bulk-Heterojunction Solar Cells—Towards 10 % Energy-Conversion Efficiency," *Advanced Materials,* vol. 18, no. 6, pp. 789-794, 2006/03/17 2006.

[88] J. L. Bredas, D. Beljonne, V. Coropceanu, and J. Cornil, "Charge-transfer and energy-transfer processes in pi-conjugated oligomers and polymers: a molecular picture," *Chem Rev,* vol. 104, no. 11, pp. 4971-5004, Nov 2004.

[89] N. S. Sariciftci, L. Smilowitz, A. J. Heeger, and F. Wudl, "Photoinduced electron transfer from a conducting polymer to buckminsterfullerene," *Science,* vol. 258, no. 5087, pp. 1474-6, Nov 27 1992.

[90] S. H. Liao, H. J. Jhuo, Y. S. Cheng, and S. A. Chen, "Fullerene derivative-doped zinc oxide nanofilm as the cathode of inverted polymer solar cells with low-bandgap polymer (PTB7-Th) for high performance," *Adv Mater,* vol. 25, no. 34, pp. 4766-71, Sep 14 2013.

[91] D. Chi, S. Qu, Z. Wang, and J. Wang, "High efficiency P3HT:PCBM solar cells with an inserted PCBM layer," *Journal of Materials Chemistry C,* 10.1039/C4TC00003J vol. 2, no. 22, pp. 4383-4387, 2014.

[92] K. Yuan, L. Chen, and Y. Chen, "Photovoltaic performance enhancement of P3HT/PCBM solar cells driven by incorporation of conjugated liquid crystalline rod-coil block copolymers," *J. Mater. Chem. C,* 10.1039/C4TC00066H vol. 2, no. 19, pp. 3835-3845, 2014.

[93] A. Rizzo *et al.*, "Characterization and modeling of organic (P3HT:PCBM) solar cells as a function of bias and illumination," *Solar Energy Materials and Solar Cells,* vol. 157, pp. 337-345, 2016/12/01/ 2016.

[94] P. R. Berger and M. Kim, "Polymer solar cells: P3HT:PCBM and beyond," *Journal of Renewable and Sustainable Energy,* vol. 10, no. 1, p. 013508, 2018/01/01 2018.

[95] N. K. Elumalai and A. Uddin, "Open circuit voltage of organic solar cells: an in-depth review," *Energy & Environmental Science,* 10.1039/C5EE02871J vol. 9, no. 2, pp. 391-410, 2016.

[96] A. K. Kyaw *et al.*, "Intensity dependence of current-voltage characteristics and recombination in high-efficiency solution-processed small-molecule solar cells," *ACS Nano,* vol. 7, no. 5, pp. 4569-77, May 28 2013.

[97] Z. Li, F. Gao, N. C. Greenham, and C. R. McNeill, "Comparison of the Operation of Polymer/Fullerene, Polymer/Polymer, and Polymer/Nanocrystal Solar Cells: A Transient Photocurrent and Photovoltage Study," *Advanced Functional Materials,* vol. 21, no. 8, pp. 1419-1431, 2011/04/22 2011.

[98] M. M. Aria *et al.*, "Perovskite-Based Optoelectronic Biointerfaces for Non-Bias-Assisted Photostimulation of Cells," *Advanced Materials Interfaces,* vol. 6, no. 17, p. 1900758, 2019/09/01 2019.

[99] I. Schoen and P. Fromherz, "Extracellular stimulation of mammalian neurons through repetitive activation of Na+ channels by weak capacitive currents on a silicon chip," *J Neurophysiol,* vol. 100, no. 1, pp. 346-57, Jul 2008.

[100] C. Veraart *et al.*, "Visual sensations produced by optic nerve stimulation using an implanted self-sizing spiral cuff electrode," *Brain Research,* vol. 813, no. 1, pp. 181-186, 1998/11/30/ 1998.

[101] F. T. Hambrecht, "Visual prostheses based on direct interfaces with the visual system," *Baillieres Clin Neurol,* vol. 4, no. 1, pp. 147-65, Apr 1995.

[102] R. Melikov *et al.*, "Bidirectional optical neuromodulation using capacitive charge-transfer," vol. 11, no. 11, pp. 6068-6077, 2020.

[103] O. S. Abdullaeva *et al.*, "Photoelectrical stimulation of neuronal cells by an organic semiconductor–electrolyte interface," *Langmuir,* vol. 32, no. 33, pp. 8533-8542, 2016.

[104] N. K. Elumalai, A. J. E. Uddin, and E. Science, "Open circuit voltage of organic solar cells: an in-depth review," vol. 9, no. 2, pp. 391-410, 2016.

[105] R. Melikov *et al.*, "Plasmon-Coupled Photocapacitor Neuromodulators," *ACS Applied Materials & Interfaces,* vol. 12, no. 32, pp. 35940-35949, 2020/08/12 2020.

[106] I. M. Soganci, S. Nizamoglu, E. Mutlugun, O. Akin, and H. V. Demir, "Localized plasmon-engineered spontaneous emission of CdSe/ZnS nanocrystals closely-packed in the proximity of Ag nanoisland films for controlling emission linewidth, peak, and intensity," *Opt Express,* vol. 15, no. 22, pp. 14289-98, Oct 29 2007.

[107] C. V. Hoang *et al.*, "Interplay of hot electrons from localized and propagating plasmons," *Nat Commun,* vol. 8, no. 1, p. 771, Oct 3 2017.

[108] L. Zhao, S. Zhao, Z. Xu, B. Qiao, D. Huang, and X. Xu, "Two effects of 1, 8-diiodooctane on PTB7-Th: PC71BM polymer solar cells," *Organic Electronics,* vol. 34, pp. 188-192, 2016.

[109] G. Bhattacharya *et al.*, "Probing the flat band potential and effective electronic carrier density in vertically aligned nitrogen doped diamond nanorods via electrochemical method," *Electrochimica Acta,* vol. 246, pp. 68-74, 2017.

[110] A. Maurano *et al.*, "Recombination dynamics as a key determinant of open circuit voltage in organic bulk heterojunction solar cells: a comparison of four different donor polymers," *Advanced Materials,* vol. 22, no. 44, pp. 4987-4992, 2010.

[111] O. S. Abdullaeva *et al.*, "Organic Photovoltaic Sensors for Photocapacitive Stimulation of Voltage-Gated Ion Channels in Neuroblastoma Cells," *Advanced Functional Materials,* vol. 29, no. 21, p. 1805177, 2019.

[112] M. Jakešová *et al.*, "Optoelectronic control of single cells using organic photocapacitors," *Science advances,* vol. 5, no. 4, p. eaav5265, 2019.

[113] M. C. Gather and S. H. Yun, "Single-cell biological lasers," *Nature Photonics,* vol. 5, no. 7, p. 406, 2011.

[114] L. Bareket-Keren and Y. Hanein, "Novel interfaces for light directed neuronal stimulation: advances and challenges," *International journal of nanomedicine,* vol. 9, no. Suppl 1, p. 65, 2014.

[115] H. Bahmani Jalali *et al.*, "Effective neural photostimulation using indium-Based type-II quantum dots," *ACS nano,* vol. 12, no. 8, pp. 8104-8114, 2018.

[116] R. Parameswaran *et al.*, "Photoelectrochemical modulation of neuronal activity with free-standing coaxial silicon nanowires," *Nature nanotechnology,* vol. 13, no. 3, p. 260, 2018.

[117] N. M. Bressler, S. B. Bressler, and S. L. Fine, "Age-related macular degeneration," *Survey of ophthalmology,* vol. 32, no. 6, pp. 375-413, 1988.

[118] D. T. Hartong, E. L. Berson, and T. P. Dryja, "Retinitis pigmentosa," *Lancet,* vol. 368, no. 9549, pp. 1795-809, Nov 18 2006.

[119] F. C. Delori, G. Staurenghi, O. Arend, C. K. Dorey, D. G. Goger, and J. J. Weiter, "In vivo measurement of lipofuscin in Stargardt's disease--Fundus flavimaculatus," *Invest Ophthalmol Vis Sci,* vol. 36, no. 11, pp. 2327-31, Oct 1995.

[120] T. K. Sau and A. L. Rogach, *Complex-shaped metal nanoparticles*. Wiley Online Library, 2012.